The Pennsylvania State University
APPLIED RESEARCH LABORATORY
P.O. Box 30
State College, PA 16804

SOUND RADIATION FROM AN ENCLOSURE

By

J. B. Fahnline
R. L. Campbell
S. A. Hambric

Technical Report 02-018

REPORT DOCUMENTATION PAGE

Form Approved OMB No. 0704-0188

1. REPORT DATE *(DD-MM-YYYY)*	2. REPORT TYPE	3. DATES COVERED *(From - To)*
5/9/2002	Technical Report	May 2000-May 2003

4. TITLE AND SUBTITLE
Sound Radiation from an Enclosure

5a. CONTRACT NUMBER
PL01000100

5b. GRANT NUMBER

5c. PROGRAM ELEMENT NUMBER

6. AUTHOR(S)
J. B. Fahnline, R. L. Campbell, and S. A. Hambric

5d. PROJECT NUMBER

5e. TASK NUMBER

5f. WORK UNIT NUMBER

7. PERFORMING ORGANIZATION NAME(S) AND ADDRESS(ES)

Applied Research Laboratory
Post Office Box 30
State College, PA 16804

8. PERFORMING ORGANIZATION REPORT NUMBER

TR 02-018

9. SPONSORING / MONITORING AGENCY NAME(S) AND ADDRESS(ES)

10. SPONSOR/MONITOR'S ACRONYM(S)

11. SPONSOR/MONITOR'S REPORT NUMBER(S)

12. DISTRIBUTION / AVAILABILITY STATEMENT

Approved for public release, distribution unlimited

13. SUPPLEMENTARY NOTES

14. ABSTRACT
The goal of the analysis is to demonstrate that the noise radiated from an existing enclosure can be predicted using finite elements or experimental measurements for the structural vibrations and boundary elements for the acoustic analysis. Because the acoustic analysis proceeds straightforwardly once the structural vibrations have been determined, the finite element analysis is the main obstacle to making the predictions. Standard "modal assurance criteria" (MAC) analyses are used to directly compare experimental measurements and finite element results and assess the accuracy of the finite element models. Methods for modeling rib-stiffened components are discussed extensively because of their importance in transmitting forces from the enclosure's shelves to its outer skin. The general conclusion is that this type of analysis is very useful for better understanding basic radiation mechanisms, but presently is not accurate enough for precisely predicting radiated noise levels.

15. SUBJECT TERMS

16. SECURITY CLASSIFICATION OF:			17. LIMITATION OF ABSTRACT	18. NUMBER OF PAGES	19a. NAME OF RESPONSIBLE PERSON
a. REPORT	b. ABSTRACT	c. THIS PAGE			19b. TELEPHONE NUMBER *(include area code)*
UNCLASSIFIED	UNCLASSIFIED	UNCLASSIFIED	UU UNCLASSIFIED-UNLIMITED	77	

TABLE OF CONTENTS

LIST OF TABLES

LIST OF FIGURES

LIST OF FIGURES, Cont.

LIST OF FIGURES, Cont.

LIST OF FIGURES, Cont.

INTRODUCTION

In the area of noise control, an enclosure is a structure surrounding a sound source which reduces its radiated noise. Traditionally, enclosures are primarily intended for controlling airborne sound transmission paths. In our application, the enclosure houses the sound source and is intended to reduce both its structural and airborne transmission paths. In this report, we will be primarily concerned with predicting radiated noise from an existing enclosure using finite and boundary element methods.

In our analysis, the sound radiation from an enclosure is computed in two steps. First, the finite element method is used to predict its structural vibrations. For the existing enclosure, this step is very difficult and time consuming because of its complexity. In particular, the way the various parts are interconnected is very difficult to model, especially since the enclosure was only available for testing after it was already fully assembled. After determining the structural vibrations of the enclosure's outer surface, its radiated noise can be predicted in a relatively straightforward manner using boundary element methods.

Since the finite element analysis is the main obstacle to making the predictions, one of the main goals of the analysis will be to assess its accuracy. We will discuss methods for modeling rib-stiffened components extensively because of their importance in transmitting forces from the enclosure shelves to the outer skin. To help validate the results, we have implemented our own version of the standard "modal assurance criteria" (MAC) analysis, which allows experimental measurements and finite element results to be directly compared.

MODELING OF RIB-STIFFENED ENCLOSURE COMPONENTS

In connecting angles to plates in a finite element model, we can conceivably use offset beam elements, plate elements, or three-dimensional solid elements to represent stiffeners and angles. The level of model complexity and fidelity both increase as we proceed from beam elements to plate elements to solid elements. In the initial enclosure model supplied to ARL, offset beam elements were used to model angles and stiffeners. This approach is by far the simplest, both in terms of the time required to generate a finite element model and the time required to run it. However, our results will demonstrate that offset beam elements have difficulties in representing the interaction between angles and plates meeting at right angles. Solid elements are capable of correctly modeling almost any type of structural behavior, but they are difficult to apply to thin plate-like structures because several elements are required through the thickness to correctly capture bending vibrations. Combining this requirement with the recommended maximum element aspect ratio of approximately three, the number of elements required quickly becomes prohibitive for anything but the simplest problems. Thus, in the context of modeling angles and plates, solid elements are primarily useful as a means of generating high fidelity solutions to simple example problems.

The remaining alternative is to model both angles and plates using plate elements (CQUAD and CTRIA in NASTRAN). This approach is intuitively attractive because both types of structural components physically resemble thin plates, such that the finite element model closely resembles the actual physical structure. The main disadvantage of this approach is the extra effort required to generate the geometric model of the structure. For example, Figure 1 shows a comparison between an offset-beam representation of one shelf of the enclosure and a plate element representation. In generating the offset-beam geometric model, approximately 17 surfaces are created and meshed. This contrasts with the plate element model

requiring approximately 70 surfaces. Also, the mesh generation phase of the analysis is much more difficult for the plate element model because the elements on all the intersecting surfaces have to join together properly, generally requiring mapped meshing techniques to be used.

To demonstrate that plate elements can correctly model the behavior in regions where angles are joined to plates, a simple example problem was devised. As illustrated in Figure 2, the model consists of two angles joined together at a right angle, with a plate connected to one of the angles. The figure also includes a simple line drawing showing the physical dimensions for the angle and plate. The three-dimensional hexahedral element mesh shown in the figure is made up of 8-noded linear CHEXA (hexahedral or "brick) elements, yielding 73740 nodes and 55488 elements. Similarly, Figure 3 shows a three-dimensional mesh consisting of 20-noded quadratic CHEXA elements, yielding 48349 nodes and 8600 elements. Both models should be able to correctly represent the vibrations, and indeed, the resonance frequencies listed in Table 1 for the two hexahedral meshes compare very well to each other. We will now use these results to check the accuracy of the simpler offset beam and plate element models.

For the plate model, we have to be careful to properly represent the stiffness and mass properties of the various components, especially since for this example problem both the plate and angles are relatively thick. Figure 4 shows the plate model along with illustrations of the element connections. At the junction between the plate and the angle, the plate elements are offset from the centerline of the plate to the centerline of the plate-angle combination. The offset plate elements are then rigidly connected to the horizontal surface of the angle using rigid bar RBE2 elements in NASTRAN. If we had instead tried to simply join the plate elements together along an edge, some of the material would be duplicated, leading to errors in the mass and stiffness properties. The resulting finite element model has 7996 nodes and 7743 elements. Table 1 lists the resulting resonance frequencies for the plate model. The correspondence between the resonance frequencies for the fully three-dimensional models and the plate model is fairly good, with the plate element models being slightly stiffer. As discussed in the NASTRAN "Common Questions and Answers" manual [1], pp. 69-72, the stiffness is expected to be too high because the membrane behavior is only represented approximately. A coarser mesh density, as illustrated in Figure 5, was also tested as a means of showing that the accuracy is adequate for more realistic mesh densities.

Finally, we could also represent angles connected to plates using offset beam elements. In the model supplied to ARL, the vertical legs of the stiffening beams were represented using beams offset in the vertical direction only, with the beam elements connected to the nodes at the line of intersection. The basic difficulty with this approach is that the offset beam adds stiffness to both the plate and the horizontal surface of the angle simultaneously. To account for the mass and stiffness properly, we thus have to offset the beam in two directions. Figure 6 shows one possible method for accounting for both offsets using three sets of rigid RBE2 elements. The first set of RBE2 elements connects the edge of the horizontal surface of the angle to the plate. The second and third sets connect the center of mass of the beam to the plate and the horizontal surface of the angle, respectively. The resulting finite element model has 8162 nodes and 8191 elements. Table 1 lists the resulting resonance frequencies for the offset beam model. In this case, the correspondence between the fully three-dimensional model and the beam model is also fairly good, but now the model is slightly too soft. Physically, this makes sense because in our model the beam is only connected to the angle and plate along one line, whereas in actuality the beams connect over areas.

Overall, the results from the simple example problem show that offset beam elements, plate elements, or three-dimensional solid elements can be used to represent stiffeners and angles. Of the three choices, either offset beams or plate elements are more useful for practical engineering problems. Between these two choices, mesh creation is somewhat easier for offset beams but plate elements should yield better accuracy, especially for the long, thin stiffeners in the enclosure under consideration. The other

unresolved issue is the degree to which the angles and the plates are welded together. In our model, it is assumed the angles are welded uniformly to the plate, whereas in the actual enclosure the drawings call for spot welding over only a relatively small area.

VALIDATION USING A MAC ANALYSIS

The standard way of comparing finite element results to experimental data is by computing the "modal assurance criteria" (MAC). In simple terms, a MAC analysis is used to determine how much two vibration distributions resemble each other. The calculations are very similar to those used to evaluate the coherence between two signals, only now we are comparing two spatial vibration distributions rather than two time signals. The basic formula for the modal assurance criteria with respect to mode μ is given as

$$MAC(\mu, f) = \frac{\left| \sum_{\nu=1}^{NN} \boldsymbol{\phi}_{\mu}(\mathbf{x}_{\nu}) \cdot \mathbf{n} \;\; \mathbf{d}(\mathbf{x}_{\nu}, f) \cdot \mathbf{n} \right|^2}{\sum_{\nu=1}^{NN} \left| \boldsymbol{\phi}_{\mu}(\mathbf{x}_{\nu}) \cdot \mathbf{n} \right|^2 \sum_{\nu=1}^{NN} \left| \mathbf{d}(\mathbf{x}_{\nu}, f) \cdot \mathbf{n} \right|^2}$$

where $\boldsymbol{\phi}_{\mu}(\mathbf{x}_{\nu}) \cdot \mathbf{n}$ is the normal component of mode μ at node point $\mathbf{x}_{\nu}$ and $\mathbf{d}(\mathbf{x}_{\nu}, f) \cdot \mathbf{n}$ is the experimentally-measured normal surface displacement at frequency f. Because the normal modes from the finite element analysis are orthonormal, the modal assurance criteria will approach unity if a mode shape closely resembles an operating deflection shape, and will approach zero otherwise. In the MAC definition, the two data sets to be compared are defined over similar meshes, which is rarely possible because the experimental data is almost always measured over a much coarser grid than for the finite element analysis. To make the meshes coincide, we can either interpolate the finite element mode shapes onto the coarser experimental mesh or we can interpolate the experimental data onto the more refined finite element mesh. The highest possible accuracy is maintained by using as many data points as possible, and thus, given the choice, we want to interpolate the experimental data onto the numerical finite element mesh. We will now document the general procedure used to interpolate the data and perform the MAC calculations.

The first step in the analysis is to generate overlapping experimental and numerical meshes. This straightforward task can be accomplished using a finite element preprocessor such as IDEAS or FEMAP. The second step is to determine, in a general way, where the nodes for the numerical mesh are located on the experimental mesh. We divide this task into two steps. First, we determine if each of the node points for the finite element analysis is located above one of the elements of the experimental mesh, and if so, we then use a nonlinear optimization routine to determine its precise location on the element's surface in terms of analytical parameters.

To determine if a node from the finite element analysis is located above an element, we compute a number of its geometrical characteristics. For each element edge, we first compute the unit vector directed along its length, with the vectors proceeding in the same direction around the element as the node numbers. We next determine the outward surface normal direction at each node by taking the cross product between the unit vectors for the two intersecting edges. Averaging the outward normal direction for the nodes then yields the outward normal for the element as a whole. Obviously, the computed normal is only approximate for nonplanar quadrilateral elements. We next determine the unit vector normal to each of the edges in the plane of the element by taking the cross product between the element

normal and the edge directions. We will subsequently refer to this as the edge normal. Because of the element numbering scheme, the edge normals point into the element's interior, as illustrated in Figure 7. All of these calculations are performed initially because they are static for each of the elements.

Knowing the geometry of each of the elements, it is easy to determine if a point lies above an element. (In this context "above" means within the element borders.) For each edge, we compute the dot product between the edge normal and the vector from the point to one of the edge nodes. Because edge normals point into the interior of the element, a positive value indicates the point lies on the same side of the edge as the element. If the dot product is negative for any of the edges, then the point lies outside of the element borders and is thus not "above" it. Because it is possible for the point to lie above several elements simultaneously, we also keep track of the approximate distance of the point from the element plane, and choose the element with the smallest distance. Also, we compute the ratio of this distance to the overall characteristic element size and reject the element if the ratio is larger than 1/2. Thus, for the MAC calculations to work properly, the surfaces for the meshes do not have to match exactly, but the discrepancies cannot be larger than the element dimensions for the experimental mesh.

Once we have determined that a node point for the finite element mesh lies above the surface of an element, we next have to determine its precise location in terms of the parameters used to interpolate the surface velocity data. For a quadrilateral element, the element surface can be written in terms of the nodal coordinates $\mathbf{x}_\mu$ as

$$\mathbf{x}(\xi,\eta)=\frac{1}{4}\sum_{\mu=1}^{4}\left(1+\xi_\mu\xi\right)\left(1+\eta_\mu\eta\right)\mathbf{x}_\mu$$

where the values for the ξ_μ and η_μ are $\xi_{1,2,3,4}=-1,-1,1,1$ and $\eta_{1,2,3,4}=-1,1,1,-1$, respectively. Each point on the surface corresponds to a unique value for the ordered pair (ξ, η), and the element surface is bounded by $-1<\xi,\eta<1$. Similarly for a triangle, the element surface can be written in terms of nodal coordinates as

$$\mathbf{x}(\xi,\eta)=\xi\,\mathbf{x}_1+\eta\,\mathbf{x}_2+\left(1-\xi-\eta\right)\mathbf{x}_3$$

where $\xi=A_1/A$ and $\eta=A_2/A$, as illustrated in Figure 8. Each point on the surface corresponds to a unique value for the ordered pair (ξ, η), and the element surface is bounded by $0<\xi,\eta<1$. Once we determine the location of the point in terms of the parameters, then it is a simple matter to linearly interpolate the experimental nodal data and determine its value at the point of interest.

If all the elements were planar, we could simply calculate the values for the interpolation parameters by determining the point in the element plane closest to the finite element node point. However, since quadrilateral elements can be nonplanar, a much more sophisticated algorithm is required. In our implementation, a nonlinear search algorithm is used to find the optimum values for the interpolation parameters to minimize the distance between the element surface and the node point. Because the distance is a squared function of the parameters, the process is relatively straightforward, with no chance of the search routine finding a local, but not a global, minimum point. Powell's method is used for the calculations and the required subroutines were taken from the book "Numerical Recipes" by Press, et al. [2]. Once the interpolation parameters have been determined, the normal surface velocity can be interpolated using formulas similar to those describing the element surface in terms of the nodal locations. Although this algorithm is somewhat complicated and computationally-intensive, it only has to be performed once at the start of the analysis, with the interpolation parameters and element numbers stored

for the subsequent calculations. At each measurement frequency, the experimental data is then interpolated onto the finite element nodes and the modes shapes can be directly multiplied by the experimental data to calculate the modal assurance criteria.

To demonstrate the calculations, we will perform a MAC analysis on the right-side door of the enclosure. The door was removed from the enclosure and tested hanging from a "bungee cord" to simulate free boundary conditions. Figure 9 shows views of the experimental mesh with 64 measurement locations and the accompanying finite element mesh with 1751 nodes. The finite element mesh is shown from the door's backside to illustrate the raised stiffening panel. The experimental data was measured only over the door's front side. Figures 10 and 11 show: (1) the experimental data at a modal peak before it has been interpolated onto the finite element mesh, (2) after it has been interpolated, and (3) the accompanying finite element mode shape. The close resemblance between the various datasets demonstrates that the interpolation scheme is working properly. Figure 12 shows the calculated MAC values for the first ten modes as a function of frequency on a dB scale, such that MAC = 0 indicates perfect agreement between the experimental data and a mode shape. The peak values are below their maximum possible value because the stiffening panel is not included in the experimental representation of the door. Following the analogy with a coherence function, we can also separate out the vibration response into contributions from the various modes simply by multiplying the MAC values by the overall vibration level. Figure 13 shows the contributions to the overall response from each of the finite element mode shapes. Once separated into contributions from the individual modes, the modal parameters can be determined, as will be discussed in the next section.

IDENTIFYING MODAL CHARACTERISTICS

Apart from the MAC calculations, it is also desirable to be able to compute resonance frequencies and modal structural damping from experimental transfer function measurements. This type of calculation falls under the general category of "nonlinear parameter estimation". The basic idea is to assume the transfer function between input force and vibration response near the resonance peaks can be written in the form

$$H(f) = \frac{A}{\omega_\mu^2 (1 - i\eta_\mu) - \omega^2}$$

where the ω_μ are the resonance frequencies, the η_μ are the structural damping levels, and A is a complex constant. These three parameters are then determined for each resonance peak by matching the analytical function to the experimental data in a least square sense. Because the transfer function data is complex, we have to match both the real and imaginary components simultaneously to correctly determine the parameters. The subroutines required to perform the calculations were adapted from the Levenberg-Marquardt algorithm given by Press et al. [3].

The basic idea of the Levenberg-Marquardt algorithm is to assume a quadratic form for the objective function (which represents the least square difference between the analytical function and the experimental data) and jump to the correct value for the minimum knowing the derivatives of the analytical function with respect to the parameters. For a linear optimization problem, this technique yields the minimum in a single jump. For a nonlinear optimization problem, the objective function is not necessarily a quadratic function of the parameters, and the attempted minimization may actually increase its value. When this occurs, the algorithm switches to a steepest descent approach and attempts to step

"downhill" to a region where the objective function is quadratic. After each downhill step, the program tries the quadratic optimization scheme, and if it fails, the step size for the steepest descent algorithm is increased. The algorithm requires the analytical evaluations of the gradients, which are input to the program using subroutine calls.

For our particular problem, we begin by performing a MAC analysis to separate the modes from each other. This simplifies the process because we don't have to include off-resonance modal contributions in the transfer function representation. The more general representation for the transfer function is discussed in the documentation for the modal analysis program StarModal [4]. The three parameters to be determined for each resonance peak are A, ω_μ, and η_μ, and thus we need to analytically evaluate the derivative of the transfer function with respect to each parameter. Because the algorithms supplied in Numerical Recipes are for real functions, we first separate the transfer function into real and imaginary parts, and then take derivatives with respect to the real and imaginary components separately. The objective (or merit) function becomes

$$\chi^2(\mathbf{a}) = \sum_{\nu=1}^{N} \left[\frac{\left| \mathrm{Re}\{H(f_\nu)\} - \mathrm{Re}\{\overline{H}(f_\nu;\mathbf{a})\} \right|^2}{\sigma_\nu^2} + \frac{\left| \mathrm{Im}\{H(f_\nu)\} - \mathrm{Im}\{\overline{H}(f_\nu;\mathbf{a})\} \right|^2}{\sigma_\nu^2} \right]$$

where the f_ν are the measurement frequencies and **a** is a vector made up of the parameters. Also, σ_ν is the standard deviation in the vth data point, which is presumed to be known and the transfer function H with an "overbar" represents the analytical model for the resonance peak. In our calculations, we have taken the standard deviations to all be unity for lack of a better estimate. With this definition for the objective function, it is a simple matter to analytically determine the required derivatives.

The only remaining task is to decide how to truncate the experimental transfer function data before applying the nonlinear parameter estimation routine. In the modal analysis software StarModal, the user manually selects the frequency range for each mode or set of modes. To simplify the analysis, we instead use the results from the MAC analysis to automatically choose the frequency range of interest for each mode. Because the structural damping can be defined in terms of the frequency difference between the 3 dB down points (which span the half power bandwidths about the resonance frequencies), we expect that we only need to include the data within 3 dB of the peak value to correctly predict the structural damping. In the actual analysis, we include data within 6 dB of the peak values to provide some margin for error if the experimental data is sparsely-sampled in frequency. The center frequency for each of the resonance peaks is determined by searching for the maximum MAC value over the whole frequency range. Of course, this may be problematic for modes that are not excited into vibration because the drive point lies on or near a nodal line.

To demonstrate the calculations and validate the predictions, we will apply the analysis to one of the prototype shelves, as illustrated in Figure 14 where it is shown resting on bubble paper to simulate free boundary conditions. Comparisons between the measured and fitted transfer function data for one of the resonance peaks are shown in Figure 15. The results show that our analytical representation for the transfer function is adequate and that the nonlinear parameter estimation routines are working properly. To facilitate comparisons between the measured transfer function data and a numerical finite element model developed in a separate effort, the computer program outputs the resonance frequency ratios (numerical/experimental) for each of the modes. Figure 16 shows a plot of the resonance frequency ratios for prototype shelf 1. To validate the structural damping predictions, Figure 17 shows a comparison between StarModal and the present predictions. The close agreement between the two sets of predictions further demonstrates that the nonlinear parameter estimation routines are properly implemented. Because

StarModal relies on the user to identify the frequency ranges where the modes are located, it is possible for "buried" modes to be skipped. No such problem occurs in our analyses because the MAC analysis can successfully separate modes with relatively small amplitudes. The main problem still to be addressed is how to filter the structural damping resonance frequency data to ensure that the results are meaningful.

To obtain more refined predictions, it is possible to measure transfer function data for multiple drive points. This allows the "complex mode indicator function" (CMIF) to be used to analyze the data and determine the modal properties, as discussed by Phillips, et al. [5]. The CMIF analysis is based on the singular value decomposition (SVD). Although considerably more effort is required to implement a CMIF analysis, in some situations it may be necessary to obtain reliable predictions.

EXPERIMENTAL MEASUREMENTS ON THE ENCLOSURE

Having documented the theoretical techniques used in finite element modeling and validation, we will now apply the techniques to the full enclosure. Before we can perform the analysis, we must first make detailed measurements of its structural vibrations. A shaker mounted vertically on the right-center spar of the second shelf provided the input force for all the measurements, and a force gauge mounted between the shaker and the spar was used to normalize the data to unit input force. Figure 18 shows the experimental mesh, where each node corresponds to one of the measurement locations. In constructing the mesh, numerical finite element models were used to position the node points, thus ensuring the experimental mesh overlies the numerical meshes. A Polytec scanning laser vibrometer was used to measure the outer skin and accelerometers were used to measure each of the shelves. It would have been preferable to measure the whole enclosure using a single measurement technique, but the interior shelves were not accessible for laser measurements, and it would have been very tedious and time consuming to measure the vibrations of the outer skin with accelerometers.

Unfortunately, we did not recognize the need for shelf measurements during the initial laser vibrometer measurements, and the enclosure was relocated during the interim and several months elapsed. Repeated attempts to duplicate the initial transfer function measurements at several locations on the enclosure skin using accelerometers yielded mixed results. Overall, the transfer functions closely resemble the original laser vibrometer measurements, but some differences occur over several frequency bands, most notably between 220-280 Hz, as shown in Figure 19. The reason for the change in the enclosure's structural dynamics is still unresolved. Despite this difficulty, most of the basic trends observed in the data will still be valid, but the specifics of the interaction between the shelves and outer skin might be called into question at some frequencies. If required, the laser vibrometer measurements could be repeated.

With that as a caveat, we will now proceed to discuss the results from the experimental measurements. Figure 20 shows a breakdown of the surface vibrations in the frequency range between 100 and 300 Hz. The frequency response of the driven shelf does not show significant deviations from the underlying response curve below its fundamental resonance frequency. However, near its fundamental resonance, the shelf clearly interacts strongly with the right side of the enclosure. Figures 21 and 22 show operating deflection shapes at eight of the resonance frequencies near the fundamental resonance of the driven shelf. For some of the modes, individual panels of the outer skin vibrate in isolation. For other modes, both the driven shelf and several panels of the enclosure skin vibrate in unison. The displacement profile at 176.6 Hz illustrates how vertical displacement of the center spar interacts with bending vibrations of the cabinet walls.

In addition to structural vibration measurements, a microphone was used to make pressure measurements near the enclosure's outer surface. This data proved to be very useful for two reasons: (1) it helped to identify the portion of the enclosure's skin responsible for each of the radiated noise peaks, and (2) it provided a quantitative assessment of the frequency ranges of primary interest for the finite element modeling. In general, it is not always possible to identify the radiating portion of the boundary surface in this fashion because the vibration spectrum is often overwhelmed by inefficiently radiating bending waves. However, in this case the radiated noise peaks correlate very well with the vibration peaks, both in terms of frequency and boundary surface location. Figure 23 shows the pressure data measured 6 inches from each side of the enclosure near their centers. The data in the figure is given in terms of source level relative to 0.0002 dyne/cm^2 at 1 foot. This reference is convenient for in-air measurements because it makes source and power levels approximately equivalent, as discussed by Ross [6]. The data below the lower end of the microphone's useable range at 50 Hz is truncated. The results also indicate that the front of the enclosure, which is made up primarily of two hinged doors and a screw-mounted panel, does not contribute significantly to the radiated noise. The most prominent noise peaks occur at approximately 230 and 300 Hz, and one of the main goals of the analysis is to explain why the sound radiation increases dramatically at approximately 200 Hz. To illustrate the correspondence between the vibration and radiated noise peaks, Figures 24 – 26 show comparisons between the integrated squared normal surface velocity over one side of the enclosure and the resulting surface pressure. The integrated squared normal surface velocity is plotted on a "power scale" by multiplying it by the characteristic impedance of air, which is given as $\rho c = \left(1.2\ kg/m^3\right)\left(343\ m/s\right)$. The figures also show the vibration amplitude when the integration is performed over the enclosure as a whole. The results demonstrate that the vibration and radiated noise peaks correspond closely to each other when one of the sides of the enclosure dominates the overall vibration spectrum.

VALIDATION OF THE RADIATED NOISE PREDICTIONS

We can gain some confidence in our radiated noise predictions by using the measured vibrations of the enclosure's outer skin as input to the boundary element program POWER. This allows us to assess the accuracy of the boundary element calculations independent of the accuracy of the finite element model. Figure 27 shows the boundary element mesh for the calculations. To assess the individual contributions from the sides of the enclosure, radiated noise predictions were made with all of the walls vibrating, and with each of the sides vibrating in isolation. By comparing these results to the measured pressures, we will be able to determine if hotspots on the enclosure walls can be identified from nearfield pressure measurements. Figure 28 shows the predicted source level (as computed from power level) as a function of frequency for each of the sides of the enclosure vibrating in isolation. These results cannot be directly compared to the measured pressures in Figure 23 because all of the walls of the enclosure were vibrating simultaneously during the measurements. Thus, because the vibration levels are low for the front of the enclosure, the pressures measured near the front face are likely due to the diffracted pressure fields from the left, right and back walls. Taking this into consideration, the predicted source levels compare very well with the measured levels shown in Figure 23, demonstrating that as long as the structural vibrations of the outer skin of the enclosure are accurately predicted, the radiated noise will also be predicted accurately by the boundary element calculations.

ANALYSIS OF THE ORIGINAL ENCLOSURE MODEL USING OFFSET-BEAM FOR STIFFENERS

The original finite element model of the enclosure supplied to ARL, as shown in Figure 29, relied heavily on beam element representations for stiffeners. This type of representation can yield accurate predictions at plate junctions, but great care has to be taken to properly represent the stiffener's interaction with the adjoining plates. Because this difficulty had not yet been recognized when the original finite element model was constructed, we might expect it to be deficient in this respect. Examining the model, we see that the stiffeners are connected to the shelves and cabinet walls only along the nodes at their juncture. This will severely reduce the moment transfer across plate junctions and the resulting bending vibrations of the cabinet walls. The goal of the analysis is thus to examine the vibration spectrum near the fundamental resonance of the driven shelf and determine how well the finite element model represents the interaction between the shelf and the enclosure walls.

The simplest way to assess the accuracy of the finite element predictions is simply to isolate the vibrations of each of the components, yielding plots similar to those given previously for the experimental vibration data. Figure 30 shows a breakdown of the vibrations for the original finite element model. In the model, the vibrations of the driven shelf dominate the response near its fundamental resonance frequency at 183 Hz, with the only significant interaction occurring very near the resonance. This differs considerably from the experimental data shown in Figure 20 where the vibrations of the right side of the enclosure increasingly dominate the overall response above the shelf's fundamental resonance. Unfortunately, this method for analyzing the data gives a good qualitative assessment of the model's accuracy, but yields no indication of how to modify the model to increase its fidelity.

A MAC analysis is more computationally intensive, but also yields much more information. To perform the analysis, the laser vibrometer and accelerometer measurements were combined together to give a complete vibration profile at a series of frequencies. The experimental data is then interpolated onto the finite element mesh and compared individually to the numerical mode shapes. To check that the experimental data is being correctly interpolated onto the finite element mesh, the nodal vibrations were written out and animated in a preprocessor. The MAC analysis produces two frequency response curves for each finite element mode, one representing the MAC amplitude and the other representing the modal contribution to the overall vibration response. To determine the dominant modes in a frequency band of interest, it is necessary to search through all the data and identify the modes with the largest MAC amplitudes. Figures 31 and 32 show plots of the MAC amplitude and modal amplitudes for the four dominant modes as a function of frequency in the range between 100 and 300 Hz, respectively. Unfortunately, none of the MAC values approach unity, and only mode 22 spans a single resonance peak. Thus only mode 22 represents a "pure" mode from the experimental measurements. Figure 33 shows the mode shapes of the four dominant modes from the finite element analysis. Comparing the mode shapes to the operating deflection shapes shown in Figures 21 and 22, we can conclude that the interaction between the shelves and the enclosure's outer skin is not well represented in the finite element model. Also, both the left and right cabinet walls vibrate in unison for many of the finite element mode shapes, indicating a higher level of degeneracy than that present in the actual enclosure.

To determine if the enclosure model is too soft or stiff, we can compare the resonance frequencies for the finite element modes to the frequencies where the MAC amplitude shows a peak. The experimental resonances occur at 147, 178, 180, 190, 200, and 230 Hz while the numerical modes occur at 134, 184, 236 and 242 Hz, respectively. This shows that the finite element model is only slightly too soft for three

of the modes, but that it is considerably too soft for the modes at 180, 190, and 200 Hz. We might thus try to modify the finite element model to differentially stiffen the "soft" components and soften the "stiff" components.

Finally, the vibrations of the outer enclosure skin were input to the boundary element code POWER to make radiated noise predictions. Figure 34 shows the boundary element model of the enclosure's outer skin and Figure 35 shows the resulting pressure predictions. The calculations are successful in predicting the dramatic increase in the radiated sound power near the fundamental resonance frequency of the driven shelf, but many of the details differ from the measurements. One of the main inconsistencies can easily be explained. In the numerical predictions, the front of the enclosure contributes significantly to the response, and even dominates the radiated noise at the fundamental resonance of the driven shelf. However, this discrepancy is somewhat expected because the doors of the enclosure are rigidly connected to its frame in the finite element model, whereas in reality the doors are hinged on one side and screwed down on the other side. Additionally, the doors are further isolated from the enclosure by means of a rubber gasket. We thus expect the finite element model to overpredict the vibrations and radiated noise from the front of the enclosure. Overall, we would assess the original finite element model as useful for radiated noise predictions, but not in specific details. For example, the model would probably be useful in estimating how the radiated noise would change if the mechanical properties and geometry of the shelves were changed, but would not be useful in making absolute radiated noise predictions at a specific frequency.

ANALYSIS OF THE REVISED ENCLOSURE MODEL USING PLATE ELEMENTS FOR STIFFENERS

In the revised finite element model of the enclosure, almost all of the beam elements have been replaced with plate elements. The original intent was to better represent the actual geometry and to simplify the process of establishing convergence for several different meshes. Unfortunately, the meshing process was more time consuming and required more user interaction than anticipated, such that it was impractical to generate and test several meshes. Figure 36 shows the finite element model for the enclosure, both with and without the front door and bottom front panel. The plate element representation is also somewhat unrealistic because it models the thin cabinet plating as solidly welded to the shelves, whereas the actual cabinet plating is only spot-welded at several locations. Thus, we expect the resulting finite element model to be overly-stiff. The goals of the analysis are to establish the accuracy of the resulting finite element model and to see how it compares with the original model.

The first step is to isolate the vibrations of each of the enclosure's component parts, yielding plots similar to those given previously for the experimental vibration data. Figure 37 shows a breakdown of the vibrations for the revised finite element model. The results show that the driven shelf dominates the response near its fundamental resonance frequency at 168 Hz, but that there is considerable interaction with the right side of cabinet both at the resonance and slightly higher in frequency. In this respect, the revised model better duplicates the experimental measurements shown in Figure 20. However, there are still considerable discrepancies between the numerical and experimental results.

A MAC analysis is again useful as a way of objectively comparing the numerical and experimental results and providing guidance in how to improve the finite element model. Figure 38 shows the MAC amplitudes and Figure 39 shows the mode amplitudes for the four dominant modes as a function of frequency between 100 and 300 Hz. Overall, the results are very similar to those for the original model, but with slightly lower overall amplitudes. Figure 40 shows the finite element mode shapes for the four

dominant modes. They correctly show strong interactions between the shelves and the cabinet plating, but do not mimic the operating deflection shapes at the resonance frequencies very well. In particular, the left side of the enclosure is much more responsive in the finite element model than in the corresponding experimental data. This difference is primarily responsible for the peak MAC values being considerably below unity.

Comparing the frequencies for the peak MAC values to the resonance frequencies for the finite element modes, we can confirm our earlier expectation that the finite element model is considerably too stiff. The experimental resonances occur at 147, 178, 180, 190, 200, and 230 Hz while the numerical modes occur at 214, 166, 272 and 299 Hz, respectively. Three of the four modes are considerably higher in frequency than their experimental counterparts, but surprisingly, the fundamental mode of the driven shelf is slightly low. While the resonance frequencies for the cabinet plating are considerably in error, the modes correctly show strong interactions with the driven shelf. We can thus conclude that the revised finite element model thus improves upon the original model in its representation of the interaction between the shelves and the cabinet plating.

Finally, the vibrations of the outer enclosure skin were input to the boundary element code POWER to make radiated noise predictions. Figure 41 shows the boundary element model of the enclosure's outer skin and Figure 42 shows the resulting pressure predictions. Because the front doors and panel are soft mounted to the enclosure with springs in the revised model, the front of the enclosure no longer contributes significantly to the radiated noise, which is consistent with the data in Figure 28. The dramatic increase in the radiated sound power near the fundamental resonance frequency of the driven shelf is again predicted, but now the power output continues to rise until approximately 300 Hz. The shift in the radiated noise peaks to higher frequencies is expected because the finite element model has already been shown to be too stiff. Similar to the original finite element model, we would assess the revised model as being useful for assessing general trends in the radiated noise predictions, but not necessarily in specific details.

The finite element analysis has helped us to understand several trends observed in the experimental data. First, the interaction between the shelves and the cabinet plating has been demonstrated to be a significant source of radiated noise, especially at frequencies above the fundamental resonance of the driven shelf. Second, the structural analysis, and not the boundary element analysis, has been shown to be the main source of inaccuracy in the radiated noise predictions. One possible way of increasing the overall accuracy of the structural analysis would be to assemble both the physical enclosure and the finite element model in pieces, using experimental measurements to adjust the model at each stage of construction. Although this would undoubtedly produce better and more consistent finite element models, it would also be somewhat impractical except as a means of providing modeling guidance. Third, the front of the enclosure has been shown to not contribute significantly to the radiated noise. It differs from the back and sides of the enclosure because (1) the doors are hinged and soft mounted to the frame, and (2) the doors are not intimately connected to the shelves except through the frame. The enclosure could easily be redesigned so that its side and back walls are mounted similar to the front doors. The attendant reduction in the enclosure's overall structural stiffness should probably be acceptable considering that it is presently overdesigned.

ANALYSIS OF THE PROTOTYPICAL SHELVES

Four prototypic shelves were developed to provide a platform for demonstrating structure concepts and potential shelf design/enclosure modifications. Figure 14 shows one of the shelves resting on bubble paper. The shelves were modeled using techniques similar to those used for the enclosure, with the ultimate goal of developing a validated finite element model of a shelf with and without attachments. In this section, we will examine the various base shelf configurations (i.e. without attachments) and document the agreement between experimental vibration measurements and finite element predictions. Also, radiated acoustic power predictions are given for the both configurations using the surface vibration profiles as input.

The four prototypical shelves were constructed with different plate thicknesses and fastener types to test how these parameters alter the resulting vibration profiles. As listed in Table 2, the four configurations were chosen to give permutations of two plate thicknesses and attachment methods. Each configuration employs a frame made out of four separate components, each with an L-shaped ("angle") cross-section. These components act as stiffeners and are attached to a flat plate using either stainless steel or nylon screws. The attachment screws are located on one-inch centers for all cases. No welds were used during the assembly. Figure 43 shows a typical shelf frame without an attached plate showing its overall dimensions. Shelf height is not shown in this figure since this dimension varies with plate thickness and the frame's dimensions. The attachment holes in the plate are threaded using heli-coils to make the shelves more durable for the many anticipated assemblies/disassemblies. In the initial tests documented here, the shelves were tested resting on bubble-wrap to simulate free-free boundary conditions. In subsequent tests, the shelves will be mounted to four legs extending from a massive base structure, as illustrated in Figure 44. Furthermore, additional plating may be attached to the shelves in subsequent tests to simulate the interaction between the shelves and the enclosure walls.

The shelf finite element models were developed using a combination of plate and bar elements, as illustrated in Figure 45. Plate elements are used to model the shelf plates while bar elements attached along the plate boundaries are used to model the stiffeners. Because the prototype shelves do not contain angles and plates meeting at right angles, bar (or beam) elements should yield reasonably accurate vibration predictions, as demonstrated previously. The screws are assumed to provide a rigid connection between the frame and plate, and the region where the frame and plate overlap is modeled in the finite element analysis using a single plate element with the combined thickness of the frame and plate. Thus, the finite element models do not account for differences in the attachments, except possibly through the specified structural damping. This approximation should be valid over the frequency range of interest, as will be confirmed by directly comparing the predicted structural resonance frequencies and mode shapes to experimental predictions. Damping levels used for each of the models are mean values representative of the damping levels extracted from experimental data using the program StarModal. Figure 46 shows the damping for shelves 1 and 4 and Figure 47 shows the damping for shelves 2 and 3. The only difference between shelves 1 and 4 and shelves 2 and 3 is the material used for the screws. Clearly, the nylons screws provide more structural damping than the steel screws.

To test the accuracy of the finite element models, the predicted normal mode vibration profiles were compared to experimental measurements using a MAC analysis. The first six flexible mode shapes for Shelf 3, not including the six rigid body modes at approximately 0 Hz, are shown as color contour plots in Figure 48. The measured results consist of transfer functions from impact hammer tests performed with the shelf resting on bubble wrap to simulate free boundary conditions. The transfer functions represent the ratio of the force input at one point to the resulting acceleration at another point. For the prototypic shelf tests, the accelerometer remained stationary and the drive point was varied across the surface of the

plate for a total of 256 points. It is easiest to vary the input force location for impact hammer testing because the force gauge resides within the hammer and it can be easily moved from point-to-point on the surface, as illustrated in Figure 49. This contrasts with the laser vibrometer measurements where the force was input at a stationary location using a shaker and the response point varied over the enclosure's surface. The resulting vibration data was then interpolated from the experimental mesh onto the finite element mesh using the procedure described previously. A MAC analysis was then performed using the interpolated experimental data and numerical vibration predictions as input. The results of the MAC analysis for each of the prototype shelves are shown Figures 50-53. The correspondence between the numerically-predicted and experimentally-measured mode shapes is excellent, as can be judged by the MAC values near unity at each of the resonance peaks.

Radiated noise predictions for each shelf were then made for both the empirical and predicted vibrations using the boundary element program POWER. Results for shelves 1 and 2 are shown in Figure 54 and results for shelves 3 and 4 in Figure 55. As can be seen in these figures, the radiated noise magnitudes agree very well. However, there are some discrepancies in the peak locations, which is a result of differences in the predicted and measured resonance frequencies. Furthermore, the existence (or non-existence) of a peak is most likely a result of differences, albeit minimal, in the measurement/drive point location between the measured and predicted results. Because the accelerometer location for the tests does not coincide with a finite element grid location, the frequency response drive point may excite some modes that are not exited in the measurements, while other modes may not be excited at all. Neglecting these identified differences, discrepancies between the measured and predicted results would still exist due to both our inability to model all of the nuances associated with such built-up stiffened structures and the limitations associated with accurately measuring the structure's response.

In summary, the radiated power predictions compare very well with the predictions made using empirical data for all of the prototypic shelves. This agreement provides confidence in the shelf finite element models. Based on the results provided here, prototypic Shelf 3 has been chosen for future work involving the demonstration of vibration control and fuzzy structure concepts. This shelf was chosen over the others because of the relative accuracy at which both the predicted vibration amplitude and resonance locations matched the measured results.

SUMMARY AND CONCLUSIONS

Several important conclusions can be drawn from our research. First, the results have shown that the boundary element code POWER gives accurate noise predictions for the sound radiation from an enclosure in a straightforward manner if the surface vibration profile can be accurately determined. Second, the thin walls of the existing enclosure are highly coupled to the shelves though rotational degrees of freedom along their edges. Third, it is difficult to accurately model the vibrations of a complex built-up structure of this type, but the results can be very useful in helping to better understand basic radiation mechanisms. Overall, the results suggest that it should be possible to reduce the radiated noise from the enclosure by reducing the moment coupling between the shelves and the walls, which will be the subject of future research.

REFERENCES

[1] John M. Lee, Ed., "MSC / NASTRAN Common Questions and Answers," 2nd Ed., (MacNeal-Schwendler, Los Angeles, CA), 1993, pp. 69-72.

[2] W. H. Press, S. A. Teukolsy, W. T. Vetterling, and B. P. Flannery, "Numerical Recipes in FORTRAN," 2nd Ed., (Cambridge University Press, NY), 1992, pp. 406-413.

[3] ibid., pp. 675-683.

[4] Anonymous, "The STAR System User Manual – Part 4 Theory and Applications," 1994, pp. 1-37.

[5] A. W. Phillips, R. J. Allemang, and W. A. Fladung, "The Complex Mode Indicator Function (CMIF) as a Parameter Estimation Method," Proceedings of the Sixteenth International Modal Analysis Conference, pp. 705-710.

[6] D. Ross, "Mechanics of Underwater Noise," (Peninsula Publishing, Los Altos, CA), 1987, pg. 7.

Table 1. Comparison Between Resonance Frequency Predictions for Finite Element Models Using Different Element Types

Element Type	f1	f2	f3	f4	f5	f6
8-Node Hexas	119.24	248.57	336.69	504.95	555.64	660.25
20-Node Hexas	119.11	248.05	336.21	504.67	555.65	659.57
Plate – Fine Mesh	119.12	248.65	338.79	508.62	569.53	675.64
Plate – Coarse Mesh	118.67	249.78	337.13	508.70	569.74	673.91
Offset Beams	118.34	247.50	333.61	500.73	549.56	652.47

Table 2. Shelf Configurations for the Prototypical Shelves

Shelf #	Frame Angle Dimensions	Plate Thickness	Attachment Method	Plate and Angle Material
1	1" x 1" x ¼"	¼"	Stainless Steel Screws	6061 Aluminum
2	1" x 1" x 3/16"	3/16"	Nylon Screws	6061 Aluminum
3	1" x 1" x 3/16"	3/16"	Stainless Steel Screws	6061 Aluminum
4	1" x 1" x ¼"	¼"	Nylon Screws	6061 Aluminum

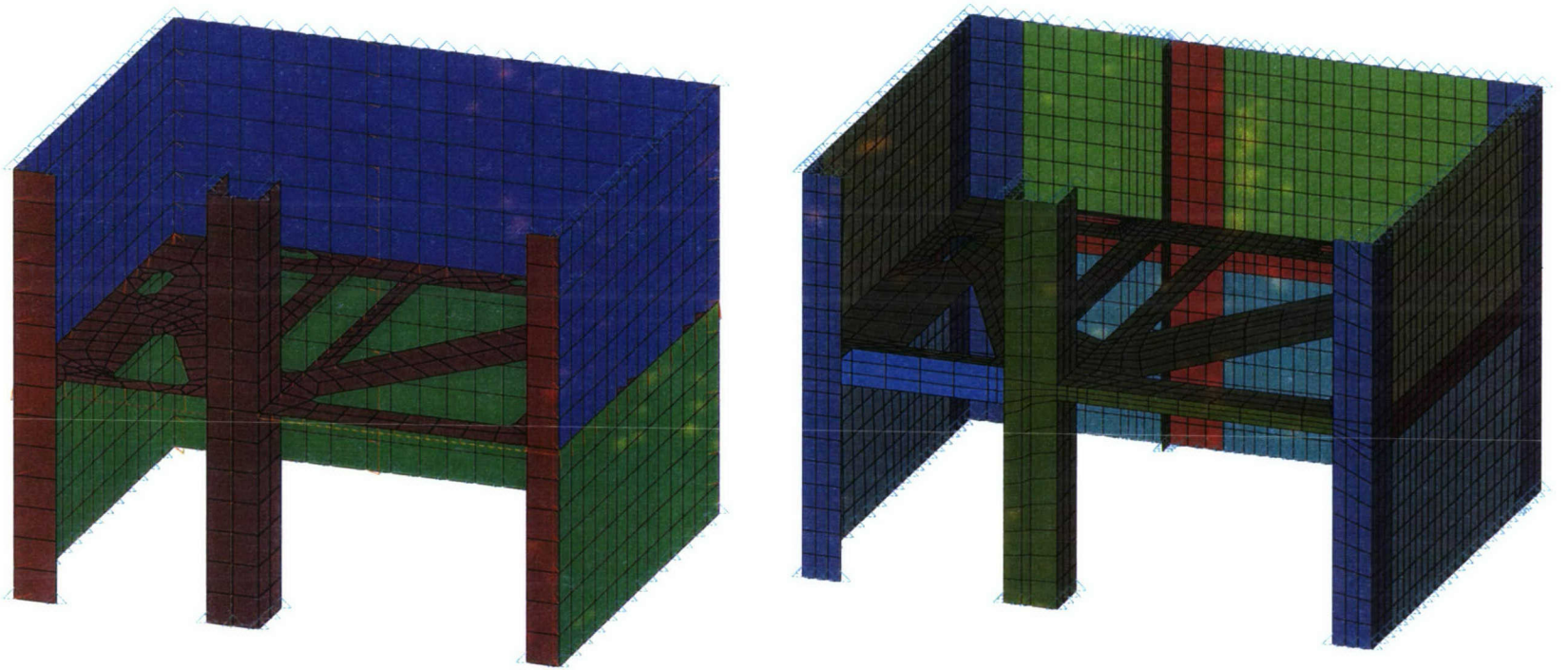

Figure 1. Comparison Between Offset Beam and Plate Element Models of One Shelf of the Enclosure

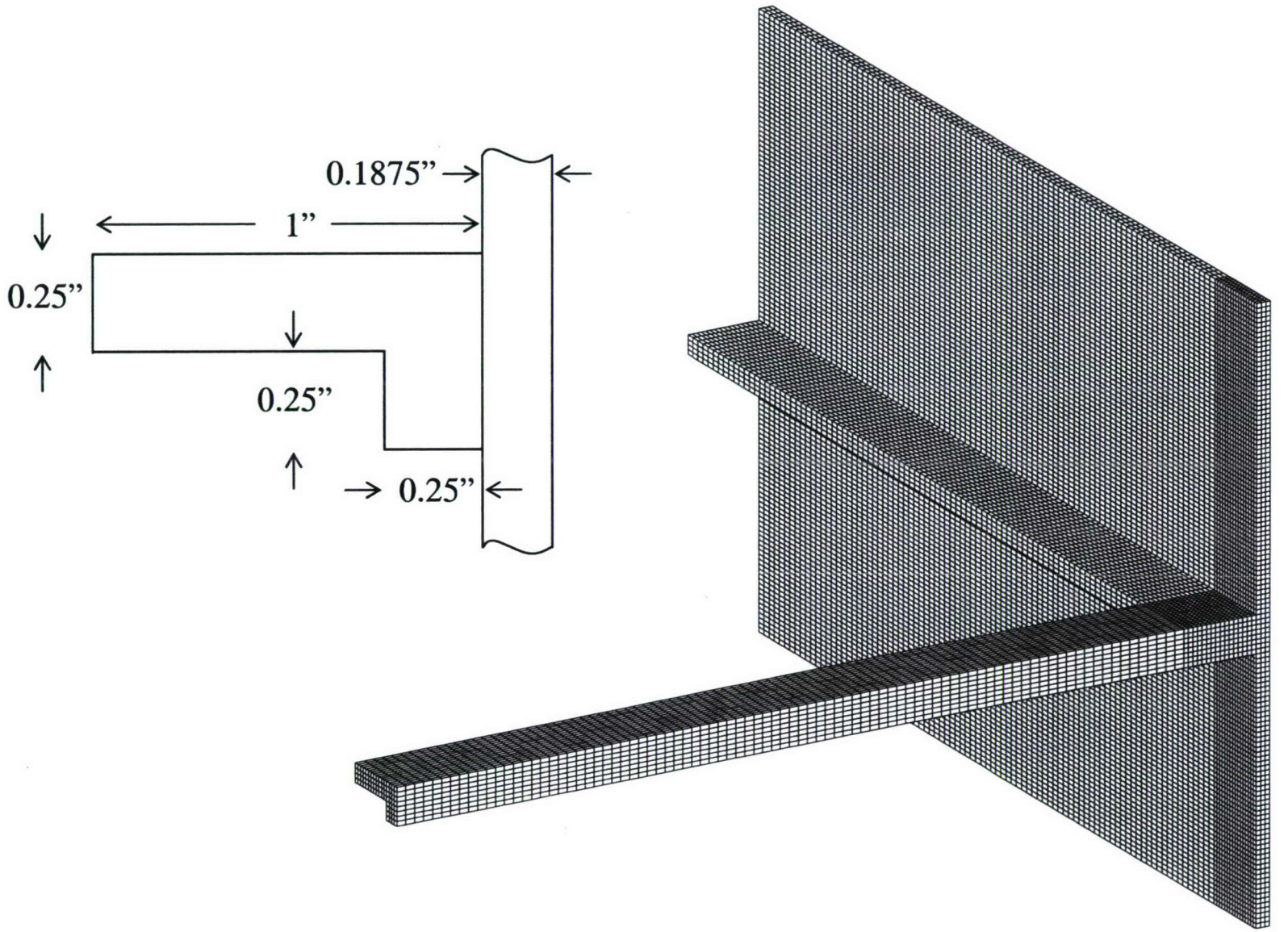

Figure 2. Finite Element Model of the Angle and Plate Example Problem Using 8-Node Hexahedral Elements

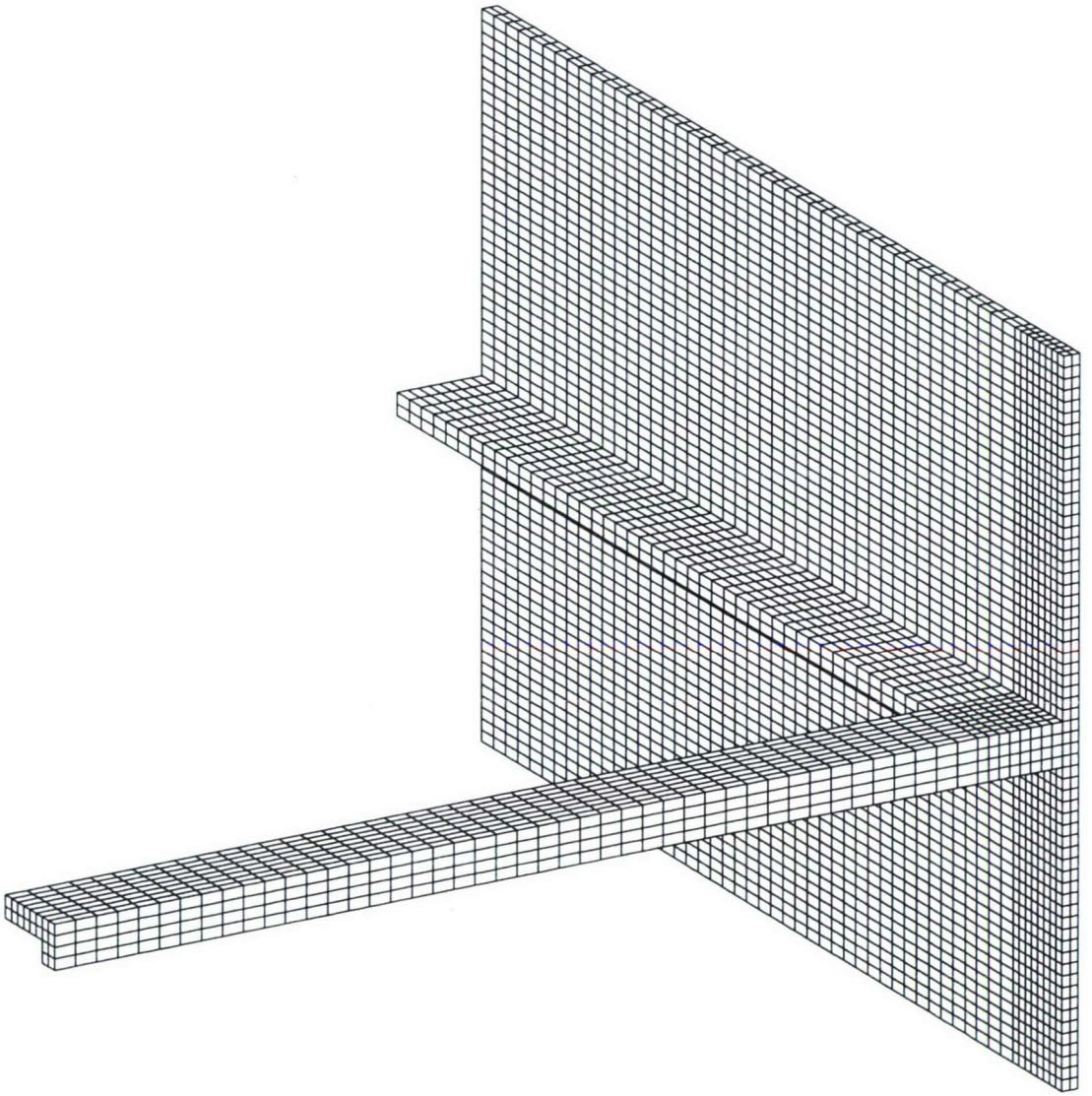

Figure 3. Finite Element Model of the Angle and Plate Example Problem Using 20-Node Hexahedral Elements

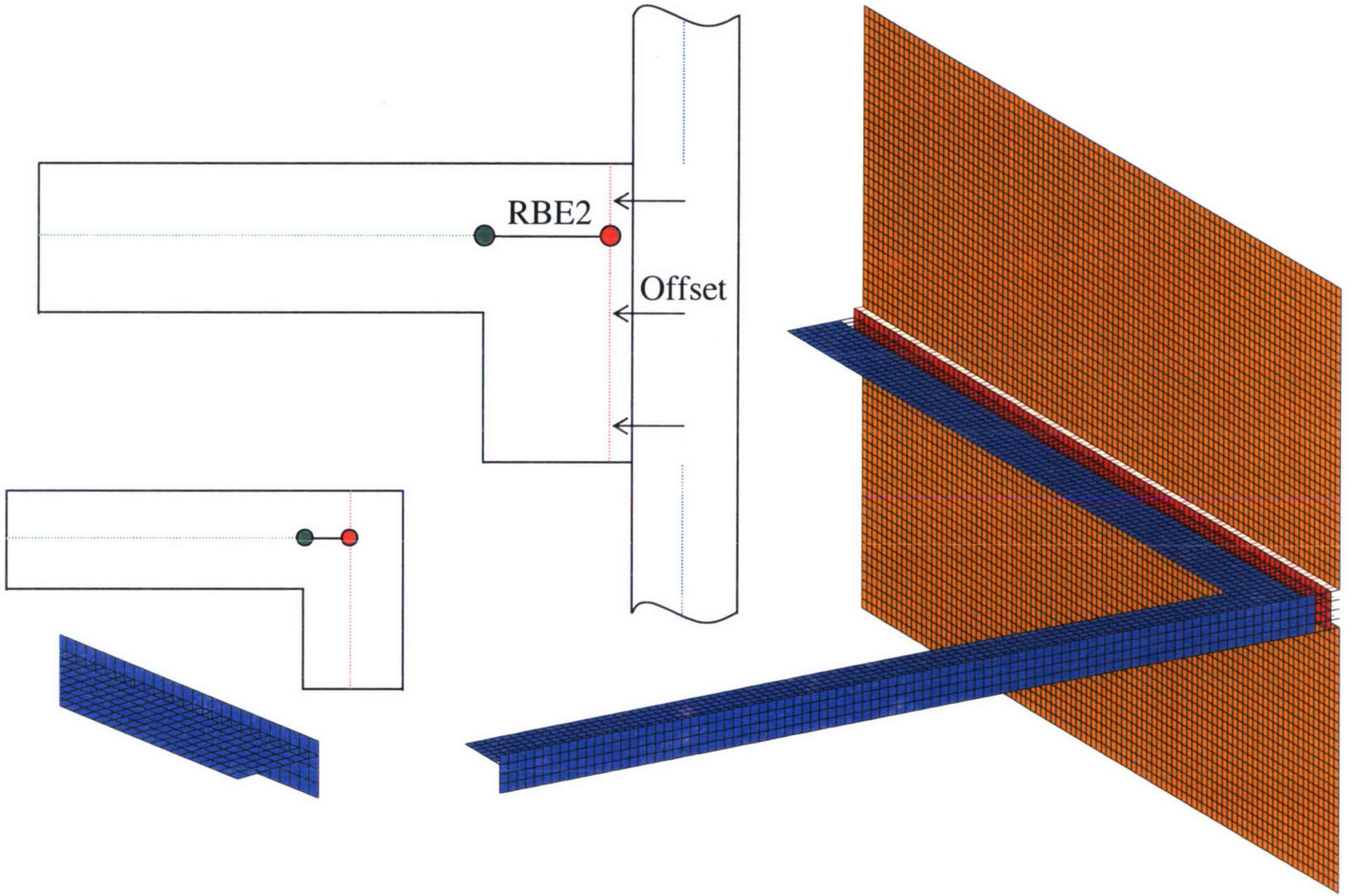

Figure 4. Finite Element Model of the Angle and Plate Example Problem Using Plate Elements

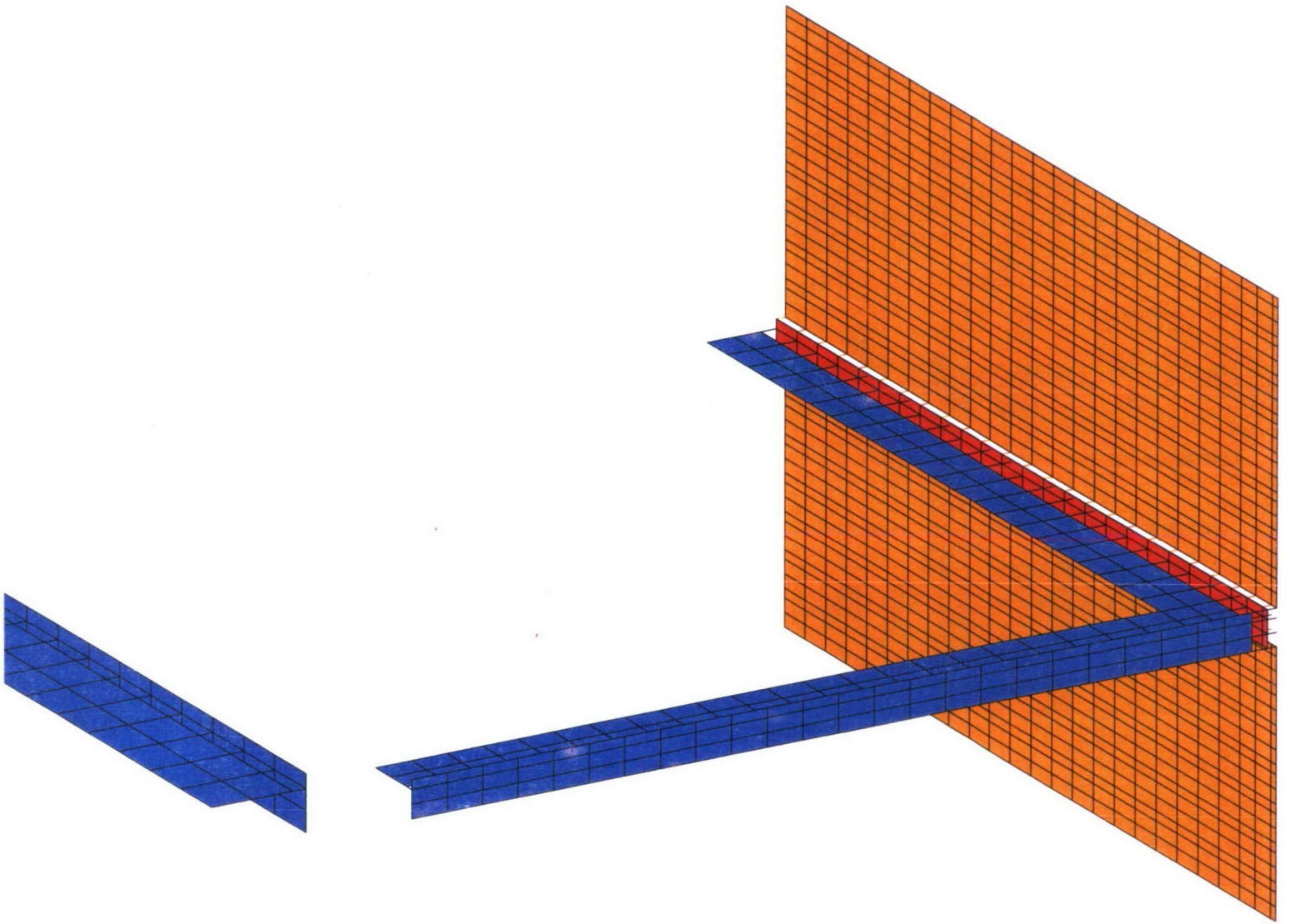

Figure 5. Realistically-Dense Finite Element Model of the Angle and Plate Example Problem Using Plate Elements

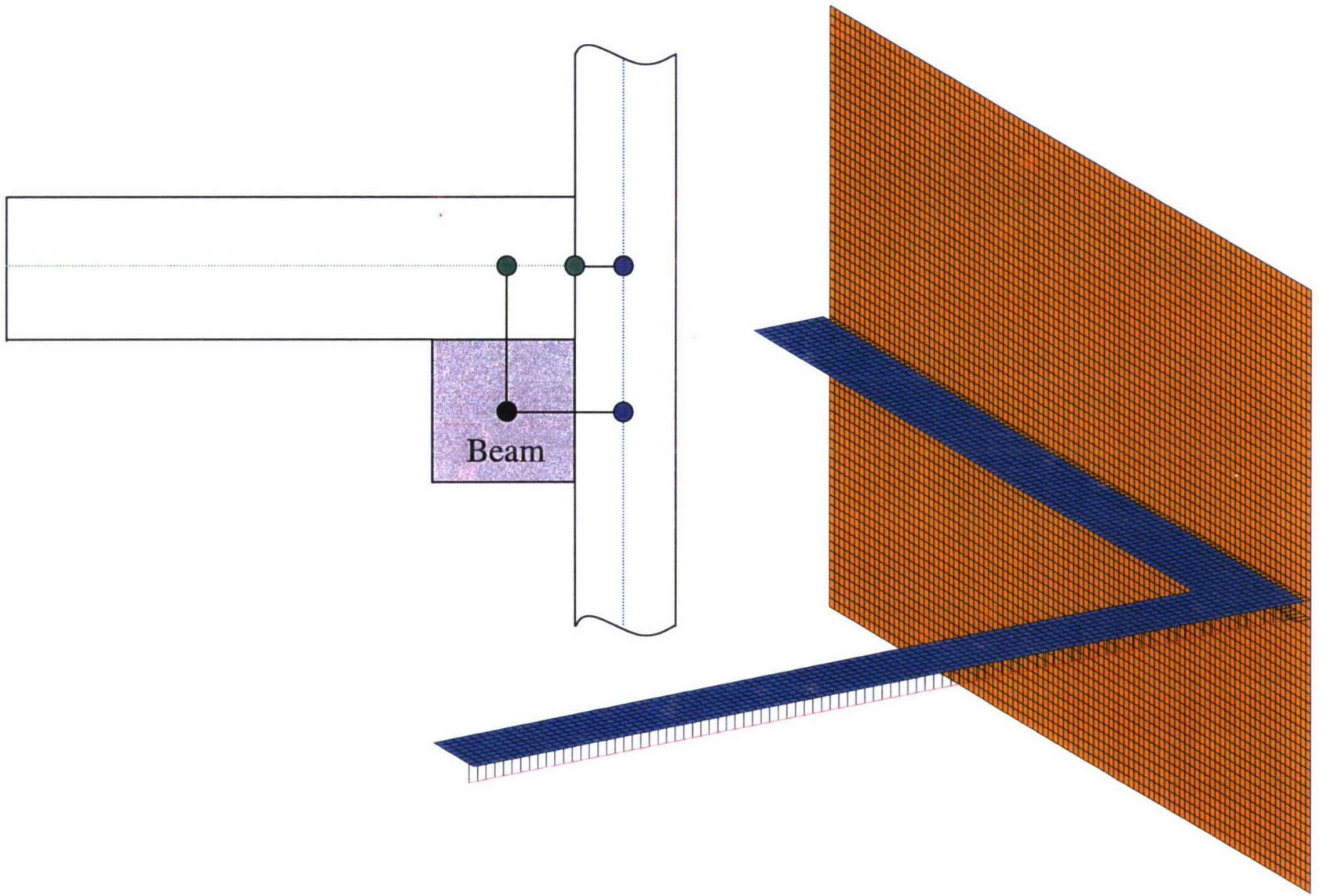

Figure 6. Finite Element Model of the Angle and Plate Example Problem Using Offset Beam Elements

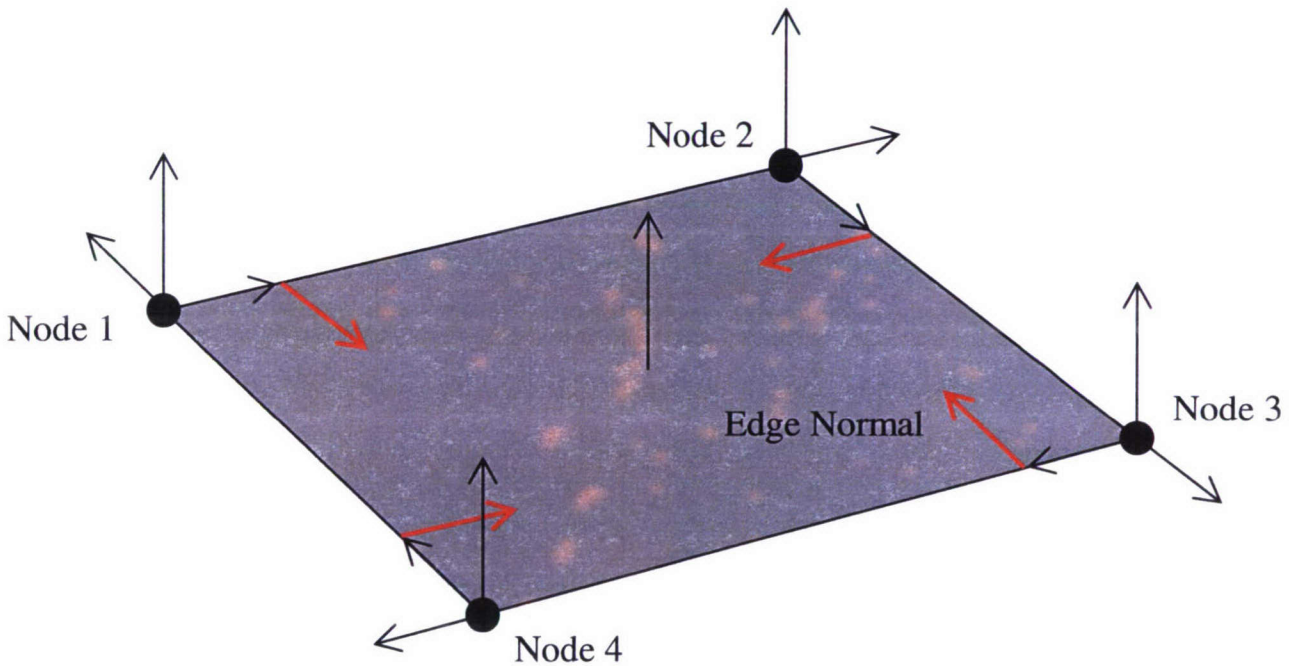

Figure 7. Illustration of the Edge Normals

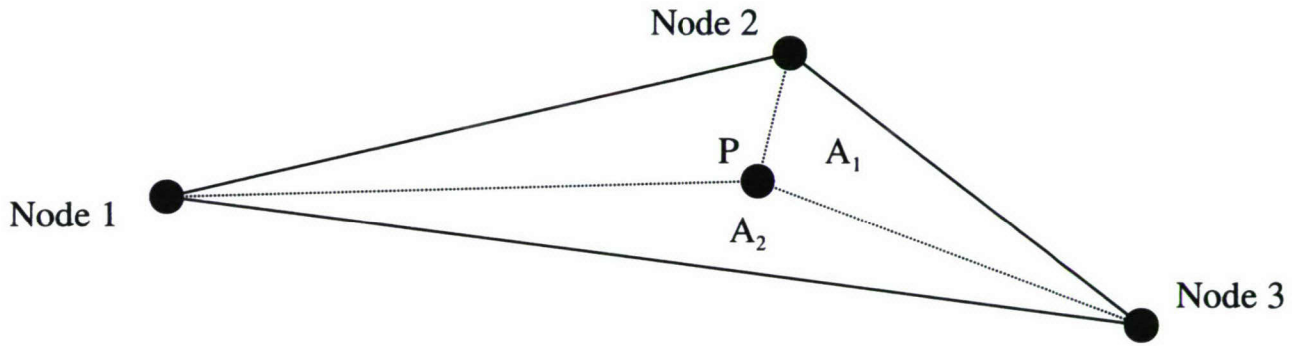

Figure 8. Illustration of the Areas of the Subtriangles

Finite Element Mesh

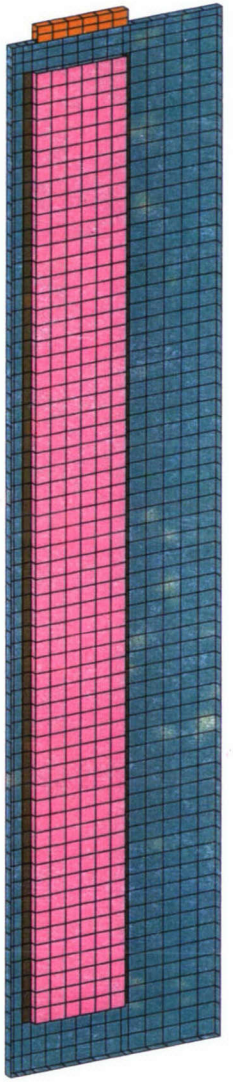

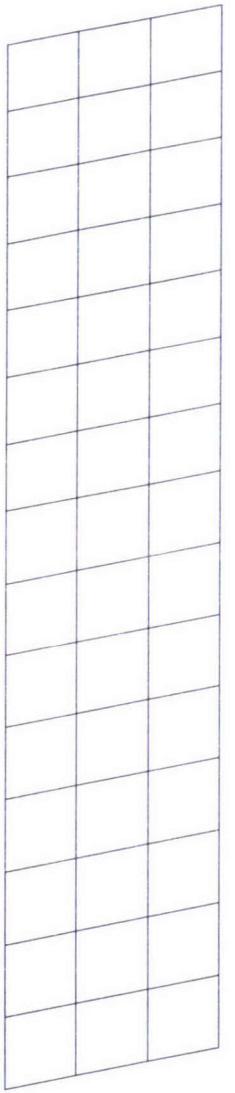

Experimental Mesh

Figure 9. Finite Element and Experimental Meshes for the Right-Side Door

Experimental Data for the Experimental Mesh

Experimental Data Interpolated onto the Finite Element Mesh

Numerical Mode #2 at 52.0 Hz

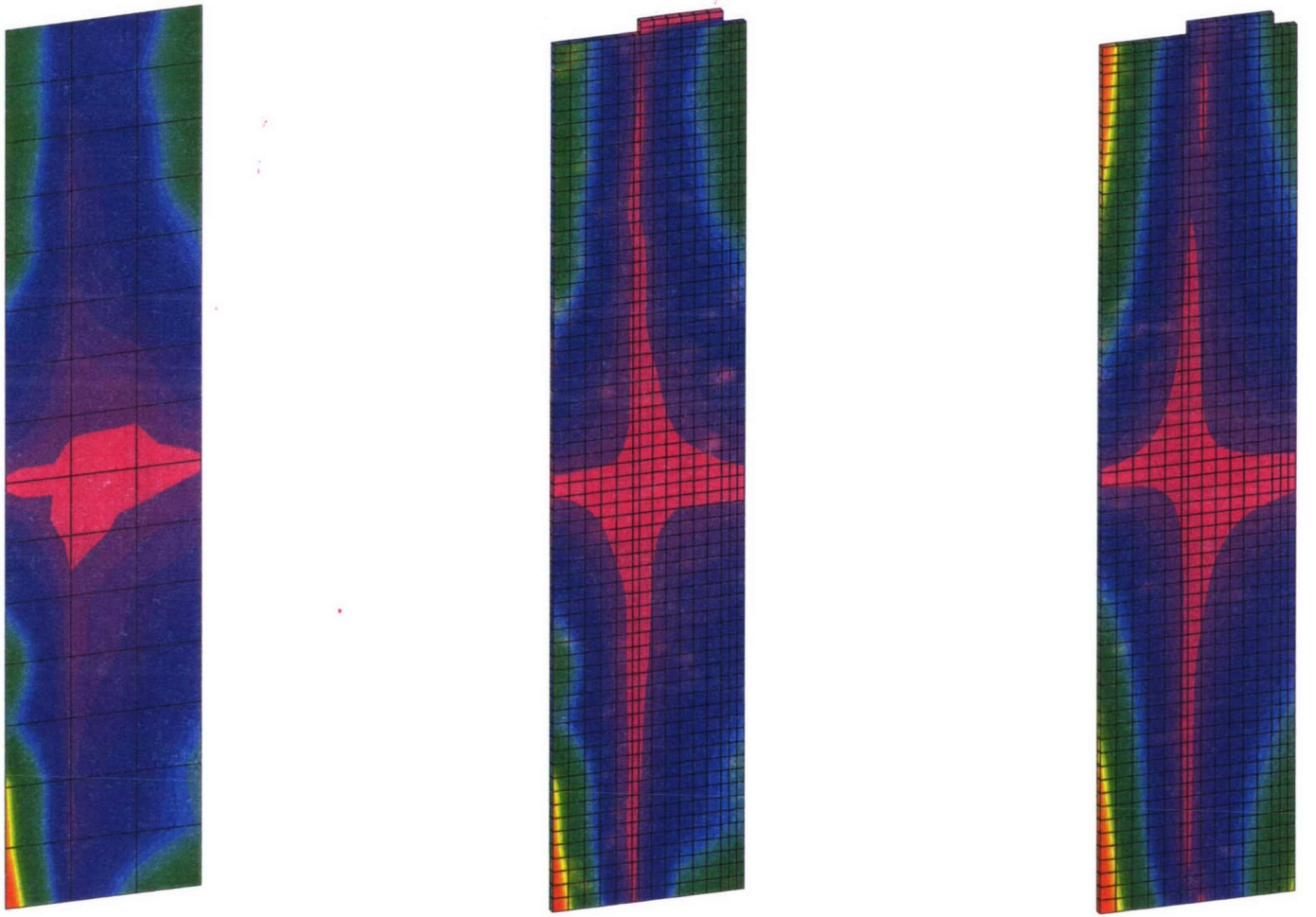

Figure 10. Experimental Data at 50 Hz Before and After it Has Been Interpolated Onto the Finite Element Mesh Compared to Numerical Mode Number 2

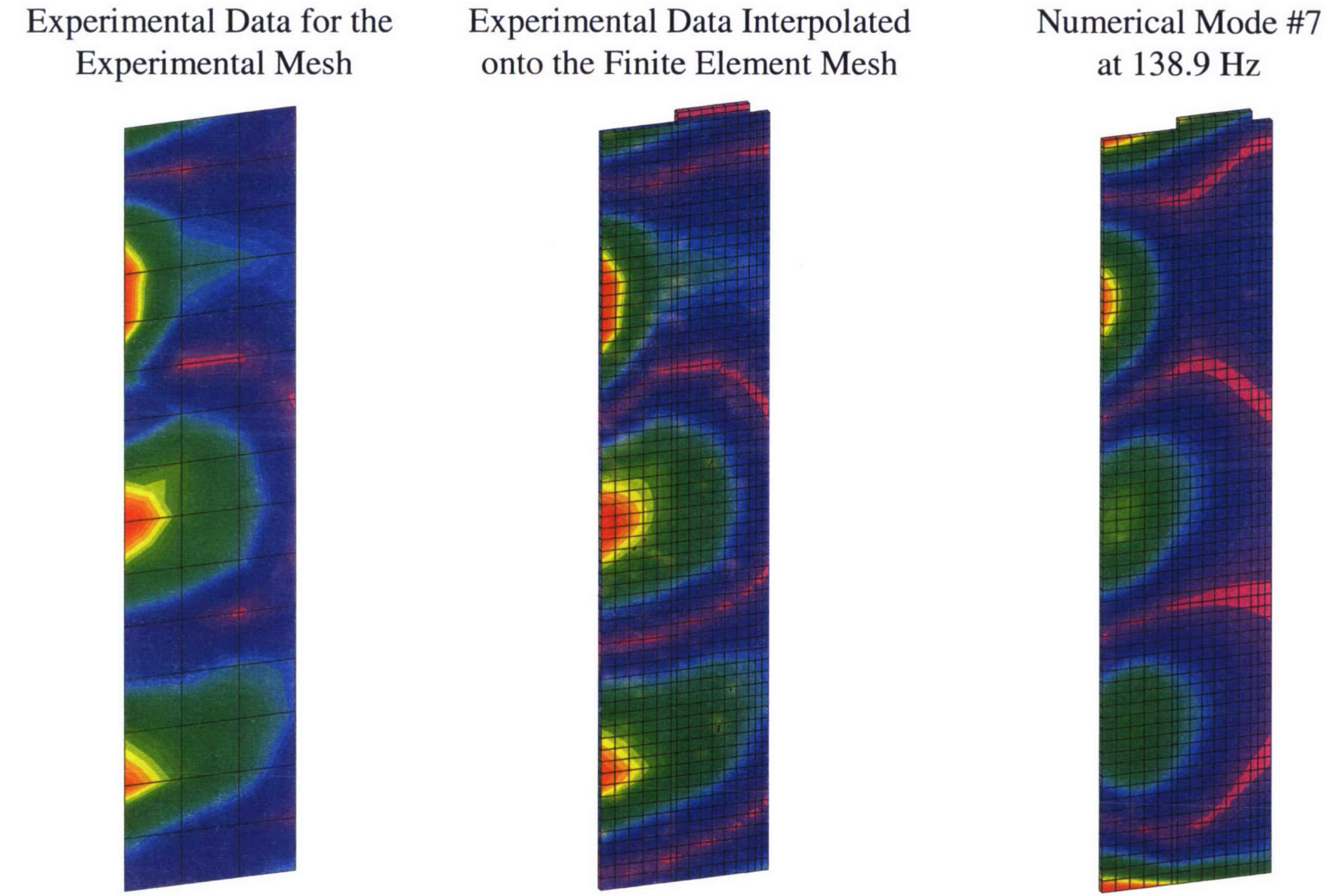

Figure 11. Experimental Data at 131.6 Hz Before and After It Has Been Interpolated Onto the Finite Element Mesh Compared to Numerical Mode Number 7

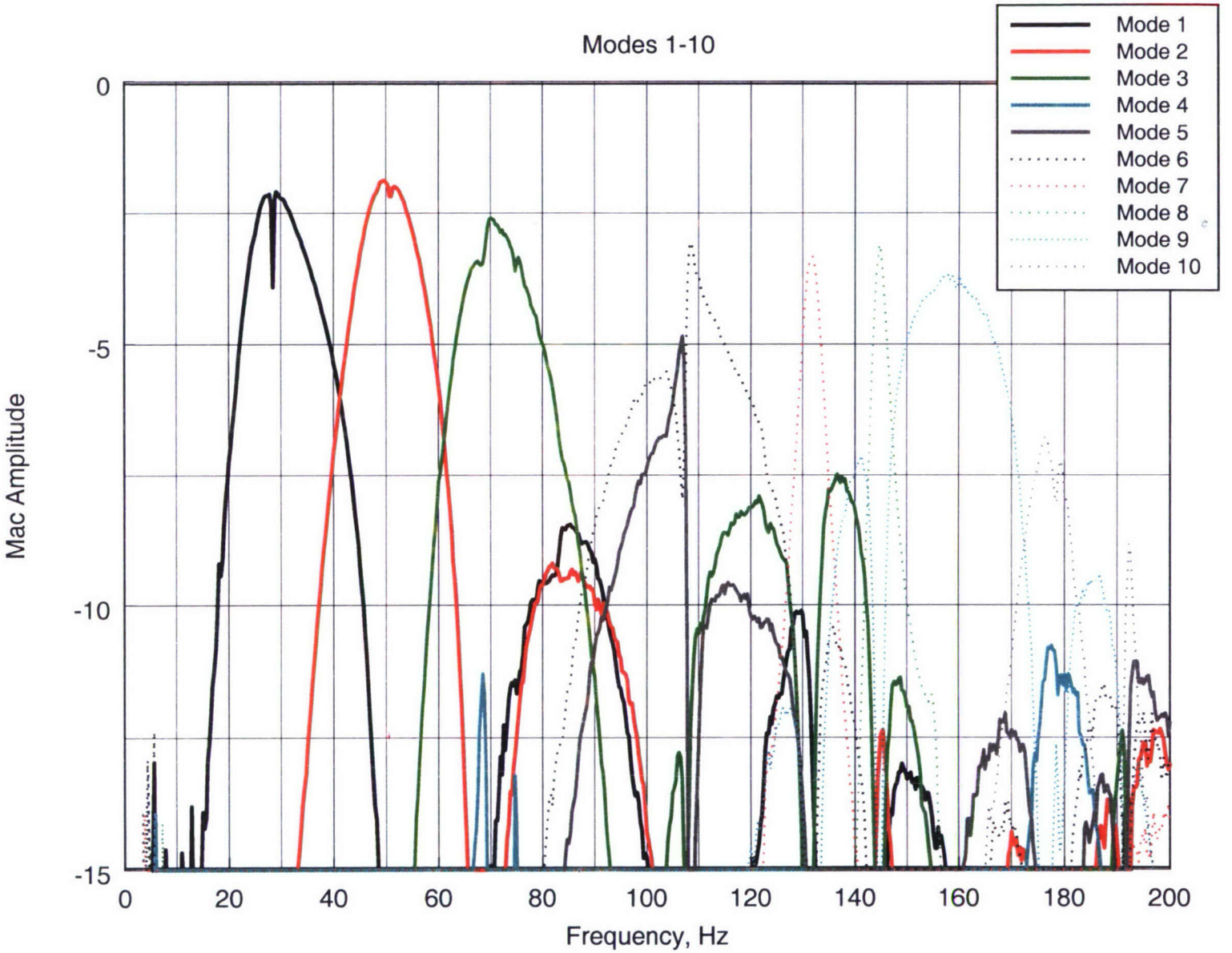

Figure 12. The Computed Modal Assurance Criteria for the First 10 Modes

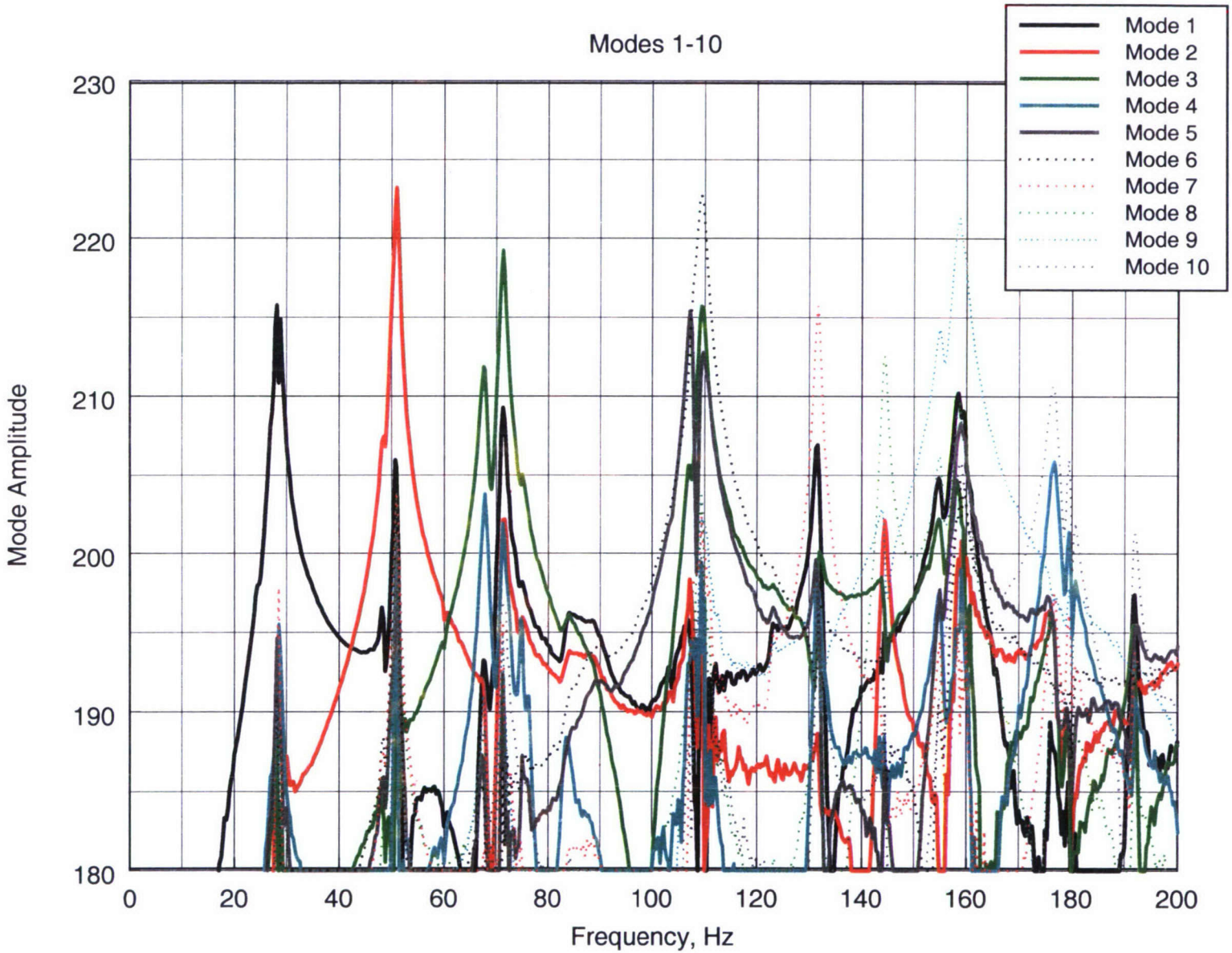

Figure 13. Experimental Data Broken Down Into the Contributions From the Numerical Modes

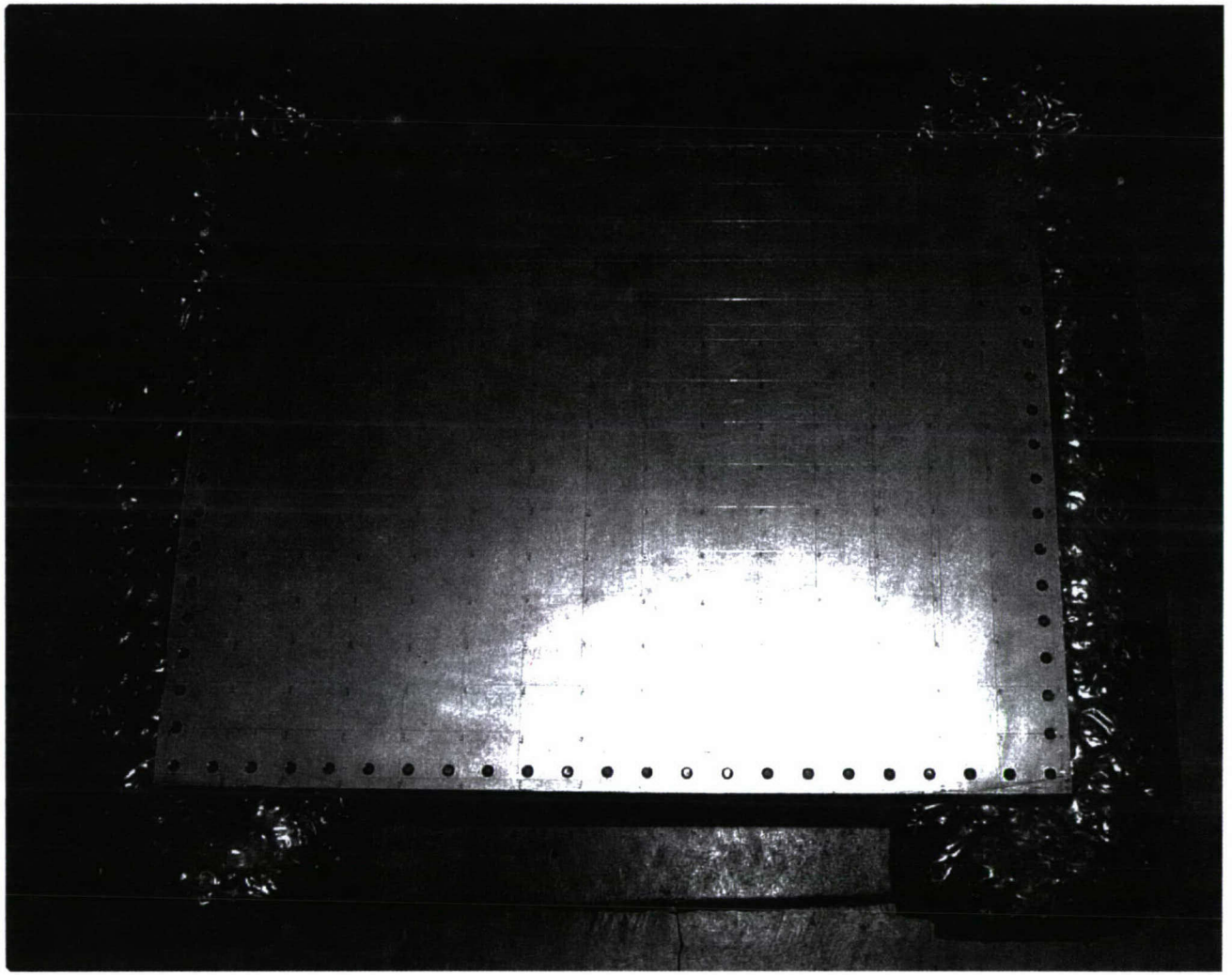

Figure 14. Shelf 1 Sitting On "Bubble Wrap"

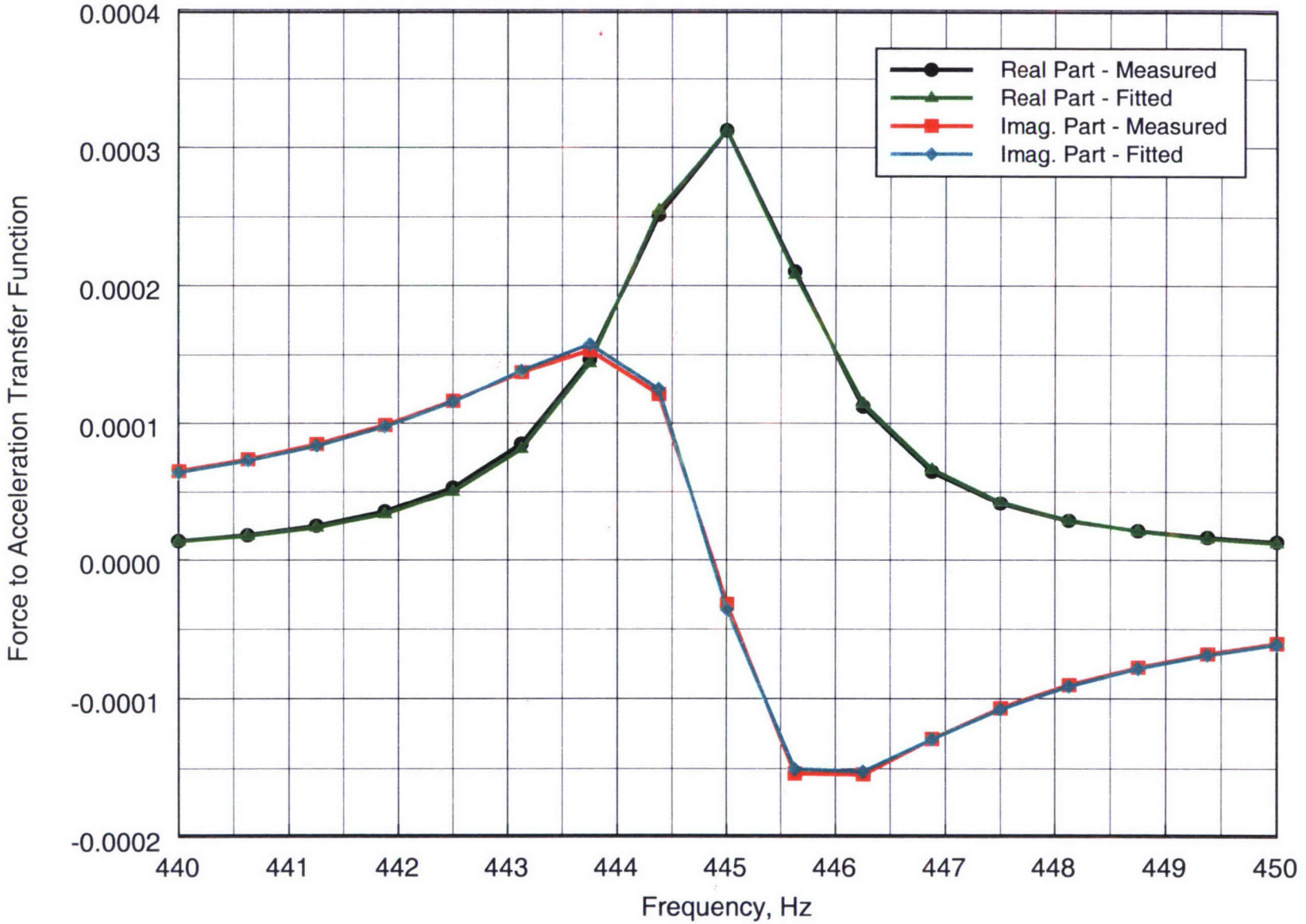

Figure 15. Comparison of the Measured and Fitted Transfer Function Data for a Single Mode

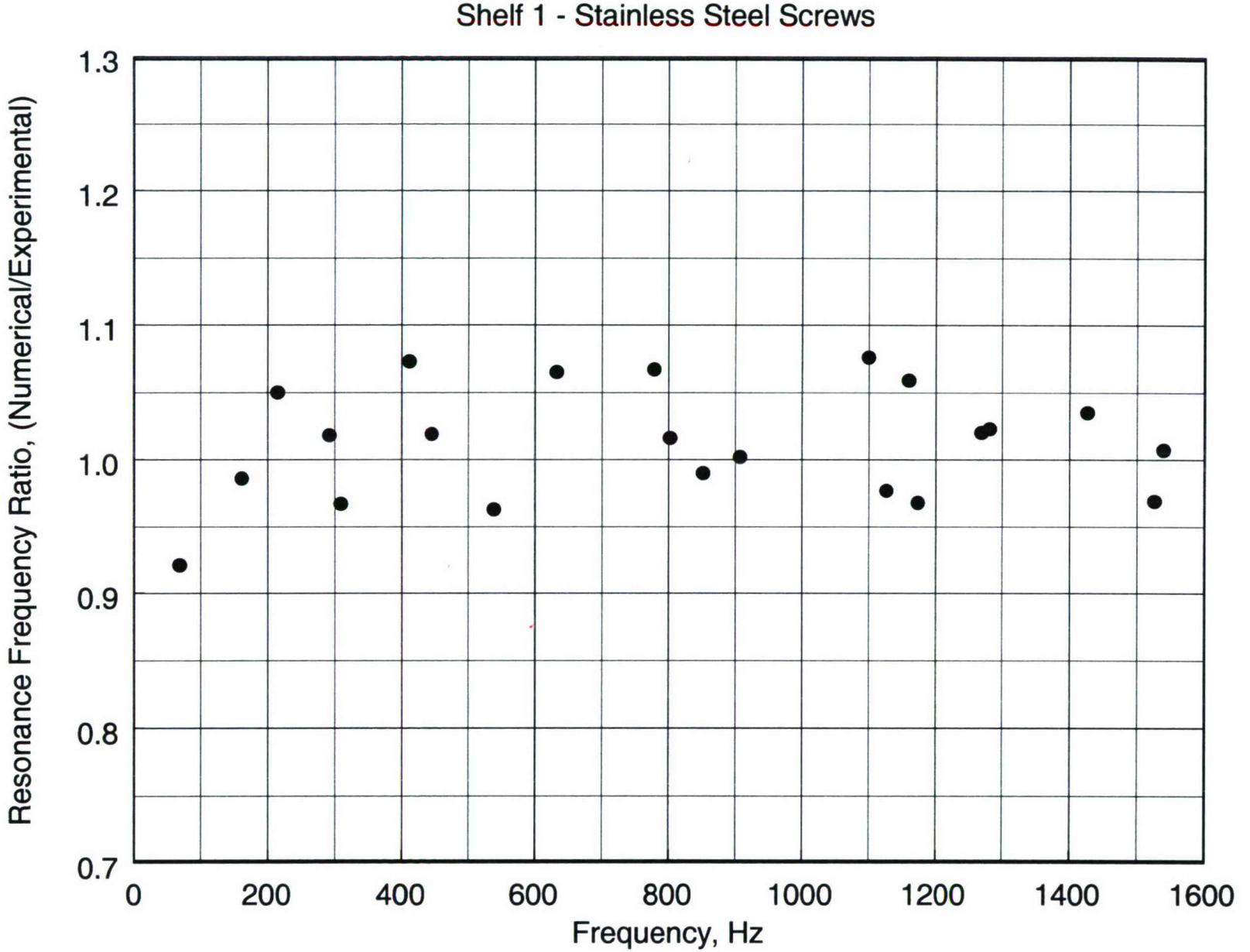

Figure 16. Resonance Frequency Ratios for Prototype Shelf 1

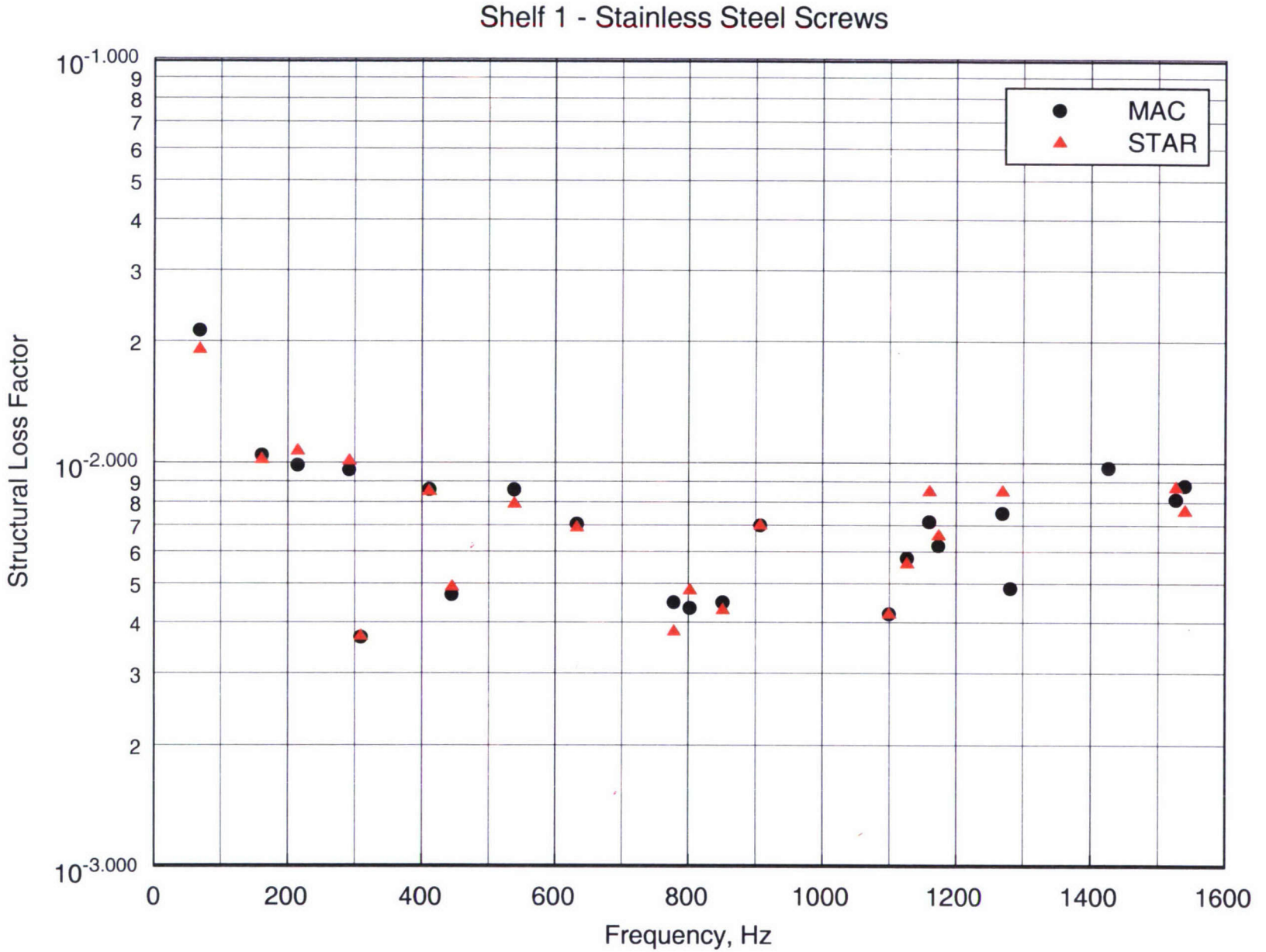

Figure 17. Comparison Between the Predicted Loss Factors for Prototype Shelf 1

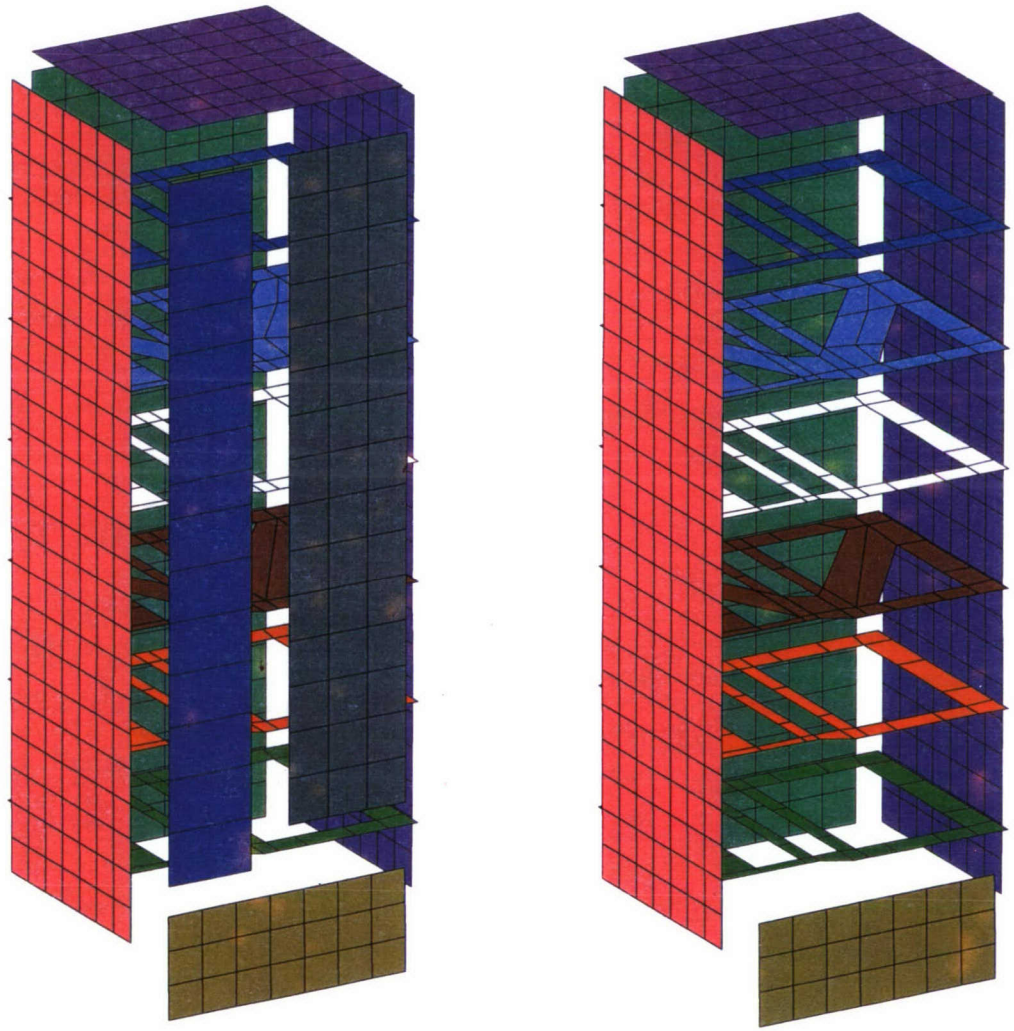

Figure 18. Experimental Mesh With and Without the Front Doors

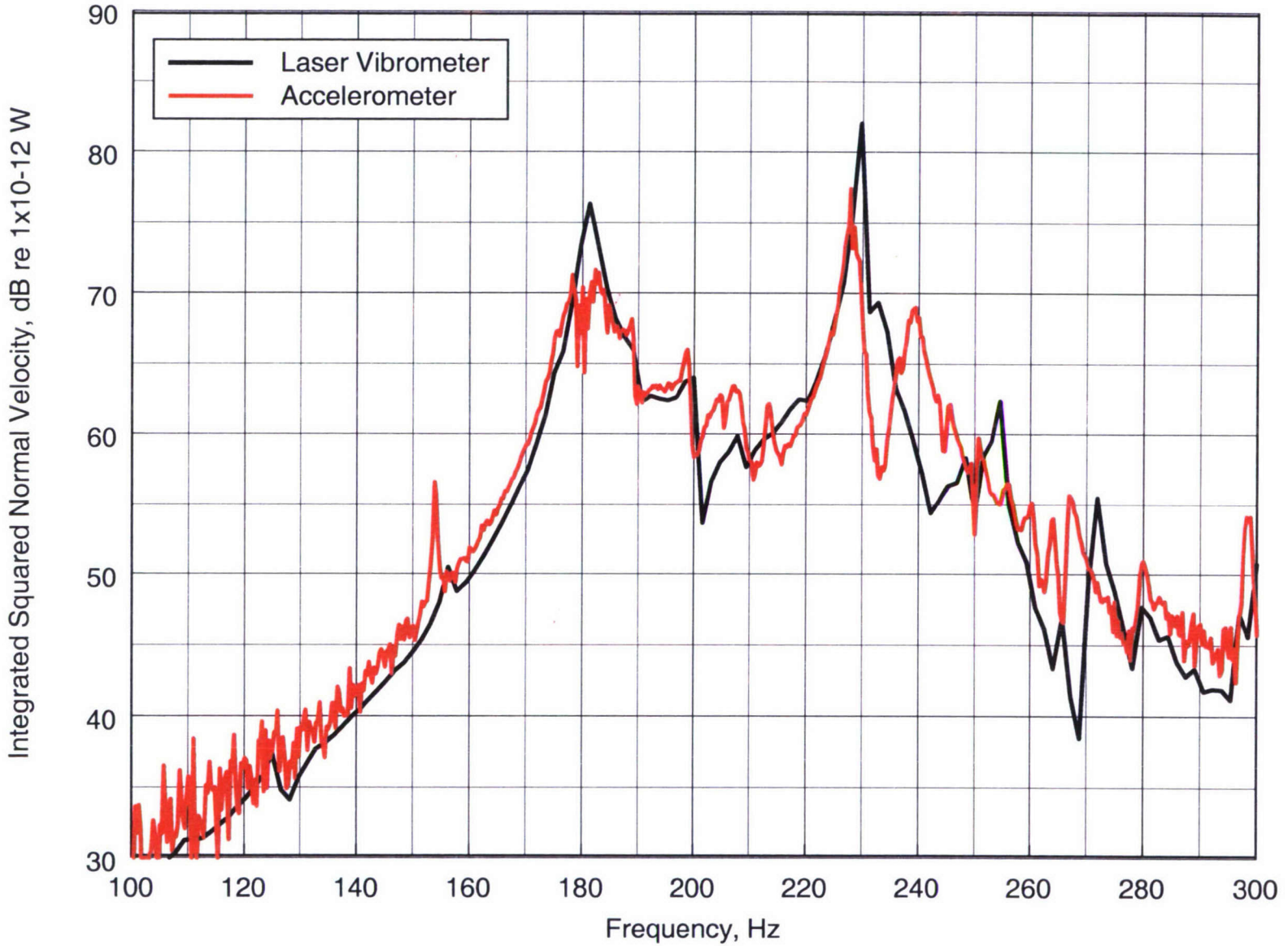

Figure 19. Comparison Between the Vibrations of Right Side of the Cabinet Near the Second Shelf

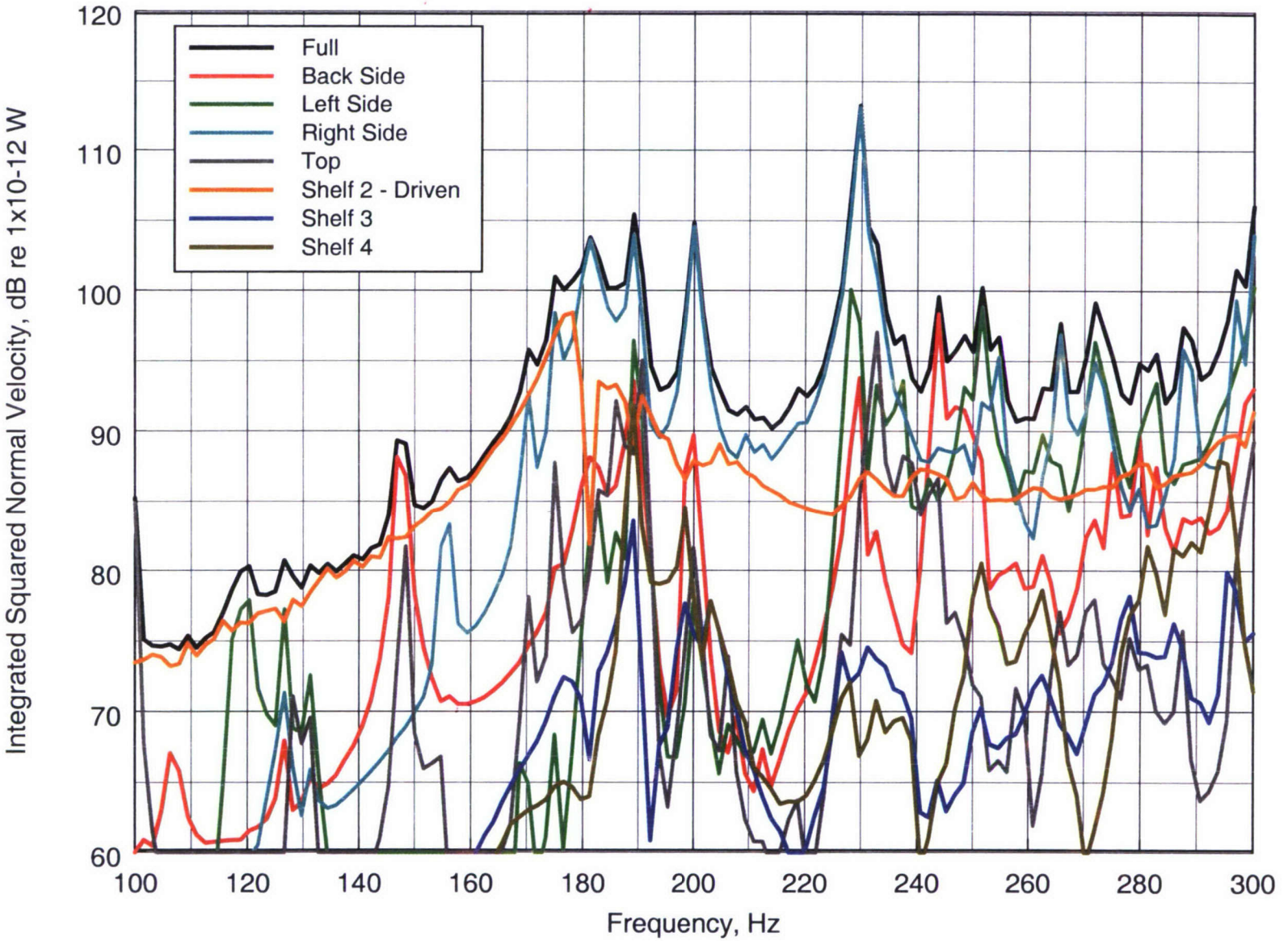

Figure 20. Breakdown Down of the Normal Surface Velocity for the Experimental Measurements

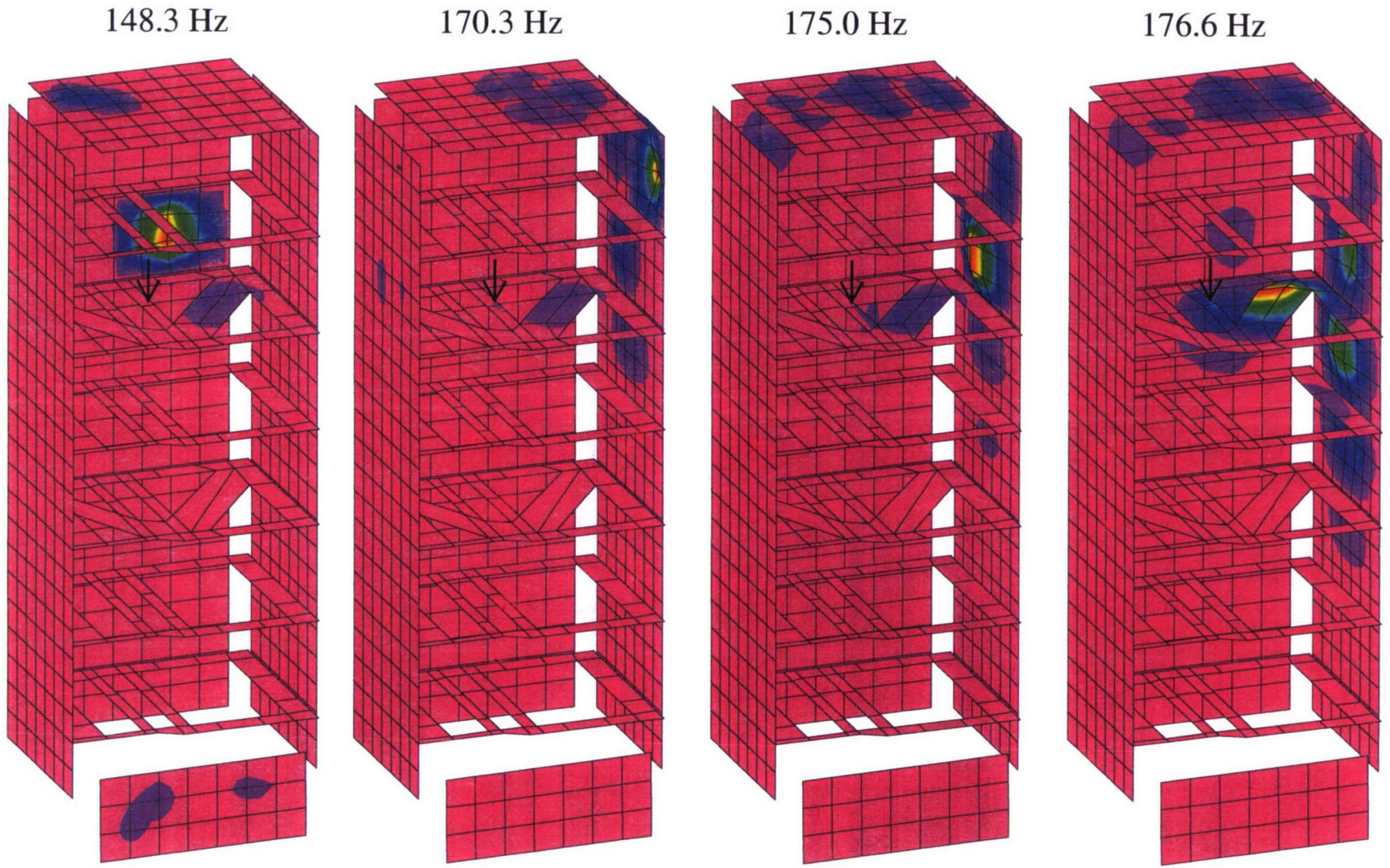

Figure 21. First Set of Four Operating Deflection Shapes at the Resonance Peaks for the Experimental Data

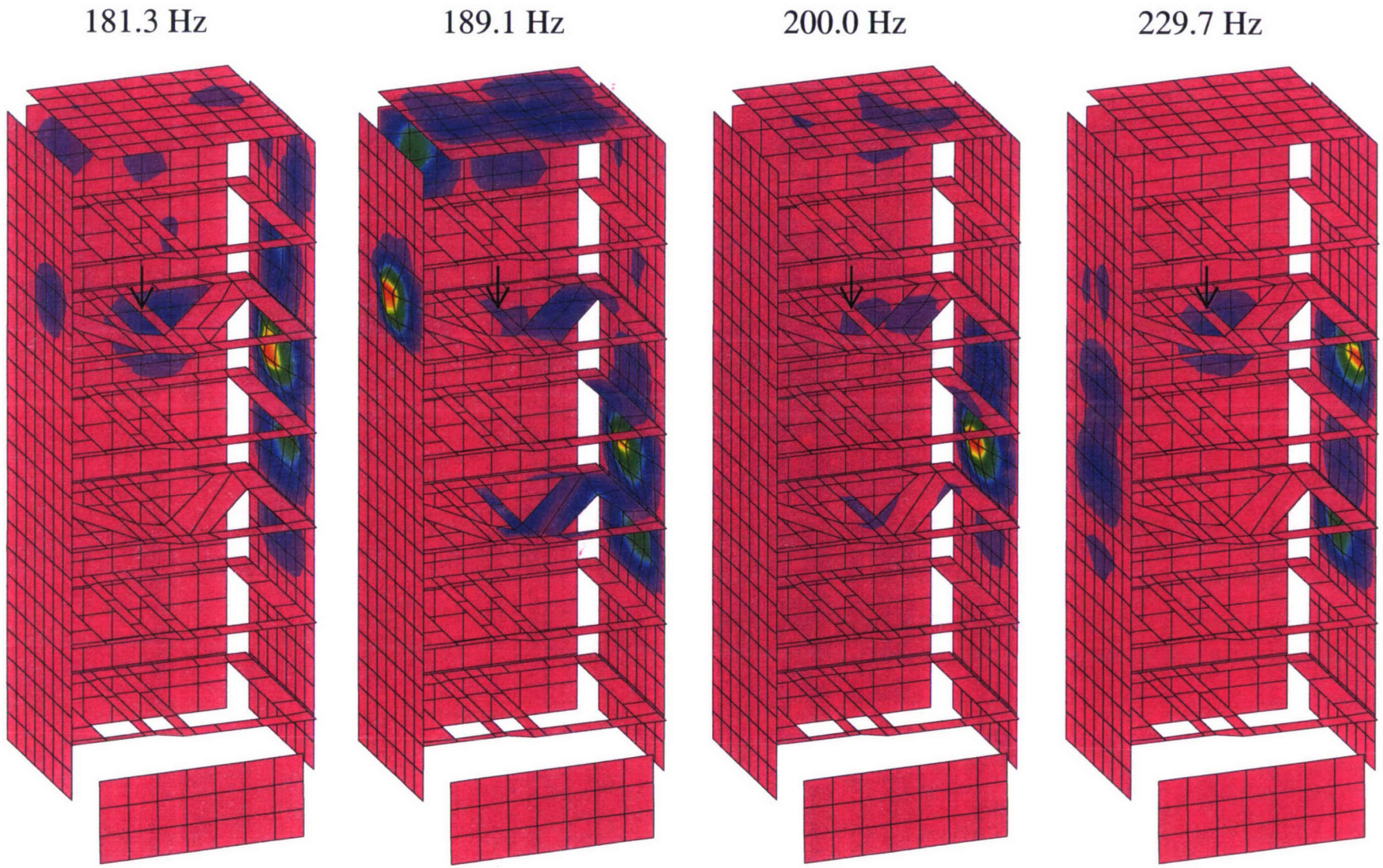

Figure 22. Second Set of Four Operating Deflection Shapes at the Resonance Peaks for the Experimental Data

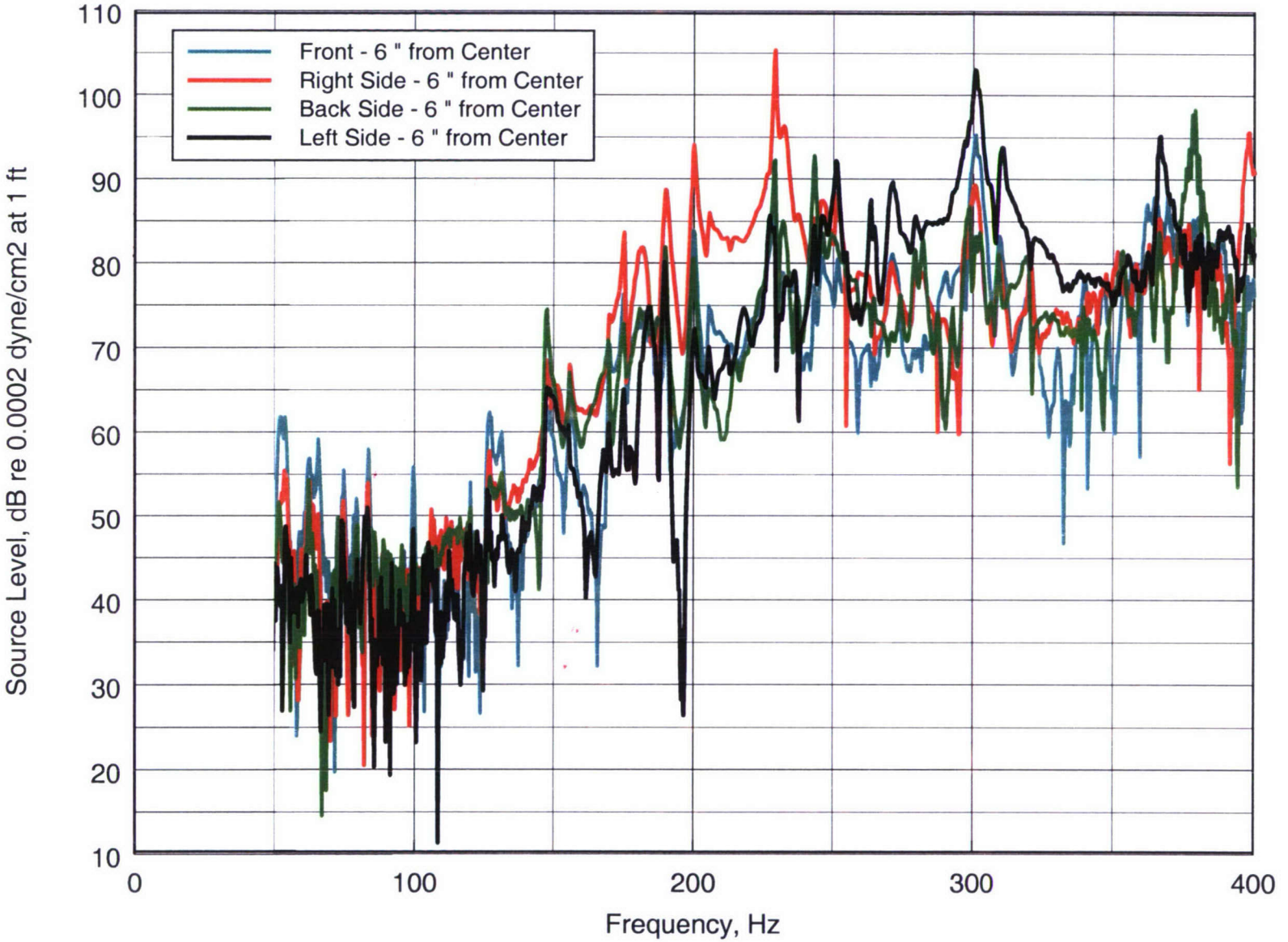

Figure 23. Measured Acoustic Pressure Levels Near the Surface of the Enclosure

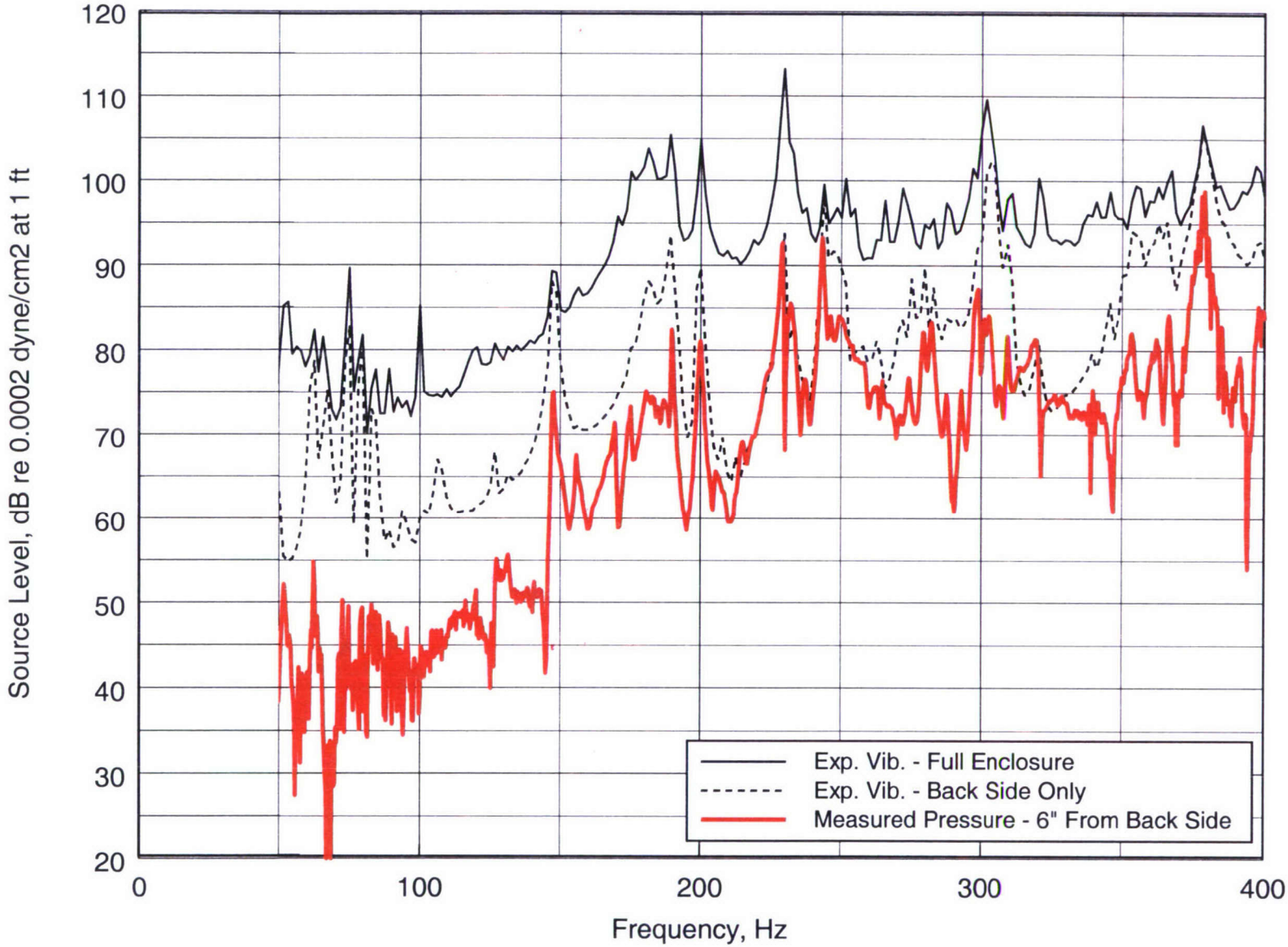

Figure 24. Comparison Between Measured Pressure and Vibration Levels Near the Back Side of the Enclosure

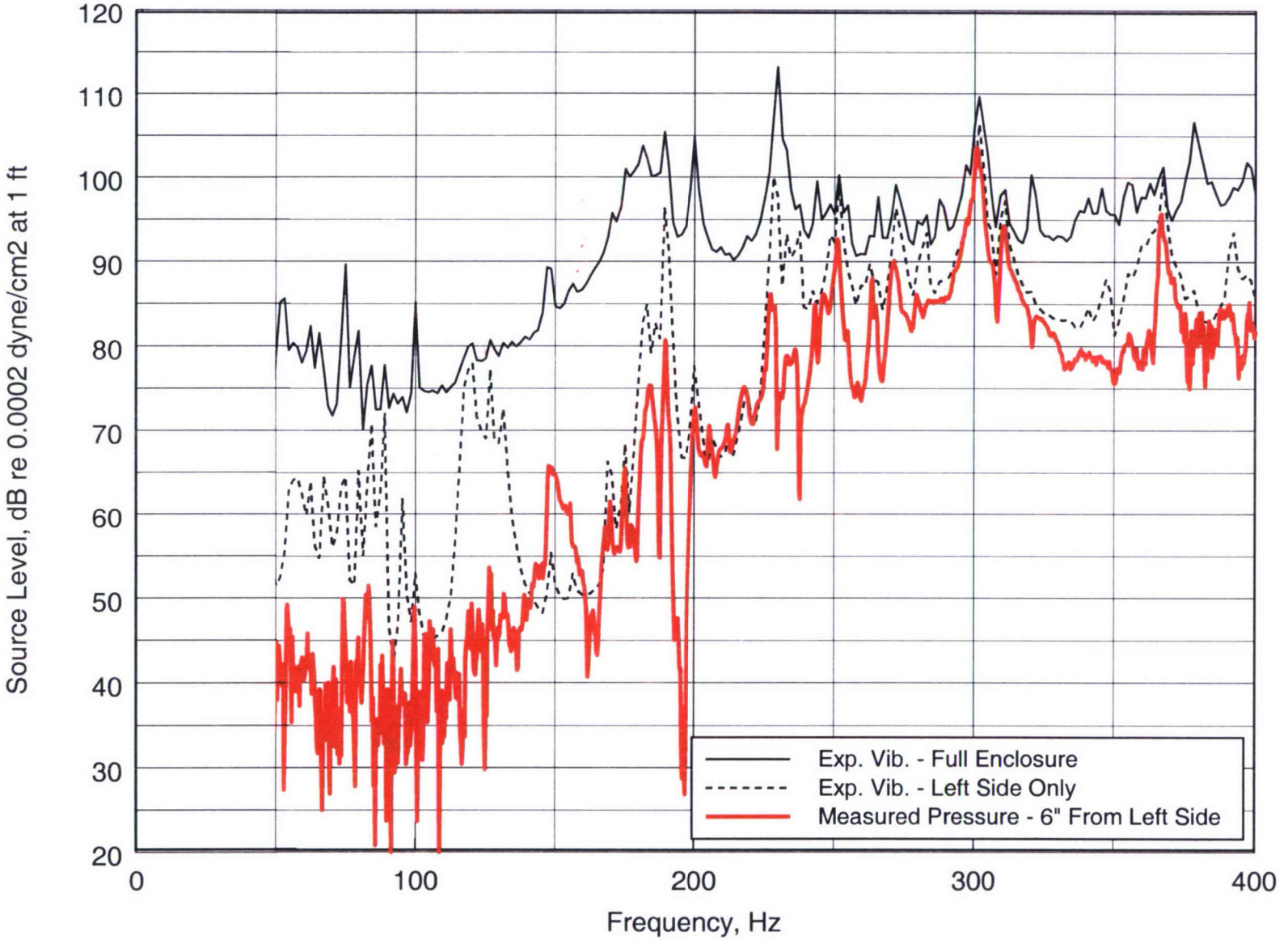

Figure 25. Comparison Between Measured Pressure and Vibration Levels Near the Left Side of the Enclosure

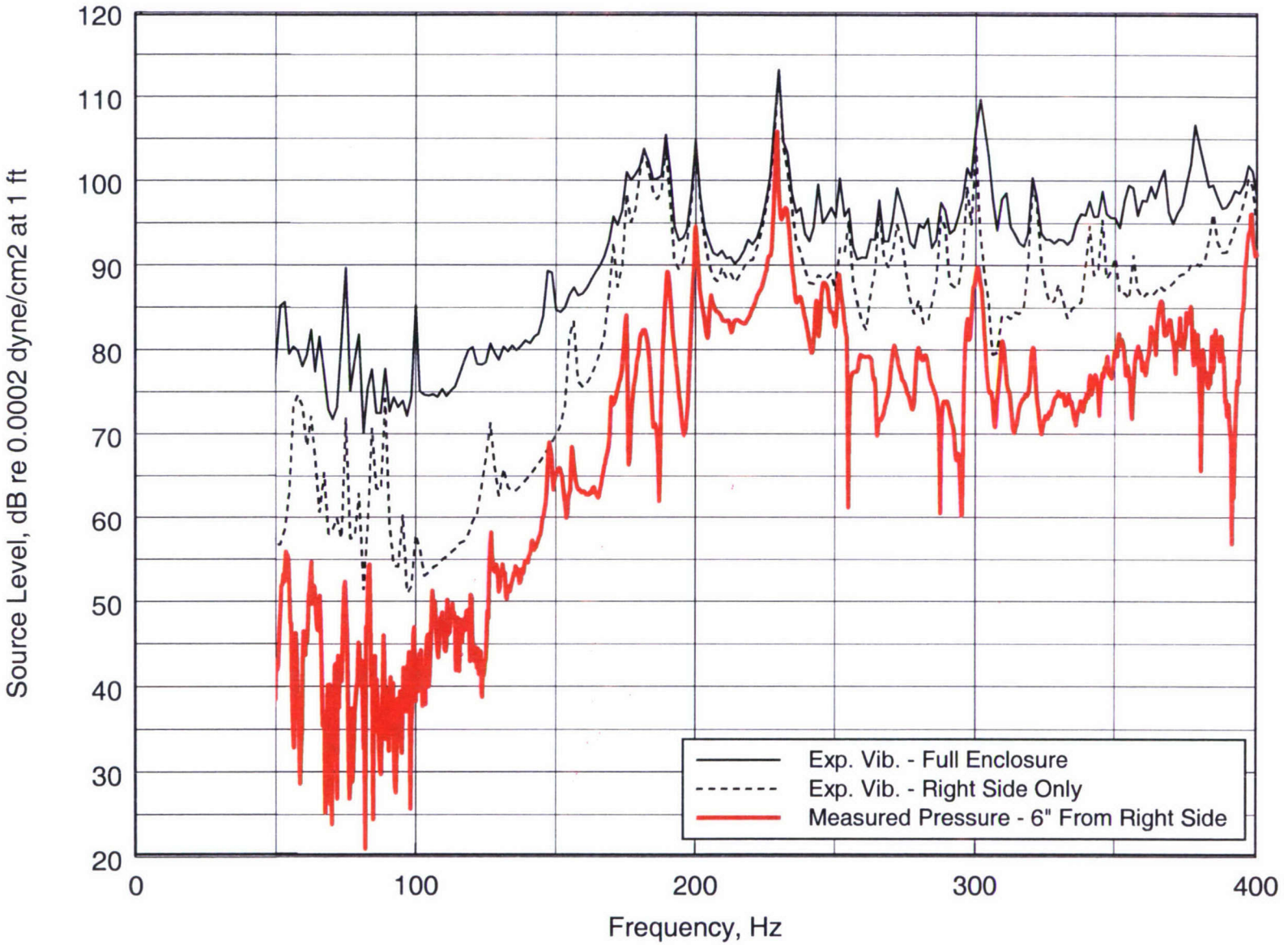

Figure 26. Comparison Between Measured Pressure and Vibration Levels Near the Right Side of the Enclosure

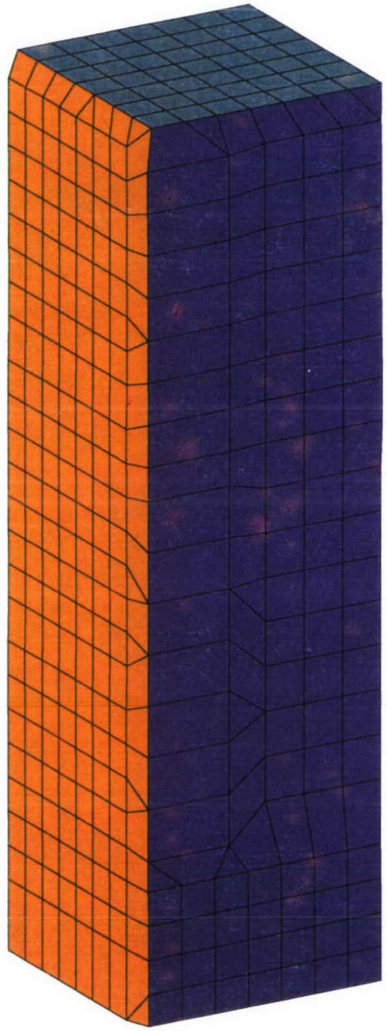

Figure 27. Boundary Element Representation of the Outer Skin of the Enclosure for the Experimental Mesh

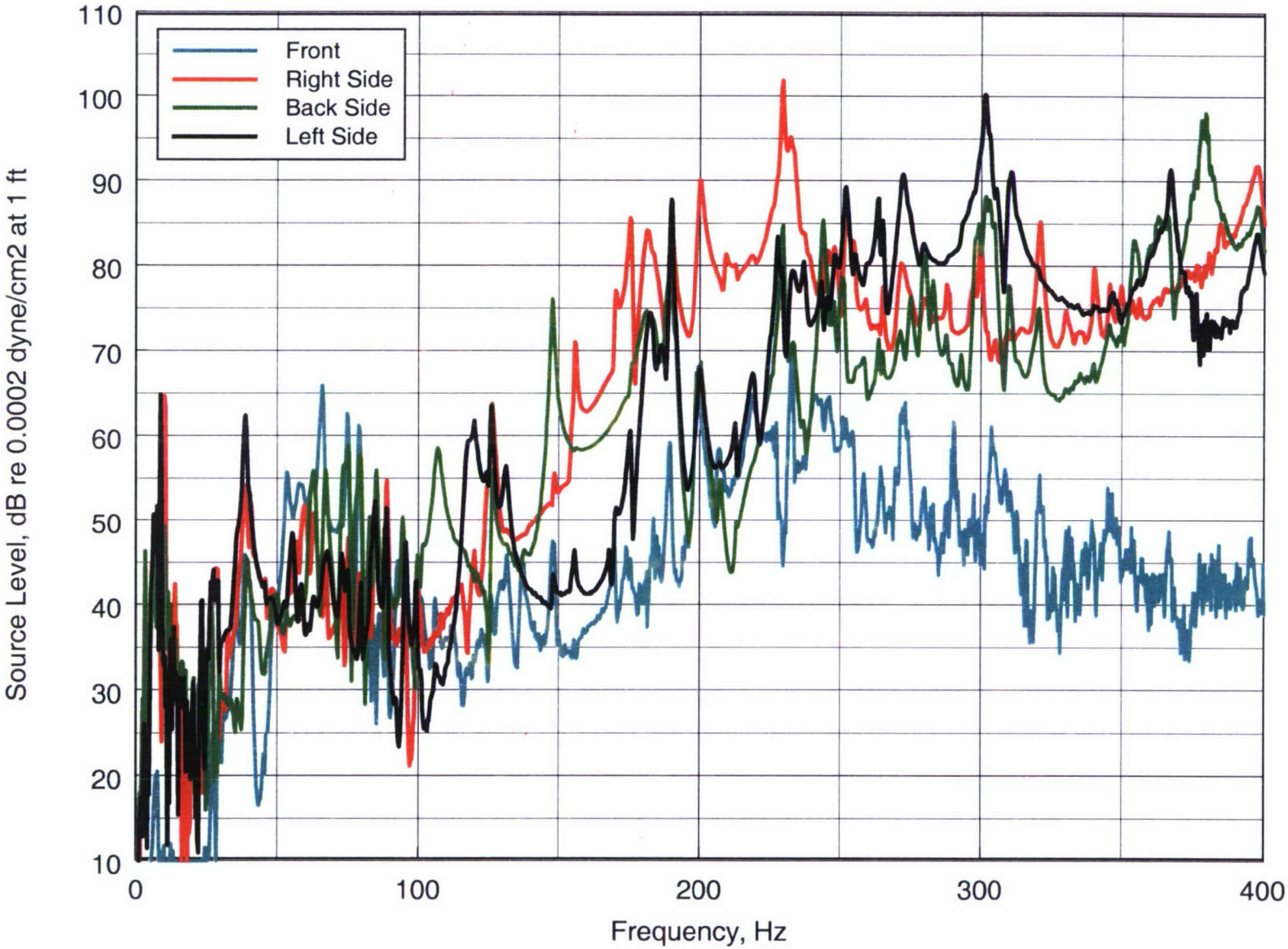

Figure 28. Predicted Acoustic Pressure Levels Near the Surface of the Enclosure Using the Vibration Data as Input

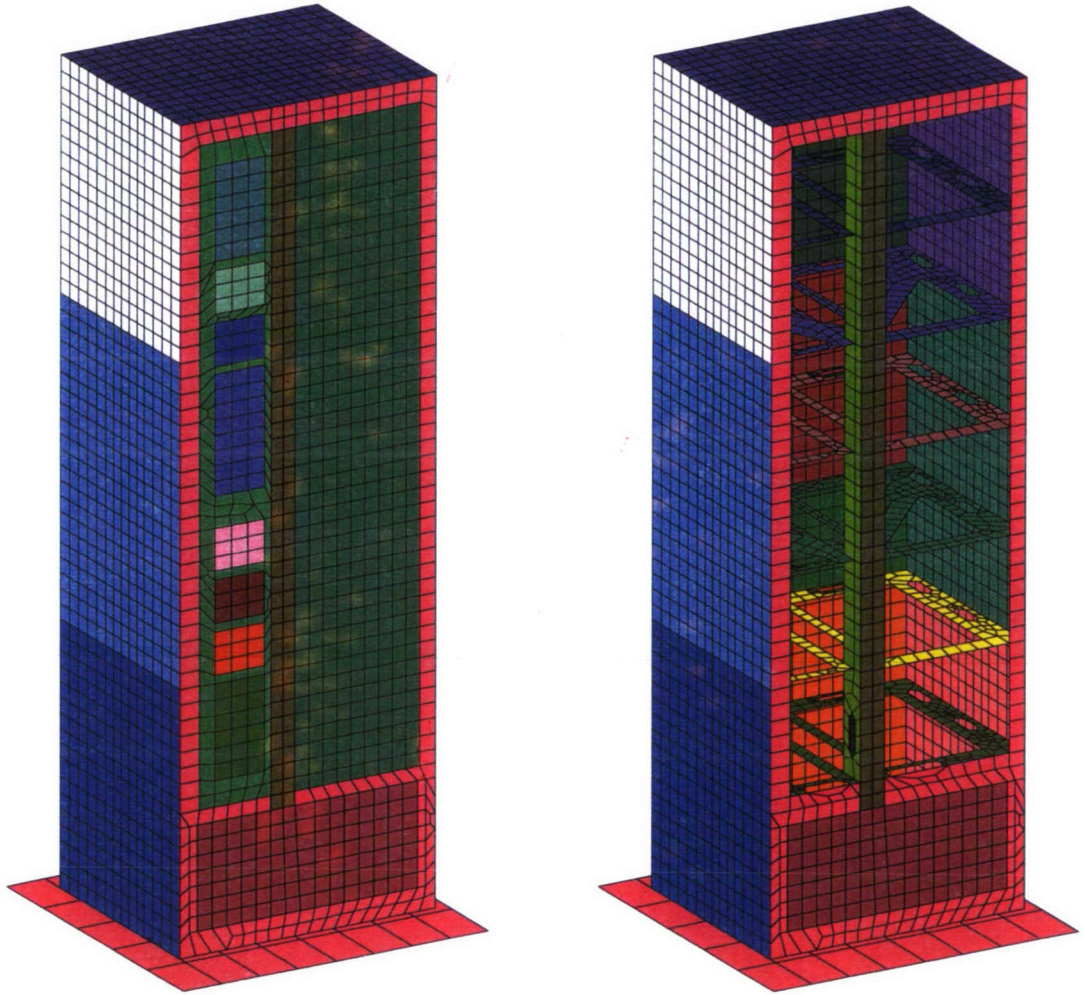

Figure 29. Original Finite Element Mesh With and Without the Front Doors

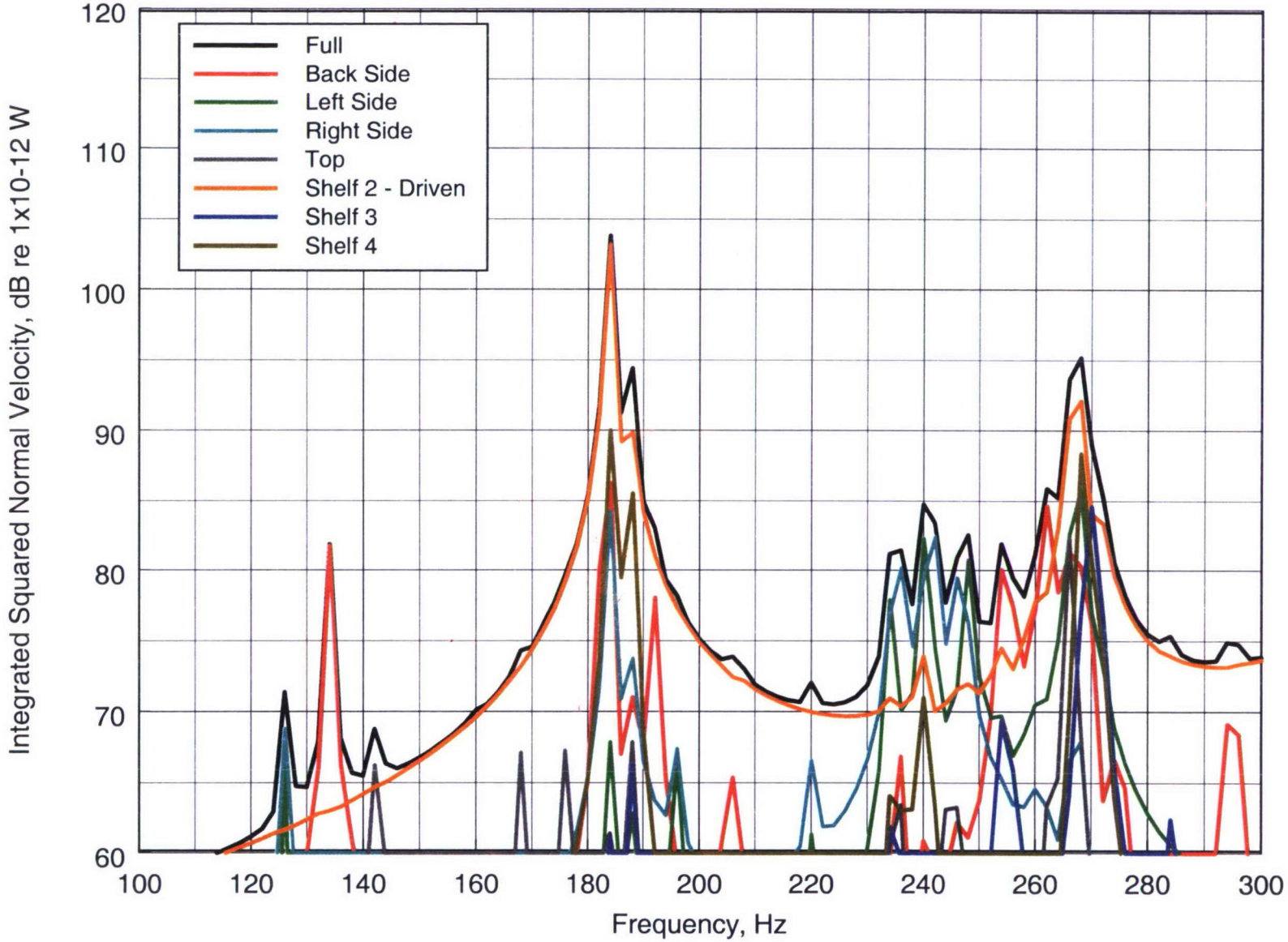

Figure 30. Breakdown of the Normal Surface Velocity for the Original Finite Element Model

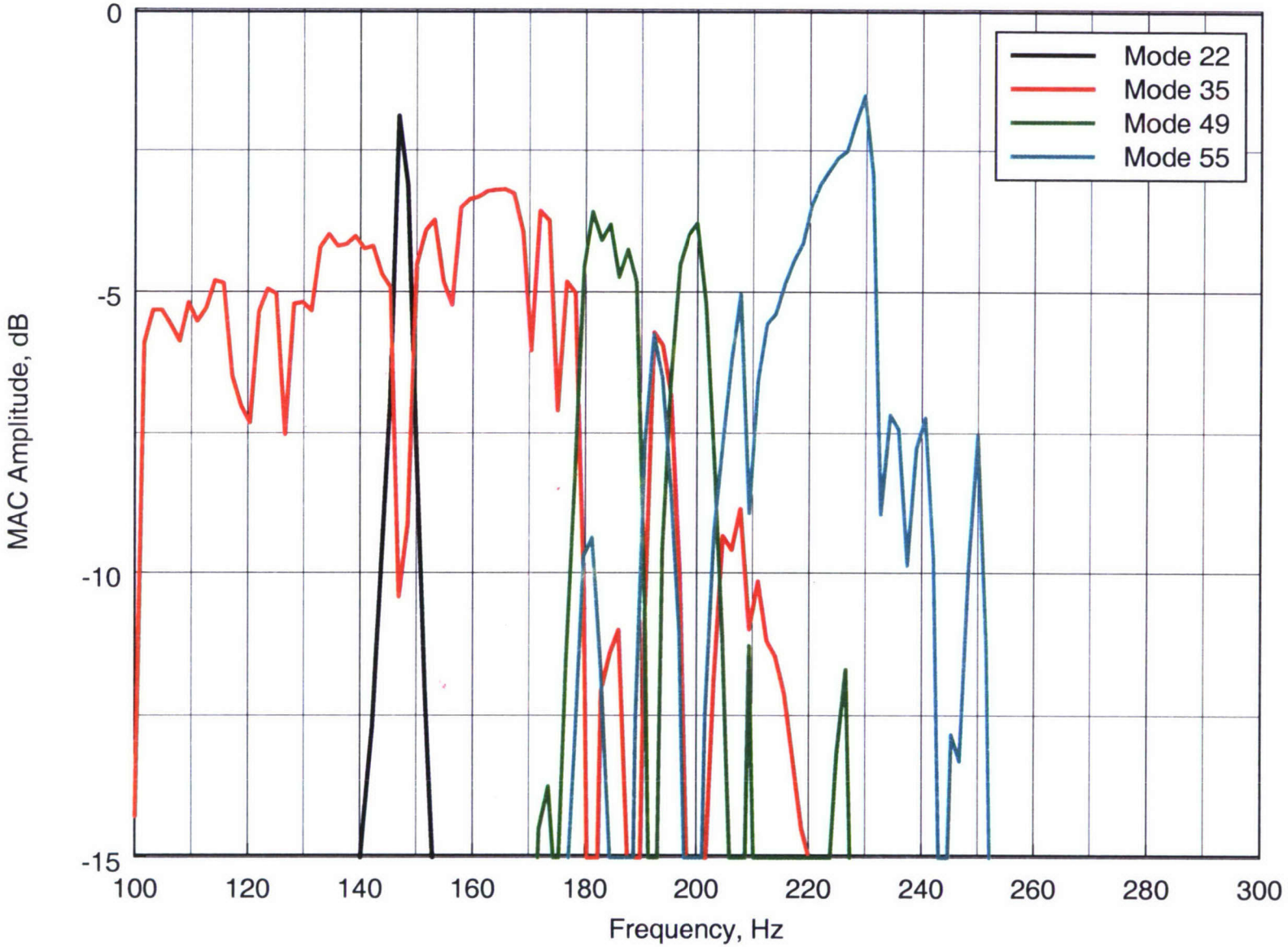

Figure 31. Dominant MAC Amplitudes for the Original Finite Element Model

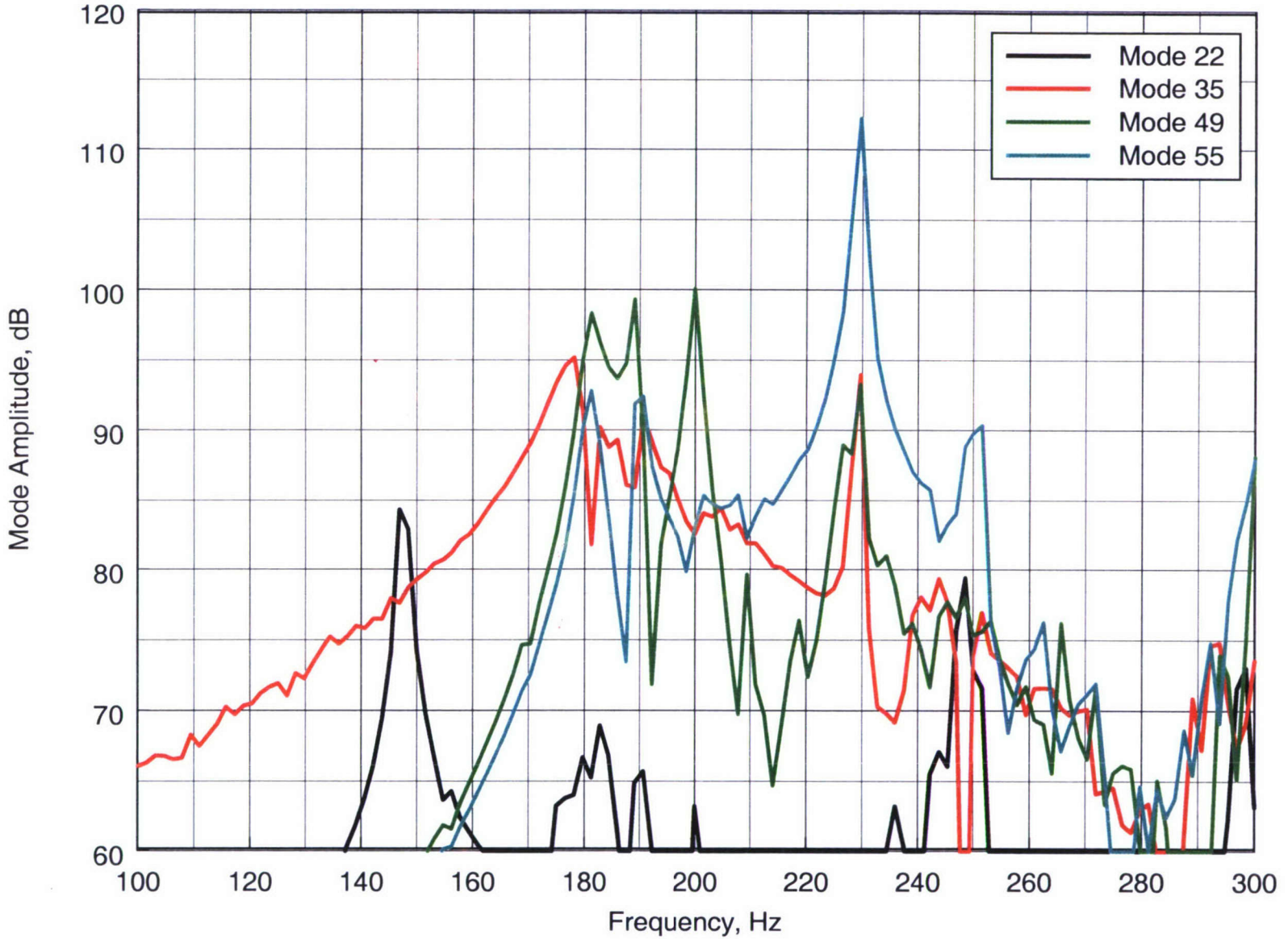

Figure 32. Dominant Mode Amplitudes for the Original Finite Element Model

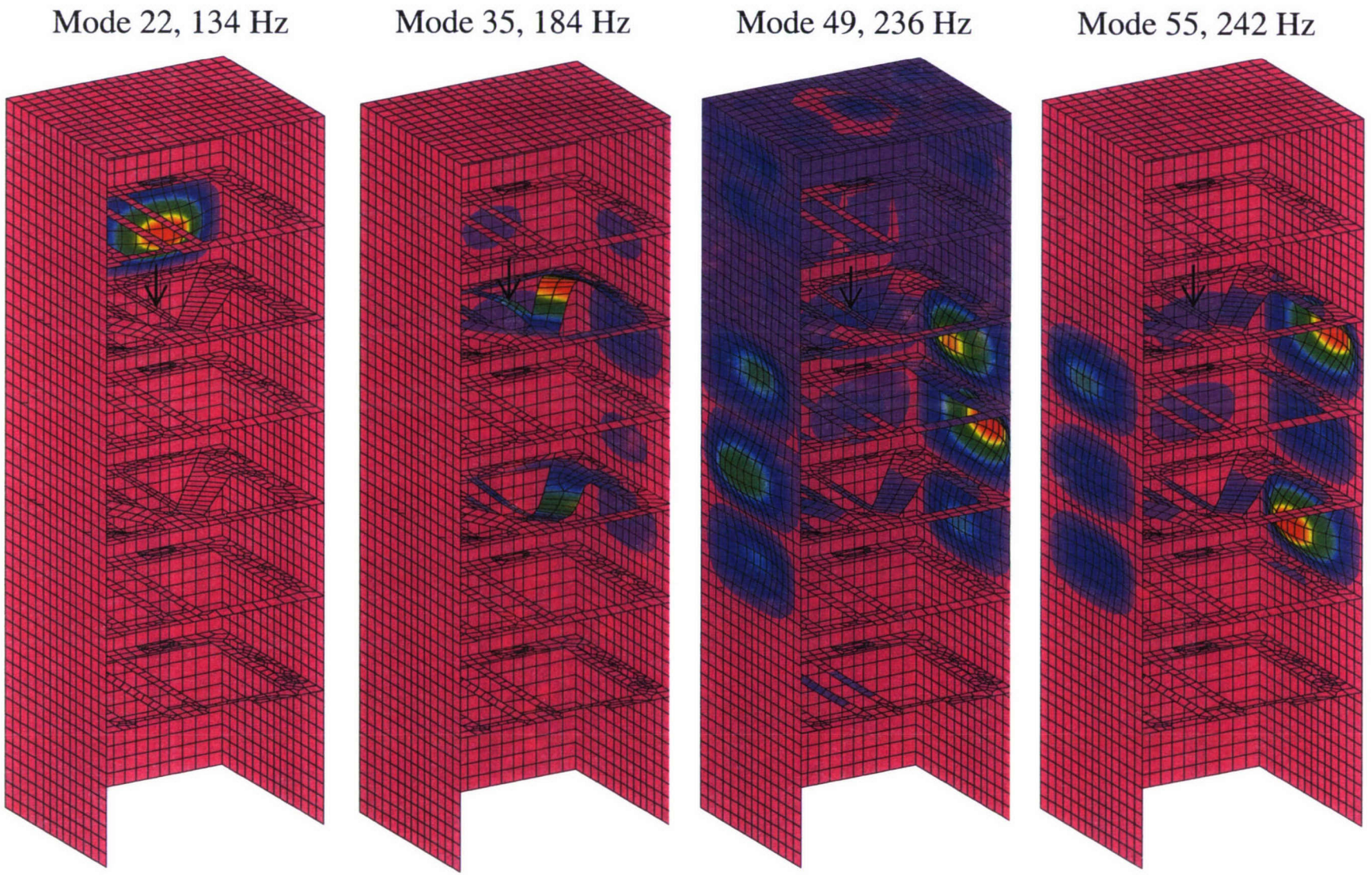

Figure 33. Mode Shapes and Resonance Frequencies for the Dominant Modes for the Original Finite Element Model

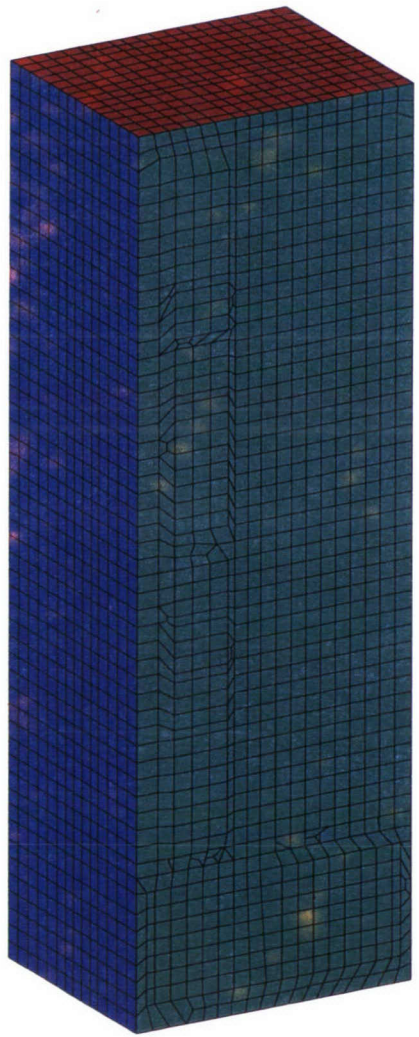

Figure 34. Boundary Element Representation of the Outer Enclosure Skin for the Original Finite Element Mesh

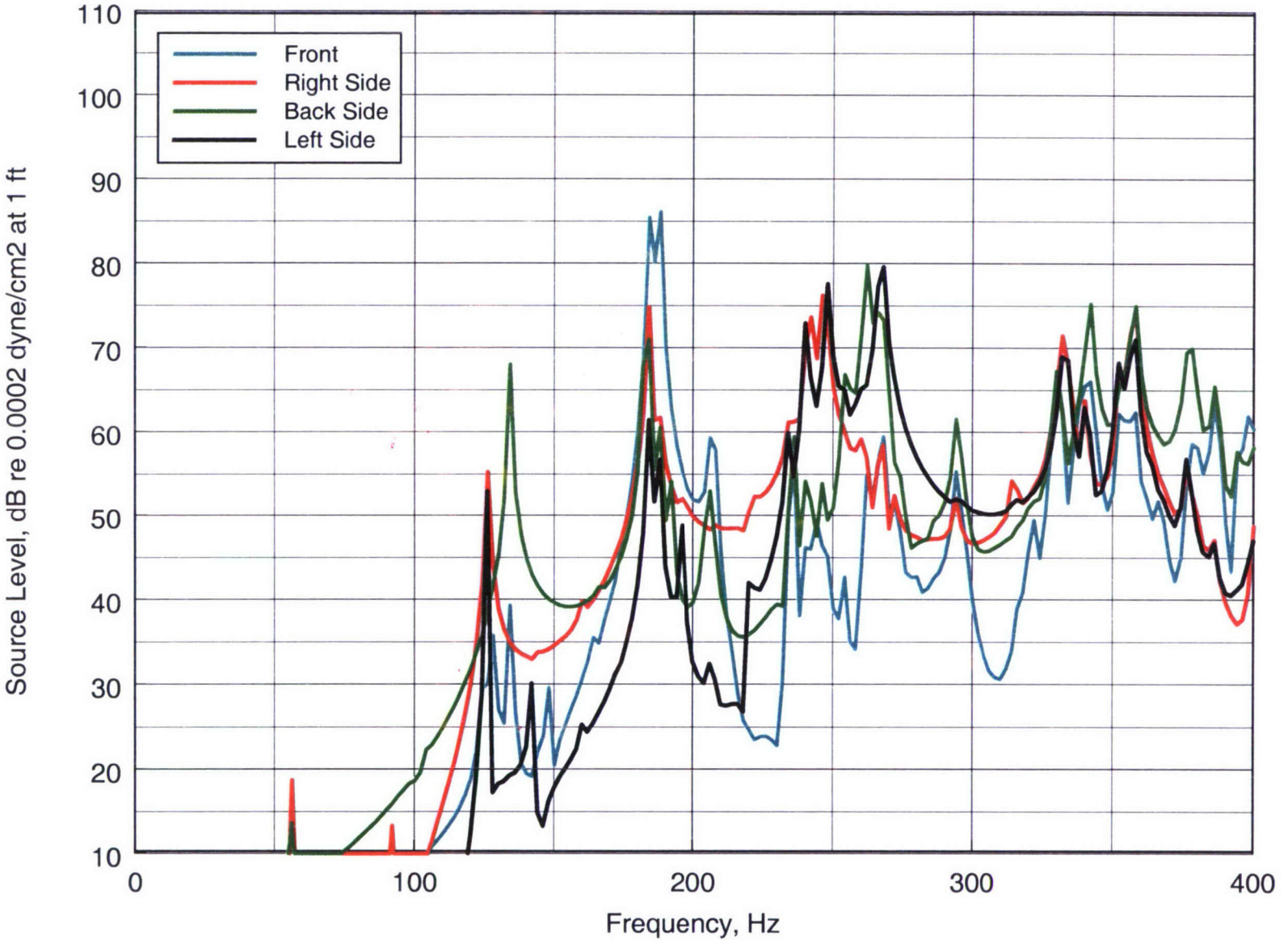

Figure 35. Predicted Acoustic Pressure Levels Near the Enclosure Surface for the Original Finite Element Model

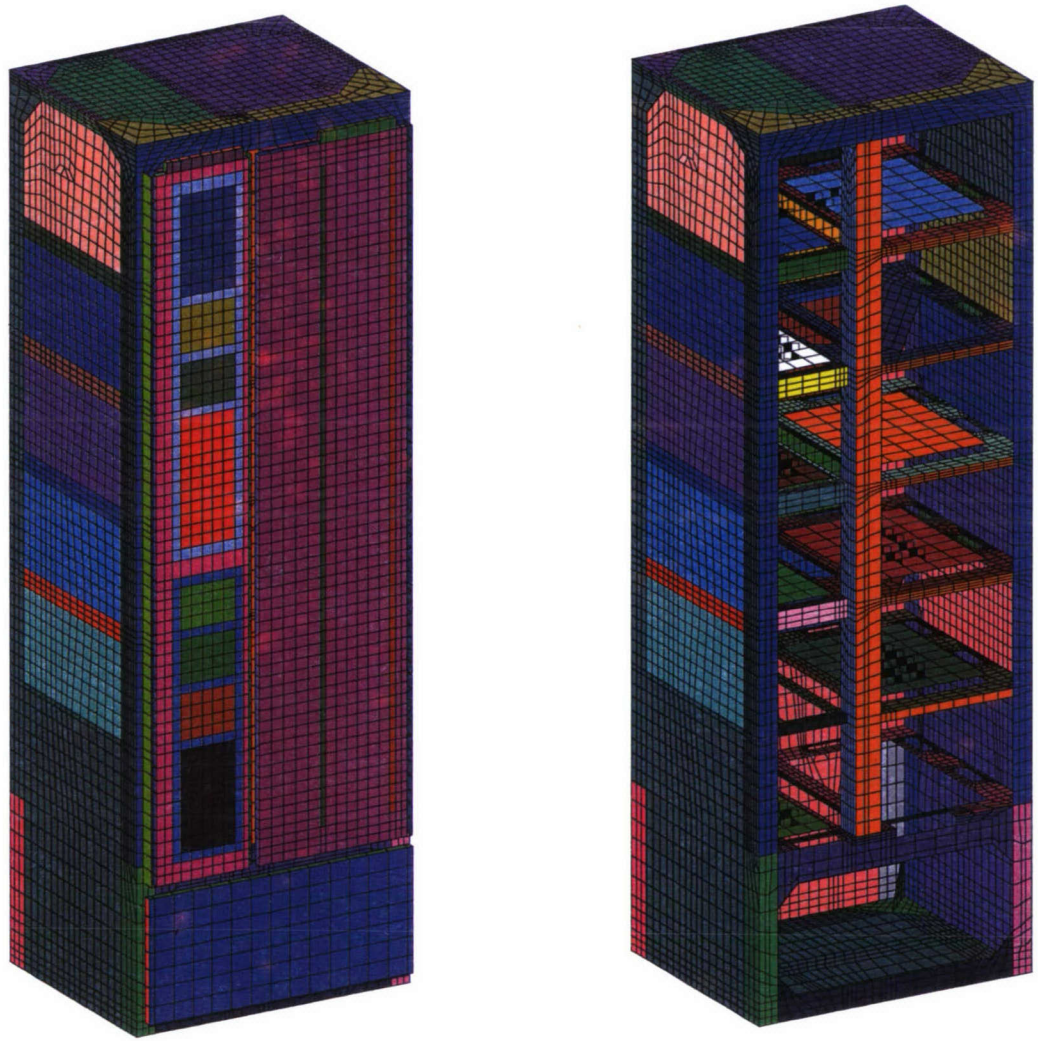

Figure 36. Revised Finite Element Mesh With and Without the Front Doors

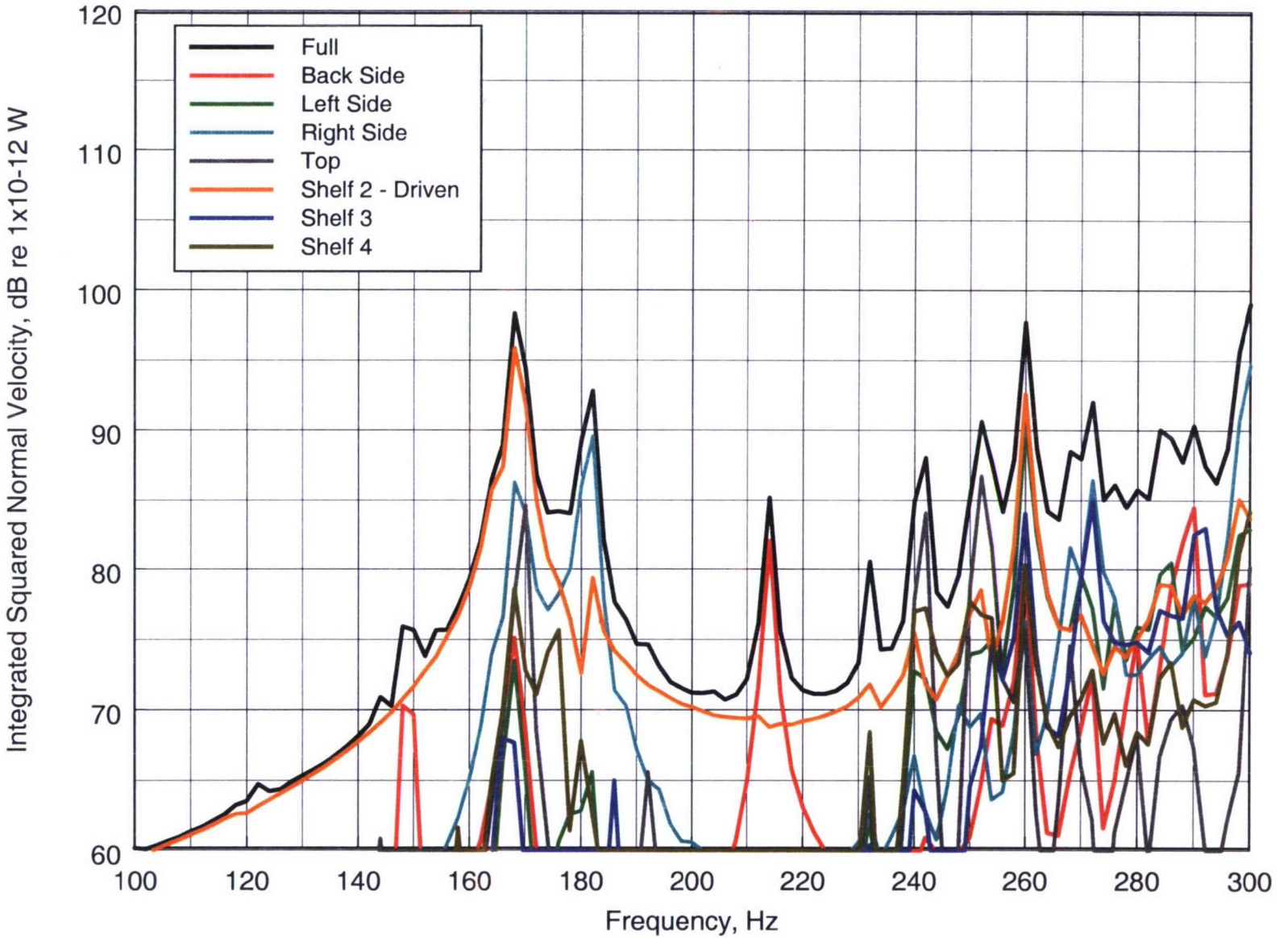

Figure 37. Breakdown of the Normal Surface Velocity for the Revised Finite Element Model

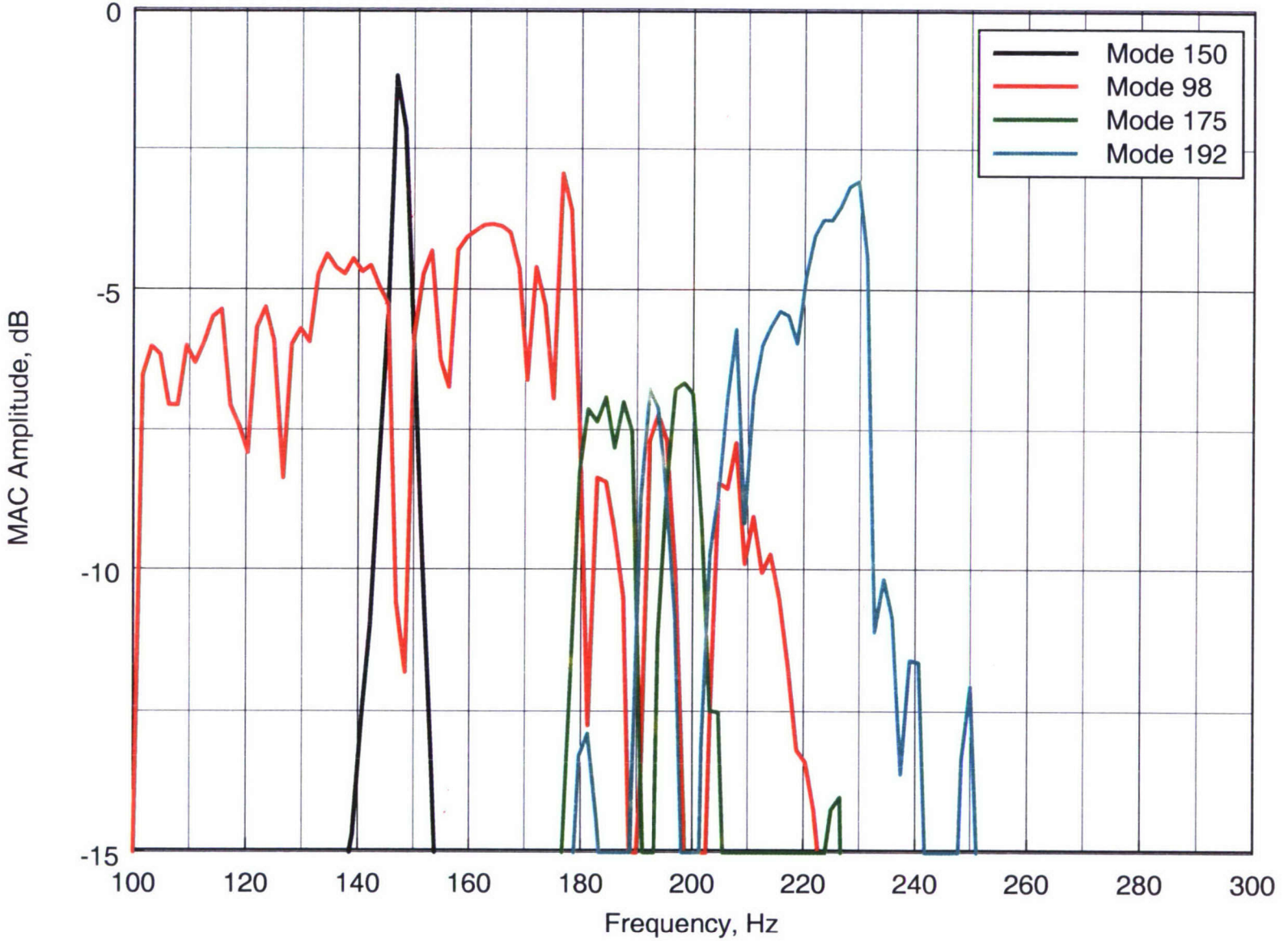

Figure 38. Dominant MAC Amplitudes for the Revised Finite Element Model

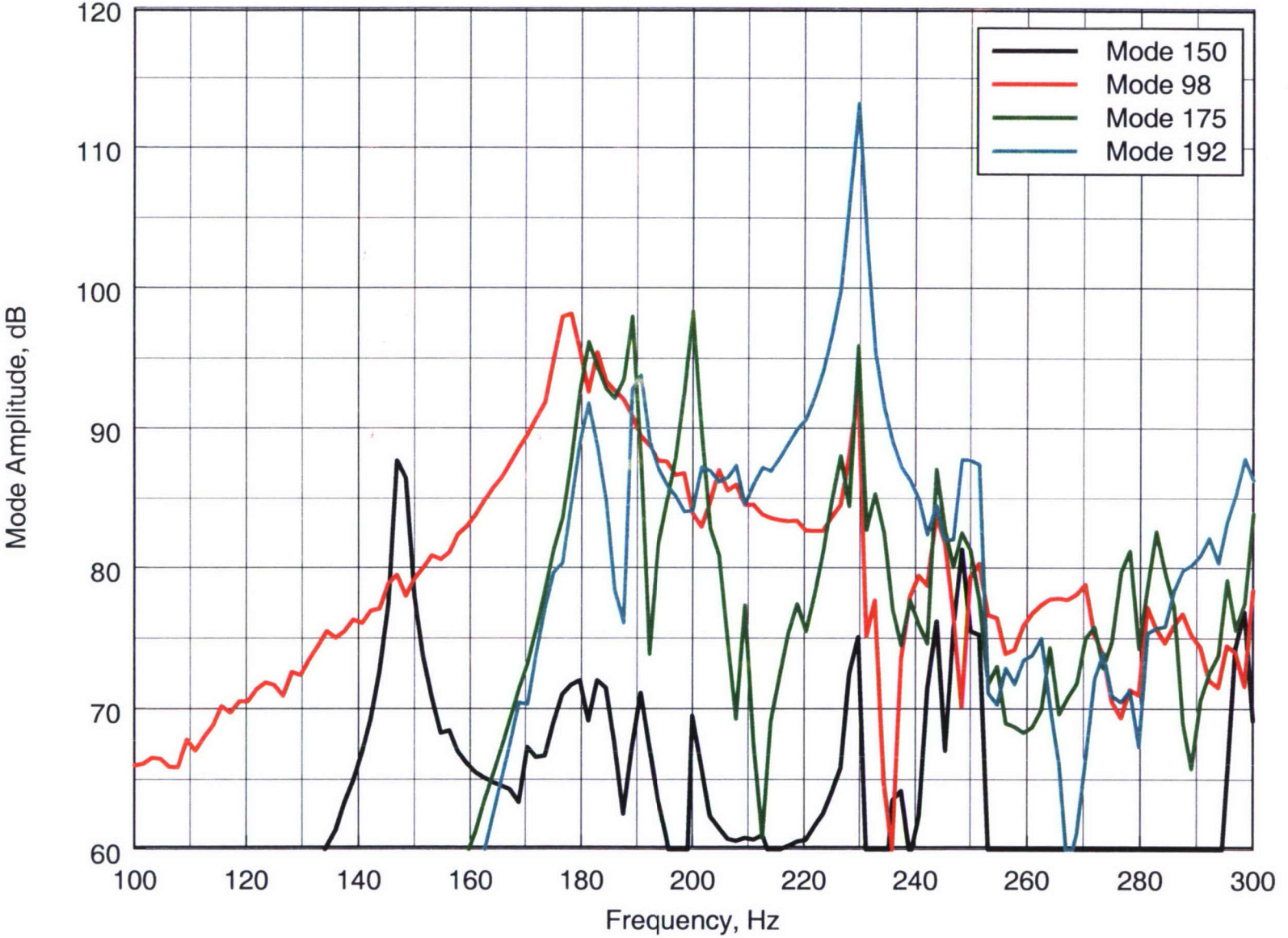

Figure 39. Dominant Mode Amplitudes for the Revised Finite Element Model

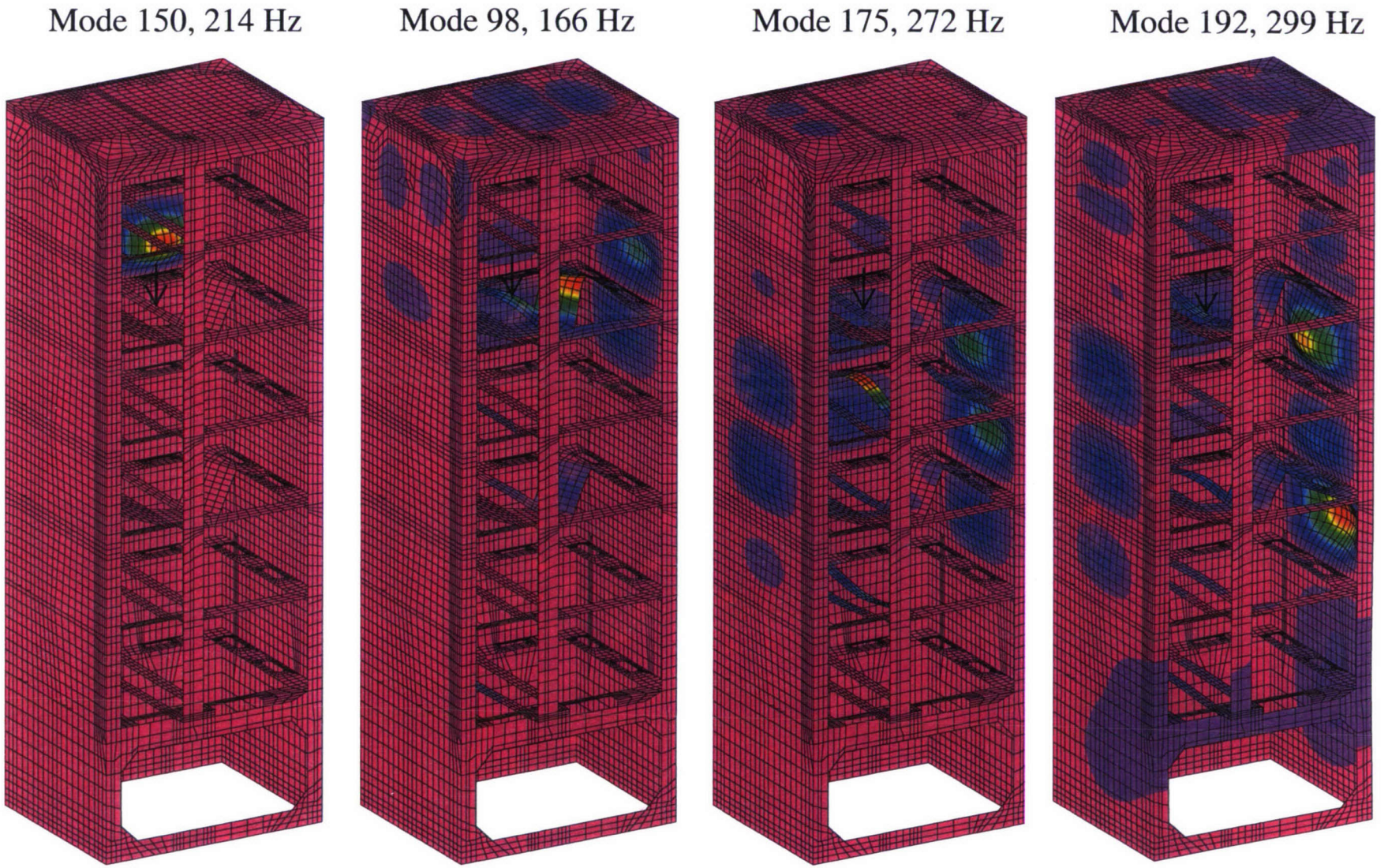

Figure 40. Mode Shapes and Resonance Frequencies for the Dominant Modes for the Revised Finite Element Model

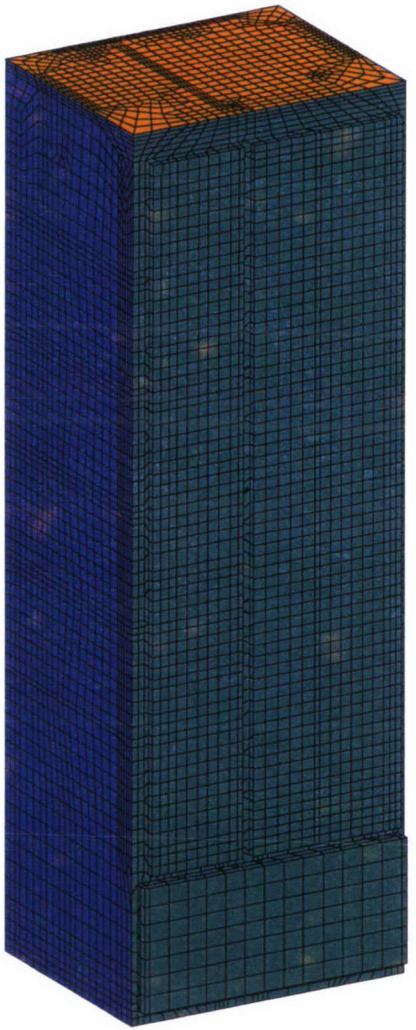

Figure 41. Boundary Element Representation of the Outer Enclosure Skin for the Revised Finite Element Mesh

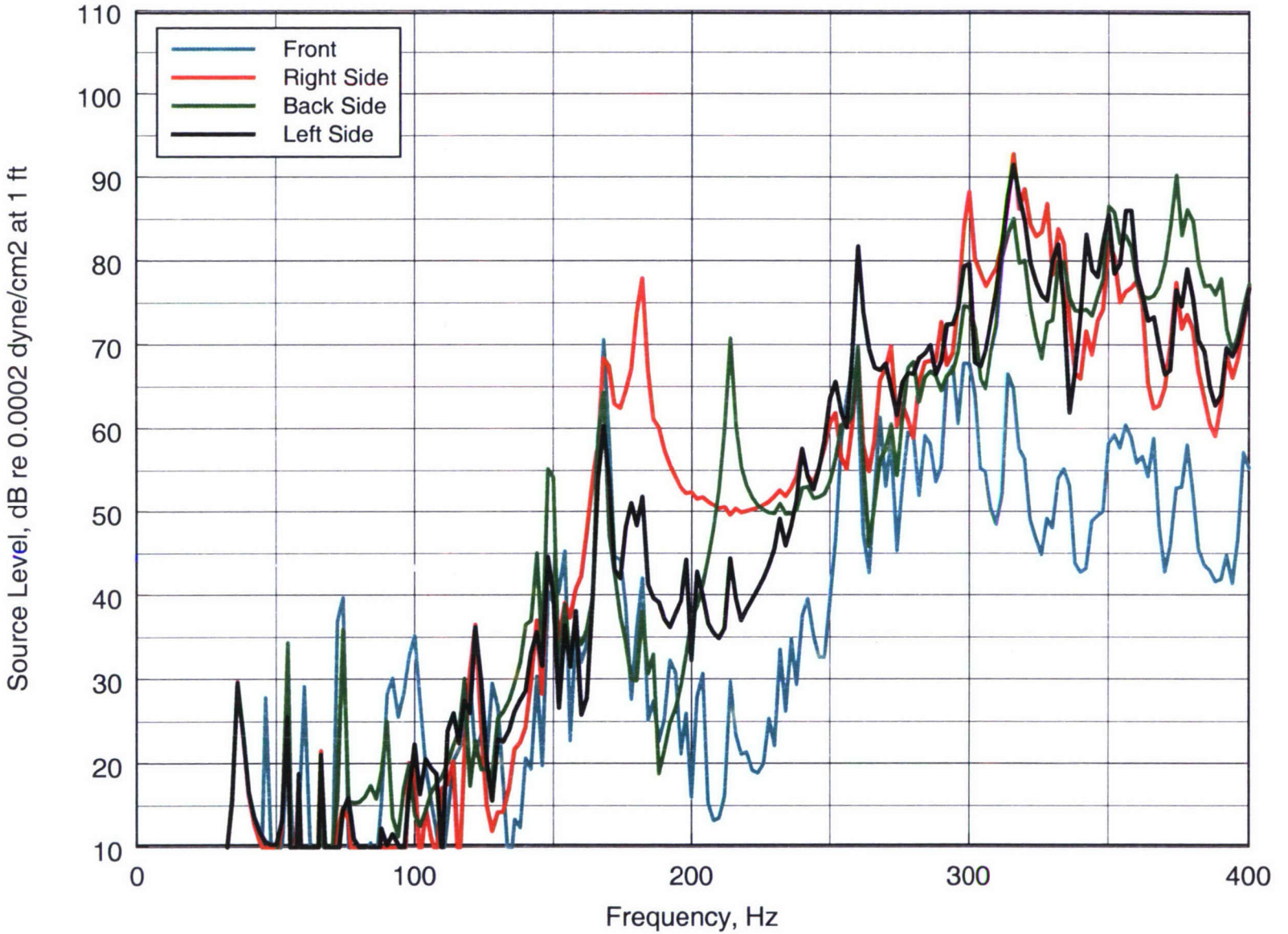

Figure 42. Predicted Acoustic Pressure Levels Near the Enclosure Surface for the Revised Finite Element Model

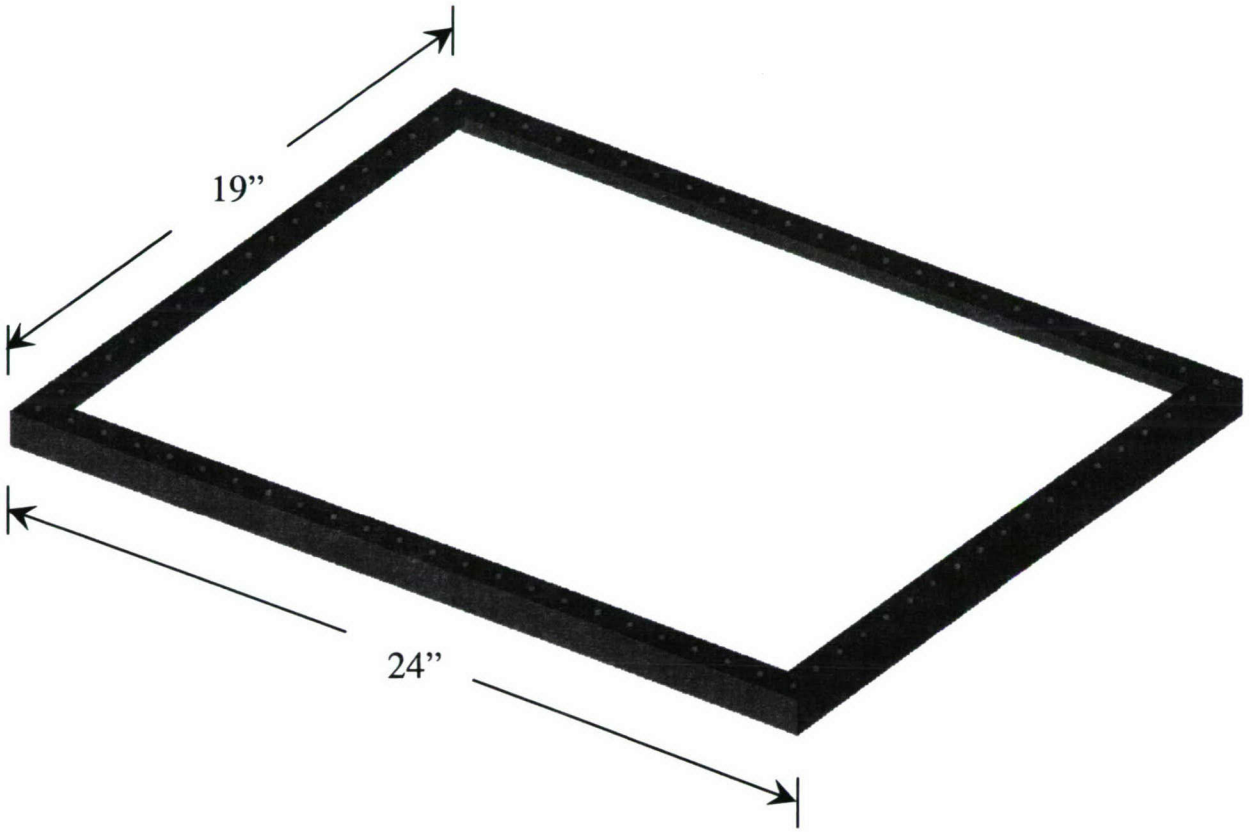

Figure 43. Shelf Frame and Stiffeners

Figure 44. Prototypical Shelf Attached to Base Structure

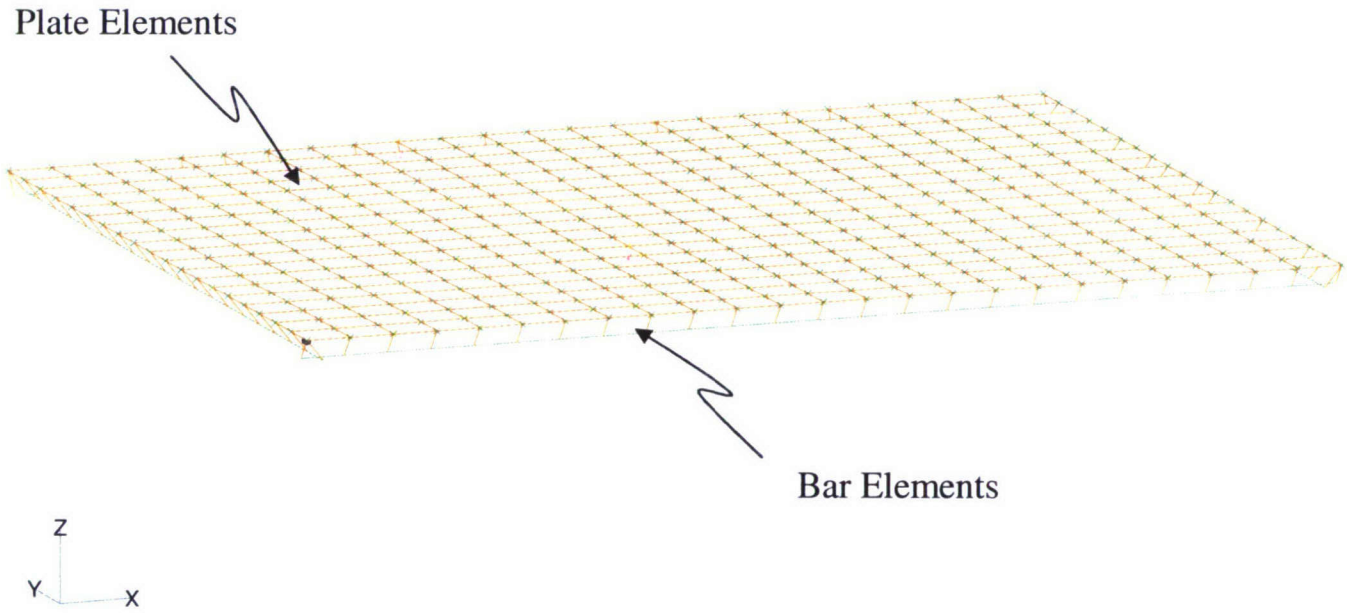

Figure 45. Typical Shelf Model

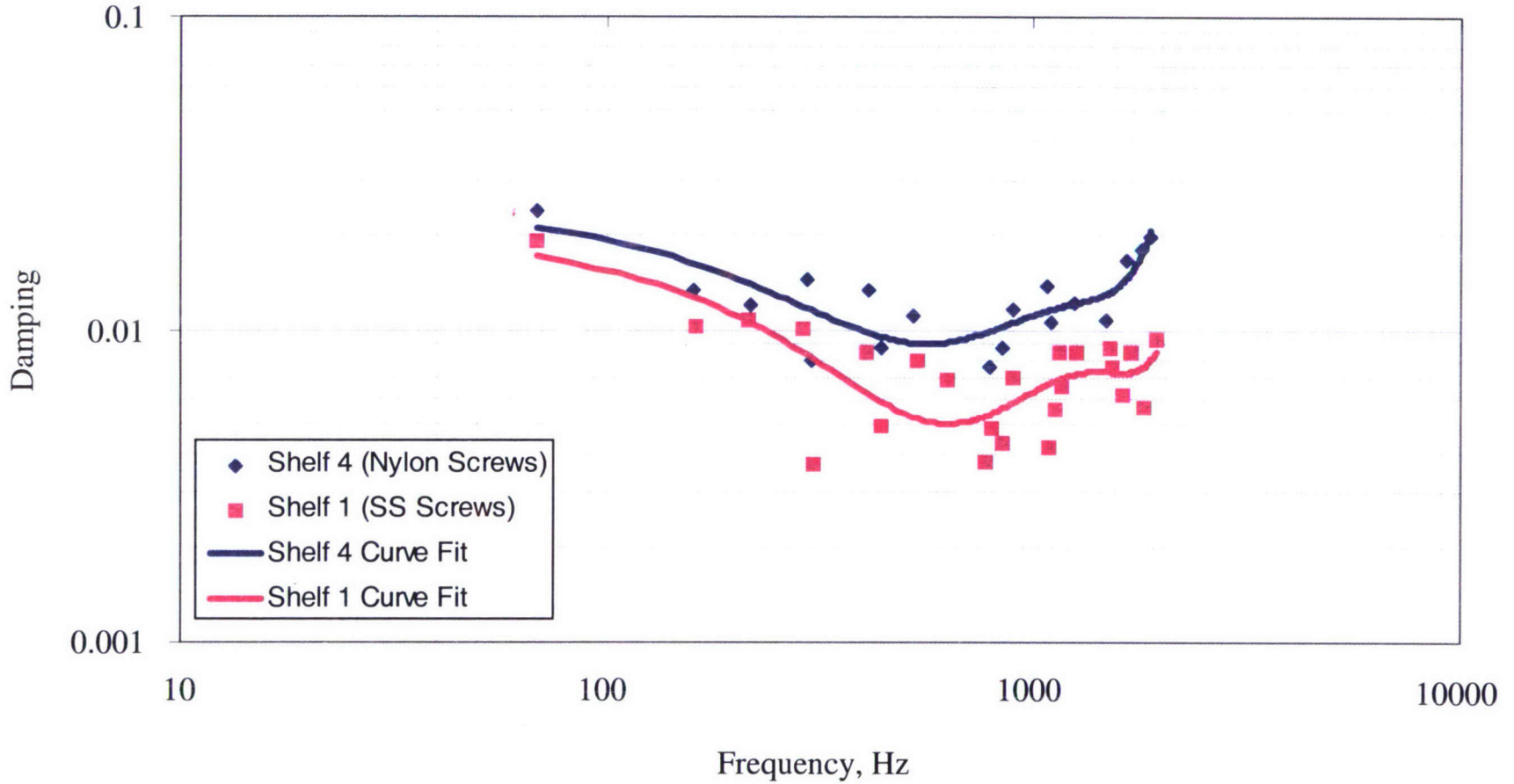

Figure 46. Damping Comparisons for Shelves 1 and 4

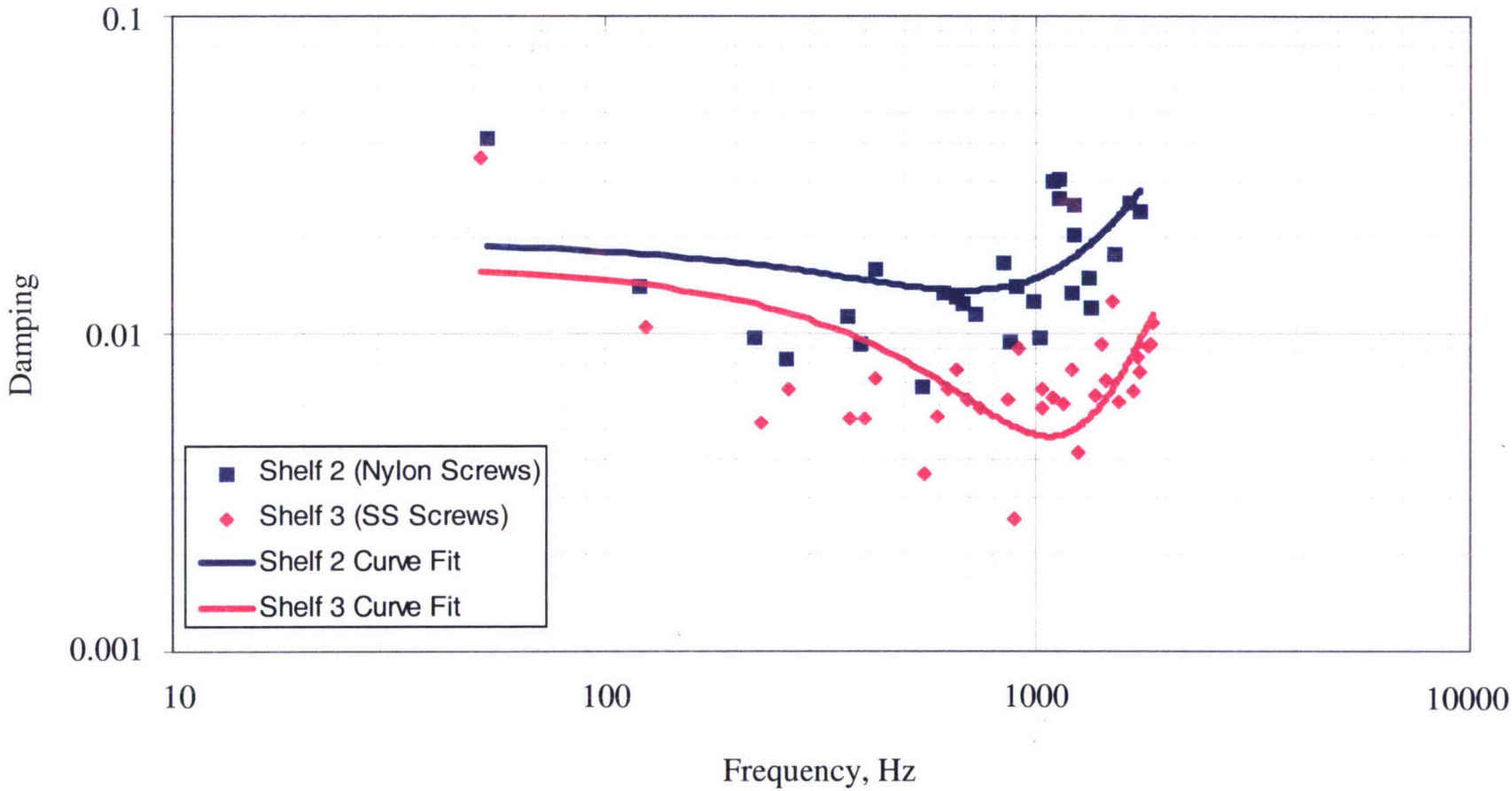

Figure 47. Damping Comparisons for Shelves 2 and 3

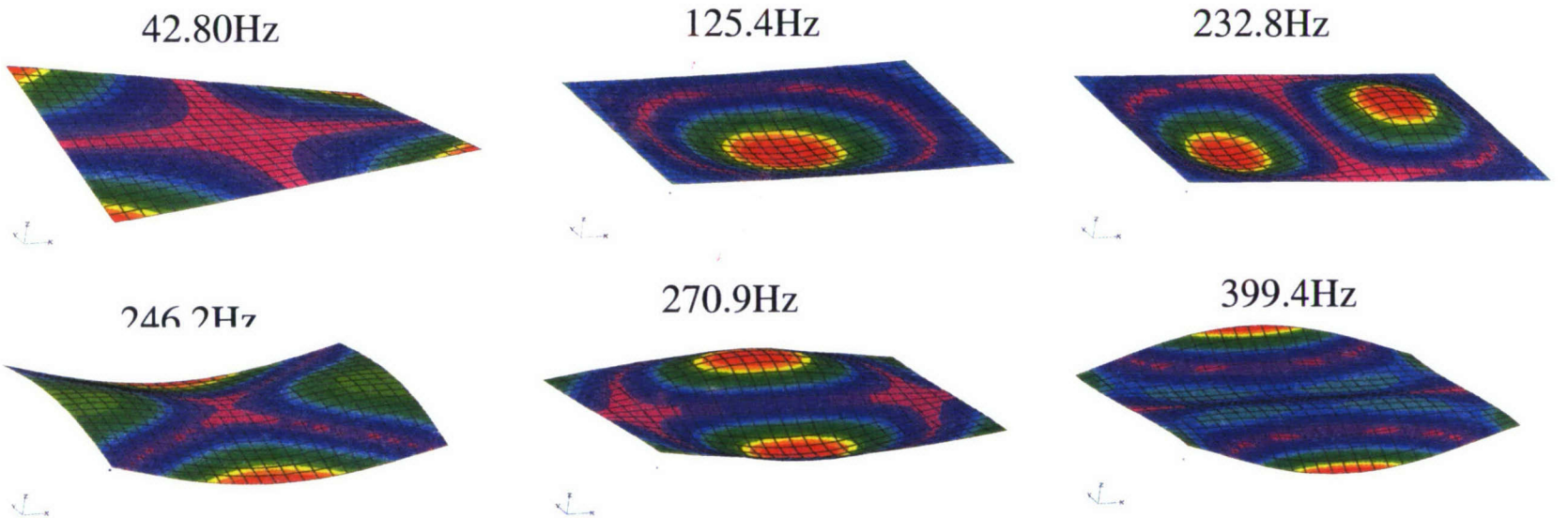

Figure 48. First Six Predicted Flexible Mode Shapes for Shelf 3

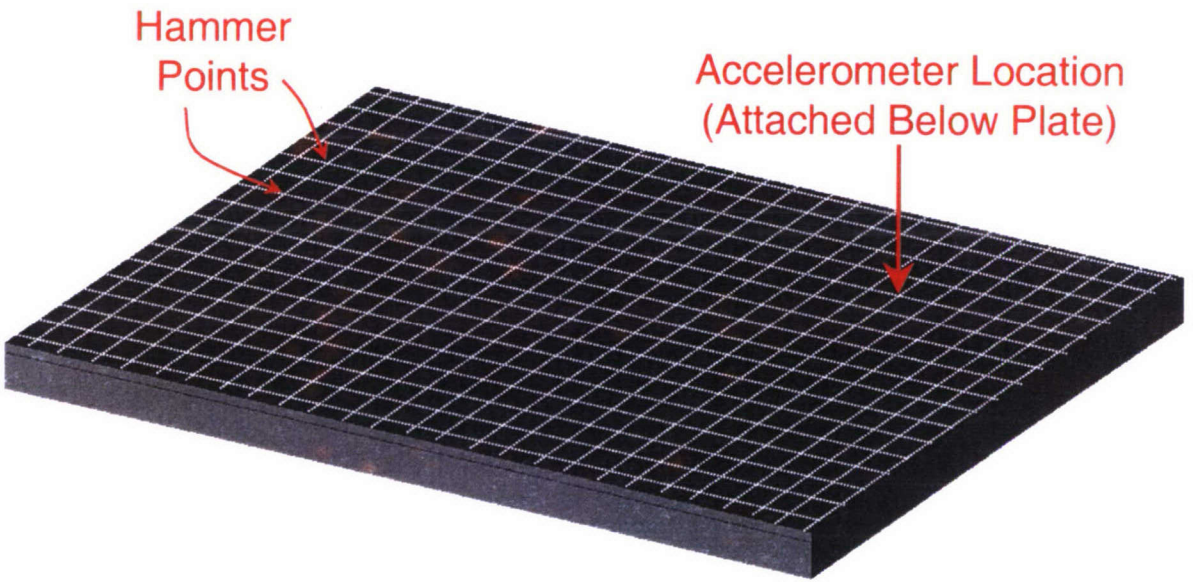

Figure 49. Impact Hammer Testing

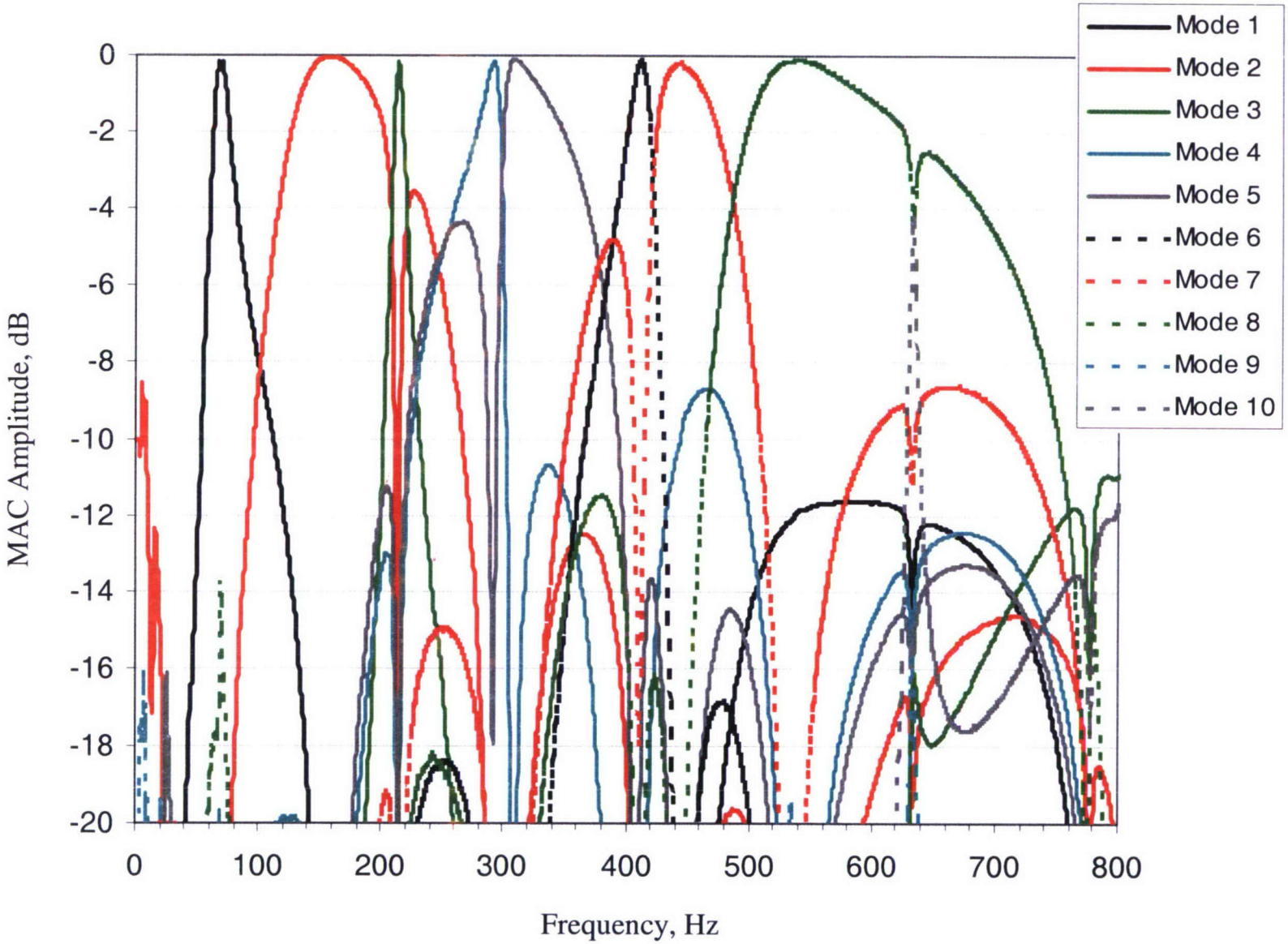

Figure 50. MAC Amplitudes for Prototype Shelf 1

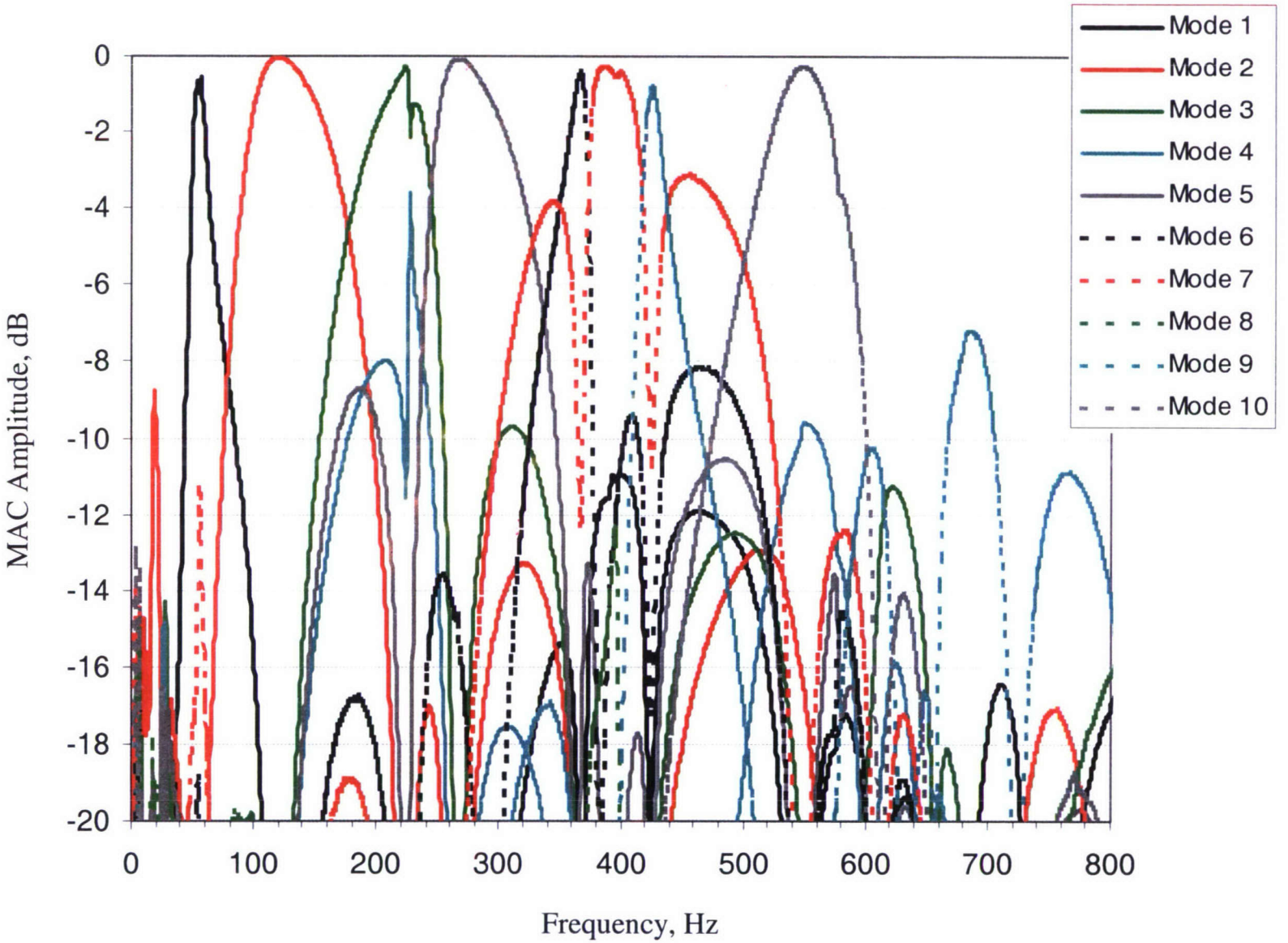

Figure 51. MAC Amplitudes for Prototype Shelf 2

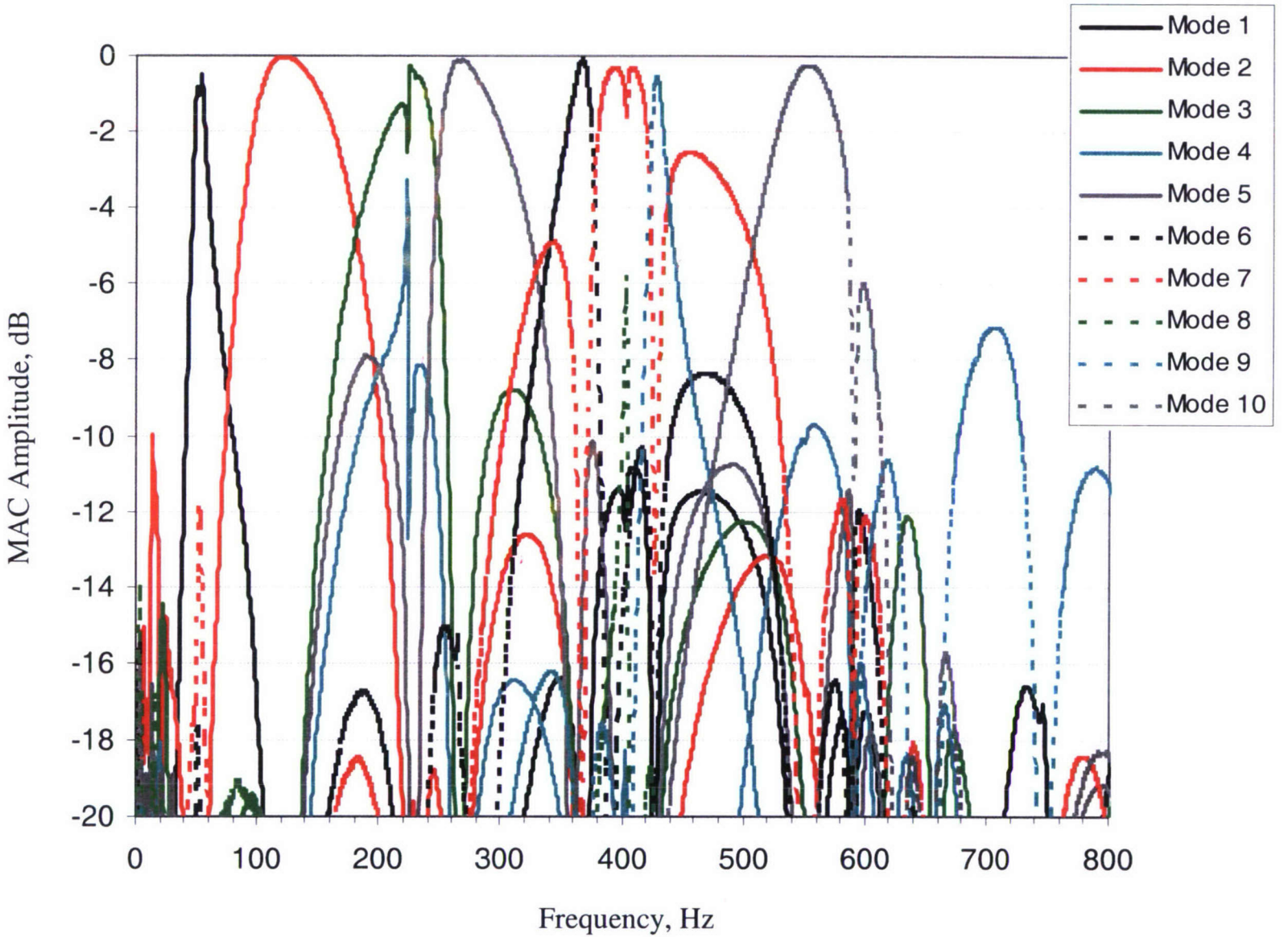

Figure 52. MAC Amplitudes for Prototype Shelf 3

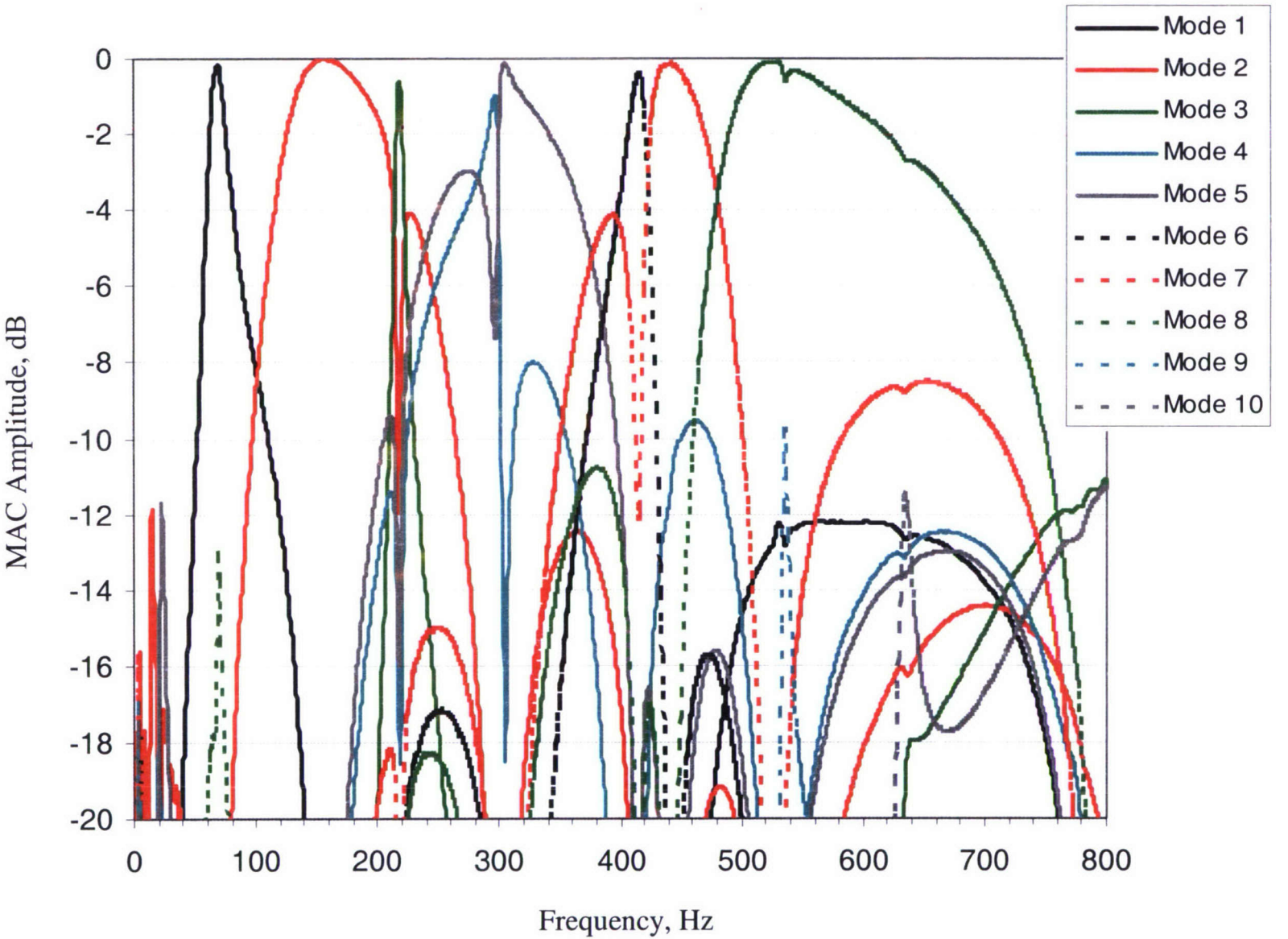

Figure 53. MAC Amplitudes for Prototype Shelf 4

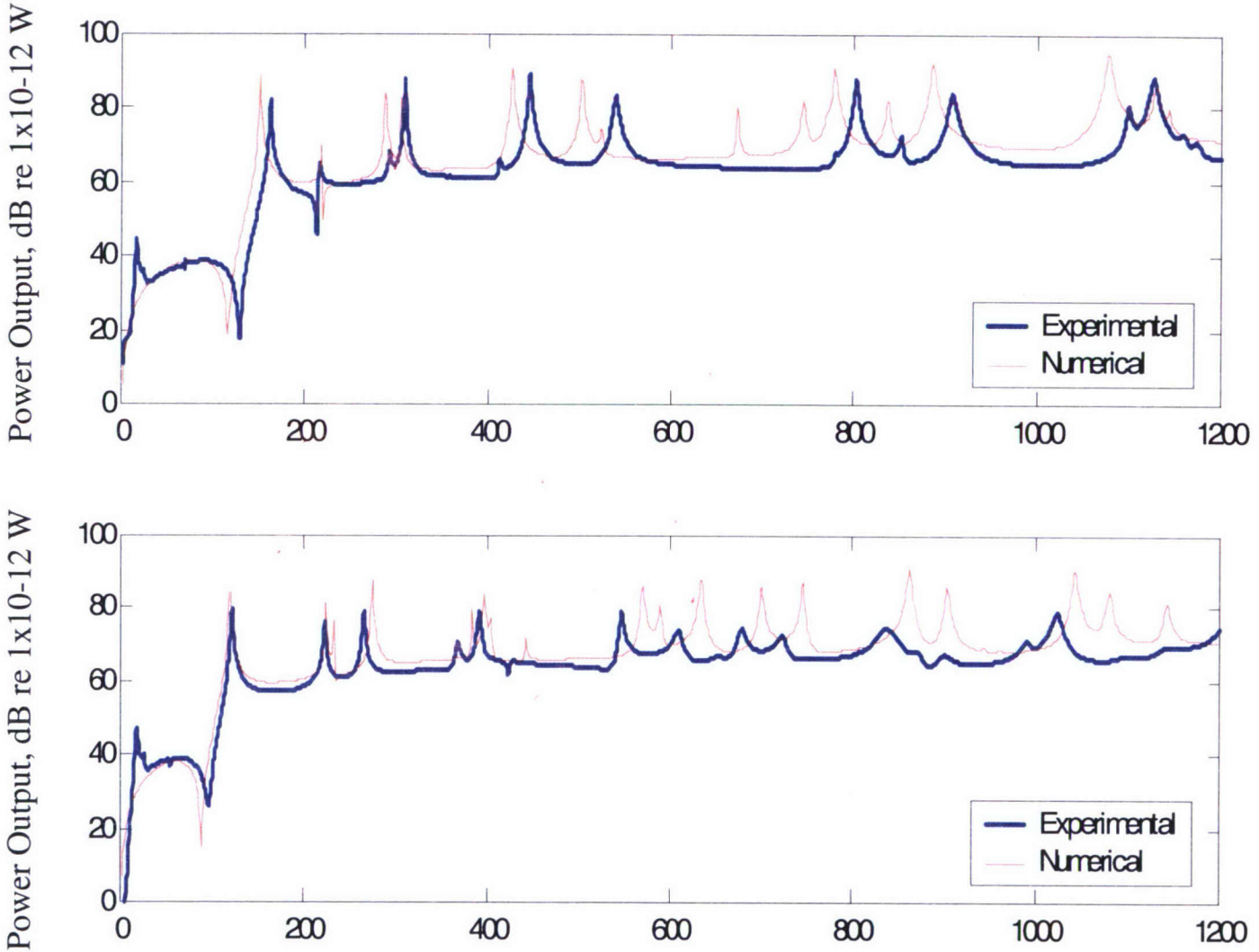

Figure 54. Power Levels for Prototype Shelves 1 and 2

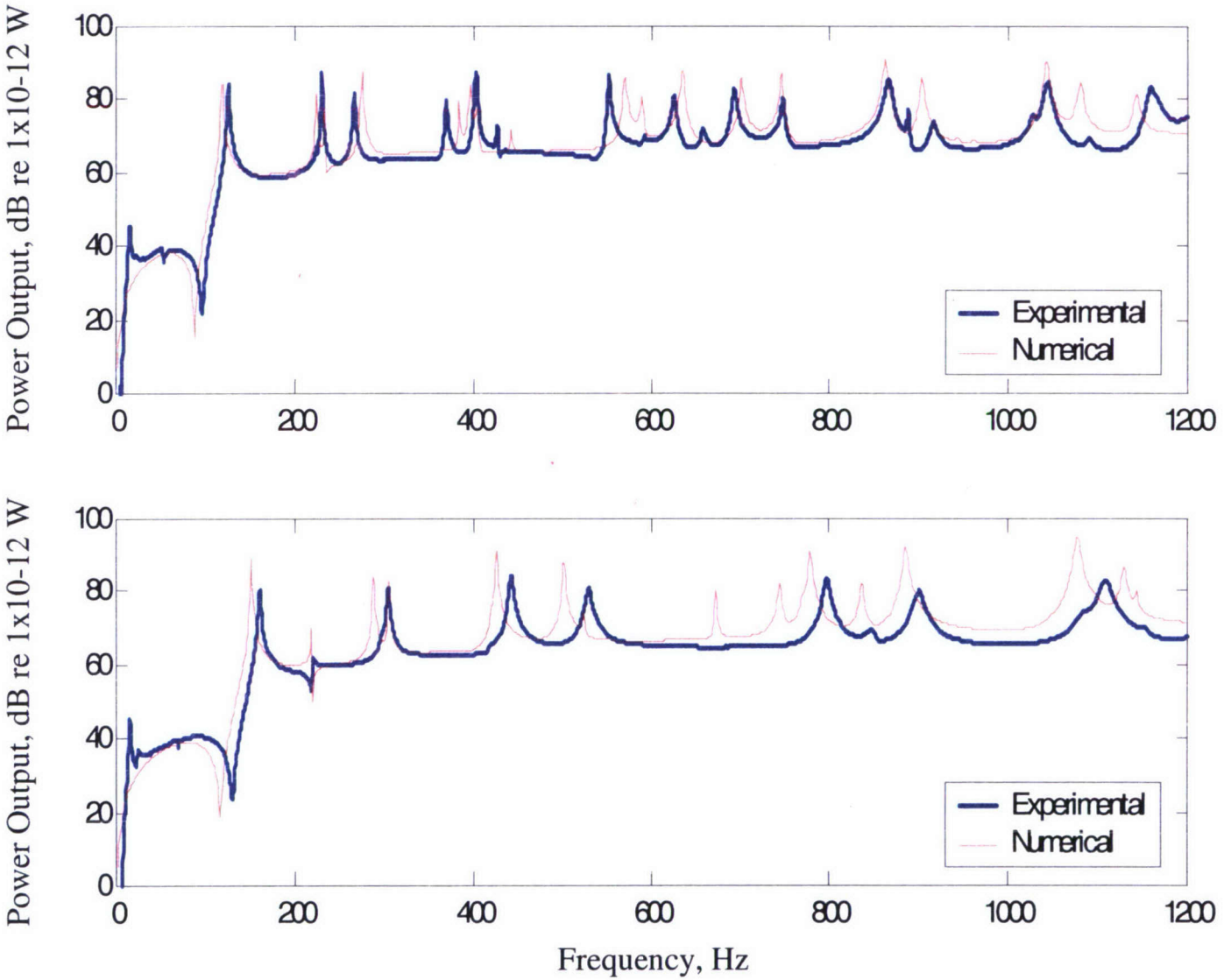

Figure 55. Power Levels for Prototype Shelves 3 and 4